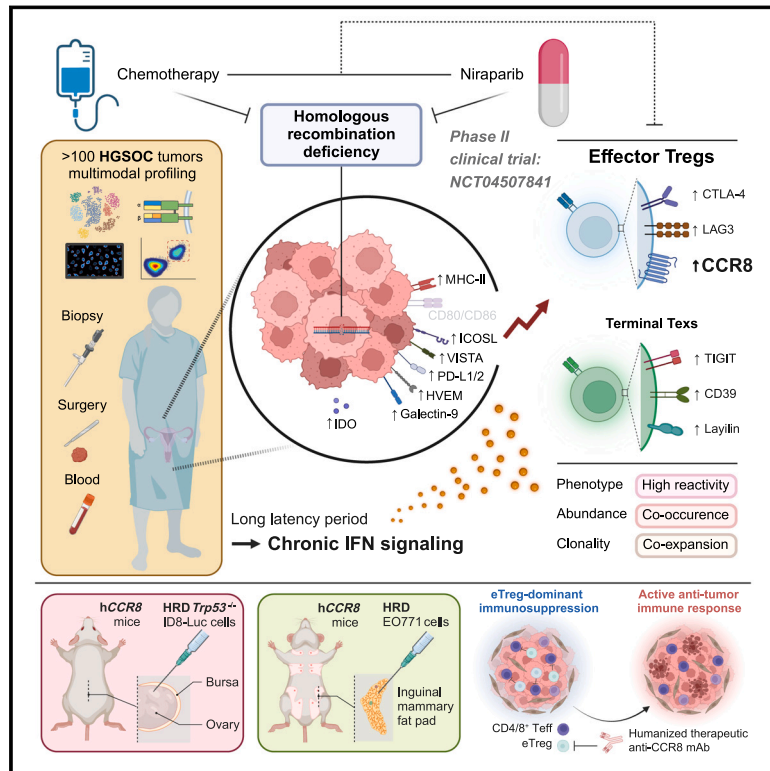# Neoadjuvant PARPi or chemotherapy in ovarian cancer informs targeting effector Treg cells for homologous-recombination-deficient tumors

Graphical abstract

Authors

Yikai Luo (罗伊凯), Yu Xia (夏宇), Dan Liu (刘眈), ..., Yong Fang (方勇), Han Liang (梁晗), Qinglei Gao (高庆蕾)

Correspondence

dma@tjh.tjmu.edu.cn (D.M.),
tongjify@163.com (Y.F.),
hliang1@mdanderson.org (H.L.),
qlgao@tjh.tjmu.edu.cn (Q.G.)

In brief

Examination of tumor microenvironment dynamics following neoadjuvant PARP inhibition or chemotherapy in newly diagnosed high-grade serous ovarian cancers (HGSOCs) reveals effector Treg cells (eTregs) as a major mediator of homologous recombination deficiency (HRD) and treatment effects. Depletion of eTregs is shown to be effective in suppressing HRD tumors in multiple mouse models.

Highlights

- The TME of HRD HGSOC is characterized by the enrichment of tumor-reactive T cells

- Neoadjuvant therapies preferentially suppress infiltrating eTregs in HRD tumors

- TME-wide interferon signaling correlates with HRD-dependent eTreg enrichment

- Joint targeting of PARP and eTregs in HRD tumors exhibits superior therapeutic efficacy

Cell

Article

Neoadjuvant PARPi or chemotherapy in ovarian cancer informs targeting effector Treg cells for homologous-recombination-deficient tumors

Yikai Luo (罗伊凯),[1,3,4,10] Yu Xia (夏宇),[1,2,10] Dan Liu (刘眈),[1,2,10] Xiong Li (李雄),[5,10] Huayi Li (李华裔),[1,2,10] Jiahao Liu (刘家豪),[1,2,10] Dongchen Zhou (周东晨),[1,2,10] Yu Dong (董宇),[6,10] Xin Li (李昕),[1,2] Yiyu Qian (钱益宇),[1,2] Cheng Xu (徐成),[1,2] Kangjia Tao (陶康佳),[1,2] Guannan Li (李冠楠),[1,2] Wen Pan (潘雯),[1,2] Qing Zhong (钟庆),[1,2] Xingzhe Liu (刘兴哲),[1,2] Sen Xu (徐森),[1,2] Zhi Wang (王志),[5] Ronghua Liu (刘荣华),[1,2] Wei Zhang (张玮),[1,2] Wanying Shan (单婉莹),[1,2] Tian Fang (方田),[1,2] Siyuan Wang (王思媛),[1,2] Zikun Peng (彭子坤),[1,2] Ping Jin (靳平),[1,2] Ning Jin (金宁),[1,2] Shennan Shi (石珅男),[1,2] Yuxin Chen (陈毓馨),[1,2] Mengjie Wang (王梦婕),[1,2] Xiaofei Jiao (焦笑飞),[1,2] Mengshi Luo (罗梦诗),[1,2] Wenjian Gong (巩文建),[1,2] Ya Wang (王亚),[1,2] Yue Yao (姚玥),[6] Yi Zhao (赵义),[6] Xinlin Huang (黄新林),[6] Xuwo Ji (季序我),[6] Zhaoren He (贺照人),[7] Guangnian Zhao (赵光年),[1,2] Rong Liu (刘嵘),[1,2] Mingfu Wu (吴明富),[1,2] Gang Chen (陈刚),[1,2] Li Hong (洪莉),[8] the COCPO Consortium, Ding Ma (马丁),[1,2,*] Yong Fang (方勇),[1,2,*] Han Liang (梁晗),[3,9,4,11,*] and Qinglei Gao (高庆蕾)[1,2,*]

[1]National Clinical Research Center for Obstetrics and Gynecology, Department of Gynecological Oncology, Tongji Hospital, Tongji Medical College, Huazhong University of Science and Technology, Wuhan 430030, China
[2]Cancer Biology Research Center (Key Laboratory of the Ministry of Education, Hubei Provincial Key Laboratory of Tumor Invasion and Metastasis), Tongji Hospital, Tongji Medical College, Huazhong University of Science and Technology, Wuhan 430030, China
[3]Department of Bioinformatics and Computational Biology, The University of Texas MD Anderson Cancer Center, Houston, TX 77030, USA
[4]Graduate Program in Quantitative and Computational Biosciences, Baylor College of Medicine, Houston, TX 77030, USA
[5]Department of Gynecology & Obstetrics, Central Hospital of Wuhan, Tongji Medical College, Huazhong University of Science and Technology, Wuhan 430014, China
[6]Precision Scientific (Beijing) Co., Ltd., Beijing 100085, China
[7]BioMap (Beijing) Intelligence Technology Limited, Beijing 100089, China
[8]Department of Gynecology and Obstetrics, Renmin Hospital of Wuhan University, Wuhan 430060, China
[9]Department of Systems Biology, The University of Texas MD Anderson Cancer Center, Houston, TX 77030, USA
[10]These authors contributed equally
[11]Lead contact
*Correspondence: dma@tjh.tjmu.edu.cn (D.M.), tongjify@163.com (Y.F.), hliang1@mdanderson.org (H.L.), qlgao@tjh.tjmu.edu.cn (Q.G.)
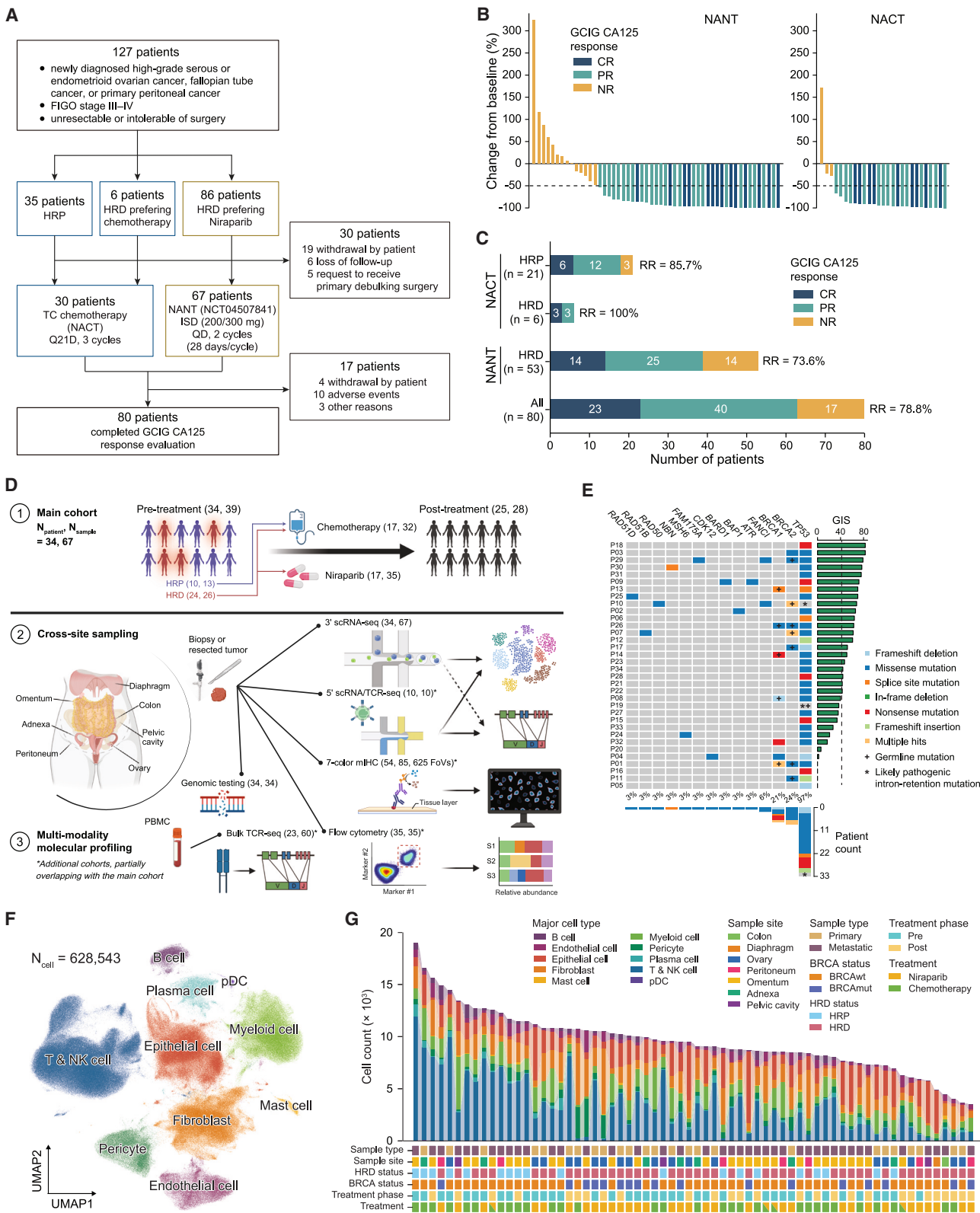https://doi.org/10.1016/j.cell.2024.06.013

SUMMARY

Homologous recombination deficiency (HRD) is prevalent in cancer, sensitizing tumor cells to poly (ADP-ribose) polymerase (PARP) inhibition. However, the impact of HRD and related therapies on the tumor microenvironment (TME) remains elusive. Our study generates single-cell gene expression and T cell receptor profiles, along with validatory multimodal datasets from >100 high-grade serous ovarian cancer (HGSOC) samples, primarily from a phase II clinical trial (NCT04507841). Neoadjuvant monotherapy with the PARP inhibitor (PARPi) niraparib achieves impressive 62.5% and 73.6% response rates per RECIST v.1.1 and GCIG CA125, respectively. We identify effector regulatory T cells (eTregs) as key responders to HRD and neoadjuvant therapies, co-occurring with other tumor-reactive T cells, particularly terminally exhausted CD8$^+$ T cells (Tex). TME-wide interferon signaling correlates with cancer cells upregulating MHC class II and co-inhibitory ligands, potentially driving Treg and Tex fates. Depleting eTregs in HRD mouse models, with or without PARP inhibition, significantly suppresses tumor growth without observable toxicities, underscoring the potential of eTreg-focused therapeutics for HGSOC and other HRD-related tumors.

INTRODUCTION

As a major driver of genomic instability, homologous recombination deficiency (HRD) occurs frequently in human cancers (e.g., ~50% in ovarian cancer).[1–3] It has attracted wide interest because of synthetic lethality, wherein this defect renders tumors vulnerable to poly (ADP-ribose) polymerase (PARP) inhibition.[4,5] Multiple PARP inhibitors have been approved for the treatment of ovarian, breast, prostate, and pancreatic cancers, and many more are being

Cell
Article

A

127 patients
- newly diagnosed high-grade serous or endometrioid ovarian cancer, fallopian tube cancer, or primary peritoneal cancer
- FIGO stage III–IV
- unresectable or intolerable of surgery

35 patients HRP

6 patients HRD prefering chemotherapy

86 patients HRD prefering Niraparib

30 patients
19 withdrawal by patient
6 loss of follow-up
5 request to receive primary debulking surgery

30 patients
TC chemotherapy (NACT)
Q21D, 3 cycles

67 patients
NANT (NCT04507841)
ISD (200/300 mg)
QD, 2 cycles
(28 days/cycle)

17 patients
4 withdrawal by patient
10 adverse events
3 other reasons

80 patients
completed GCIG CA125 response evaluation

B

GCIG CA125 response
- CR
- PR
- NR

NANT

NACT

Change from baseline (%)

C

GCIG CA125 response
- CR
- PR
- NR

NACT HRP (n = 21): 6 | 12 | 3 — RR = 85.7%
NACT HRD (n = 6): 3 | 3 — RR = 100%
NANT HRD (n = 53): 14 | 25 | 14 — RR = 73.6%
All (n = 80): 23 | 40 | 17 — RR = 78.8%

Number of patients

D

① Main cohort
$N_{patient}, N_{sample}$ = 34, 67

Pre-treatment (34, 39)

Chemotherapy (17, 32)

Niraparib (17, 35)

HRP (10, 13)
HRD (24, 26)

Post-treatment (25, 28)

② Cross-site sampling

Diaphragm
Omentum
Colon
Adnexa
Pelvic cavity
Peritoneum
Ovary

Biopsy or resected tumor

3' scRNA-seq (34, 67)

5' scRNA/TCR-seq (10, 10)*

7-color mIHC (54, 85, 625 FoVs)*

Tissue layer

Genomic testing (34, 34)

③ Multi-modality molecular profiling
*Additional cohorts, partially overlapping with the main cohort

PBMC

Bulk TCR-seq (23, 60)*

Flow cytometry (35, 35)*

Marker #2 / Marker #1

S1 S2 S3
Relative abundance

E

RAD51D RAD51B RAD50 NBN FAM175A MSH6 CDK12 BARD1 BAP1 ATR FANCI BRCA1 BRCA2 TP53

GIS

Frameshift deletion
Missense mutation
Splice site mutation
In-frame deletion
Nonsense mutation
Frameshift insertion
Multiple hits
+ Germline mutation
* Likely pathogenic intron-retention mutation

Patient count

F

N_{cell} = 628,543

B cell
pDC
Plasma cell
Myeloid cell
T & NK cell
Epithelial cell
Mast cell
Fibroblast
Pericyte
Endothelial cell

UMAP2 / UMAP1

G

Cell count (× 10³)

Major cell type
- B cell
- Endothelial cell
- Epithelial cell
- Fibroblast
- Mast cell
- Myeloid cell
- Pericyte
- Plasma cell
- T & NK cell
- pDC

Sample site
- Colon
- Diaphragm
- Ovary
- Peritoneum
- Omentum
- Adnexa
- Pelvic cavity

Sample type
- Primary
- Metastatic

BRCA status
- BRCAwt
- BRCAmut

HRD status
- HRP
- HRD

Treatment phase
- Pre
- Post

Treatment
- Niraparib
- Chemotherapy

Sample type
Sample site
HRD status
BRCA status
Treatment phase
Treatment

(legend on next page)

Cell
Article

CellPress
OPEN ACCESS

developed for or tested in various solid and hematological malignancies.[6,7] Although recent studies have started to shed light on the interplay between HRD and the tumor microenvironment (TME) of human cancers,[8–10] including ovarian cancer,[11] it remains a top priority to decode the interaction effects of HRD and PARP inhibition on the TME. Practical hurdles to such characterizations, including prior treatment exposures and heterogeneous patient populations, impede a deeper understanding of TME plasticity and the development of novel, effective cancer therapies. Because high-grade serous ovarian cancer (HGSOC) has the highest prevalence of HRD and often requires neoadjuvant therapies to achieve optimal debulking,[12,13] it exemplifies an archetypal disease for characterizing the effect of HRD on treatment-naive TME and subsequent changes induced by PARP inhibition.

Efforts to address this knowledge gap would have crucial implications for understanding why in HGSOC evidence of therapeutic benefits by immune checkpoint inhibitors (ICIs) is lacking.[14] Across phase III clinical trials, the addition of PD-1/PD-L1-targeting agents, including nivolumab,[15] avelumab,[16,17] and atezolizumab,[18,19] to chemotherapy and/or targeted therapy (e.g., bevacizumab) failed to confer a survival benefit in a variety of disease settings. Combining nivolumab with CTLA-4-targeting ipilimumab resulted in significantly improved progression-free survival than nivolumab alone but in a smaller cohort.[20] Importantly, PD-L1 positive score as a classical ICI biomarker did not show consistent trends with the response rate (RR) in the trials mentioned above. These clinical observations suggest a complex immunomodulatory landscape in HGSOC beyond the PD-1/PD-L1 signaling, calling for a comprehensive search of critical immune factors.

Here, we leveraged a large number of samples from a clinical study to evaluate neoadjuvant PARP inhibition in HRD HGSOC (NCT04507841).[21] In parallel, we collected samples from patients receiving neoadjuvant chemotherapy (NACT). Single-cell and bulk multimodal profiling of these samples yielded valuable data that enabled us to delineate the TME divergence between HRD and homologous recombination-proficient (HRP) tumors as well as their phenotypic evolution following the neoadjuvant therapies.

RESULTS

A single-cell atlas of the HGSOC TME under neoadjuvant treatment

To investigate the effects of HRD, neoadjuvant therapies, and their interactions on the TME, we recruited treatment-naive patients with newly diagnosed unresectable HGSOC in our phase II clinical trial (NCT04507841) (Figure 1A; Table S1). We determined the response to neoadjuvant niraparib monotherapy (NANT) or NACT for each patient according to the Gynecologic Cancer InterGroup (GCIG) CA125 response criteria[22,23] (Figure 1B; Table S1). Dynamically and effectively monitoring overall tumor burden within a short period, especially for patients with non-measurable lesions, GCIG CA125 response was suited for longitudinal quantitative analysis of TME correlates. Among 53 HRD patients who received NANT, 14 (26.4%) achieved complete response (CR) and 25 (47.2%) reached partial response (PR), resulting in a GCIG CA125 RR of 73.6% (62.5% per RECIST v.1.1) (Figure 1C). Six HRD patients chose to receive NACT and exhibited an RR of 100.0%, including three patients with CR and three patients with PR (Figure 1C). In parallel, 21 HRP patients received NACT. Six patients yielded CR, and 12 patients acquired PR, resulting in an RR of 85.7% (Figure 1C). In total, 80 patients who underwent either neoadjuvant treatment displayed a GCIG CA125 RR of 78.8% (Figure 1C). Overall, the safety profile of NANT was manageable, and no new safety signal was observed, with hematologic toxicities as the most common treatment-related adverse events. These results indicate that NANT is an effective treatment option for controlling disease progression for HRD patients with HGSOC.

From 34 patients in the trial cohort, we obtained 67 tumor samples (39 pre-treatment and 28 post-treatment), including 24 site-matched pre- and post-treatment pairs as our main cohort for single-cell RNA sequencing (scRNA-seq) (Figure 1D; Table S1). These patients had a balanced distribution of HRD status and genomic aberrations, as surveyed by our HRD assay (Figure 1E; Table S2). The scRNA-seq data were processed through a rigorous quality control (QC) and preprocessing pipeline (Figures S1A–S1D). We observed consistent high quality across samples, with low ambient contamination (Figure S1A), high per-cell unique molecular identifier (UMI) and gene count, and low mitochondrial DNA UMI and ribosomal UMI proportions

Figure 1. Study design and dataset overview

(A) Flowchart of patient enrollment and treatment.

(B) Percentage change in GCIG CA125 level from baseline. Dashed black line represents a −50% change in GCIG CA125 level from baseline, indicating a GCIG CA125 response. A CA125 value below the reference level further indicates CR. Otherwise, PR is documented.

(C) Patient response according to GCIG CA125 response criteria stratified by HRD status and treatment cohort.

(D) Cross-site sampling of tumor and blood samples for single-cell and bulk multi-omic profiling from ovarian cancer patients. Numbers in parentheses indicate patient count and sample count, respectively.

(E) Genomic alterations of a panel of homologous recombination repair (HRR) genes across 34 patients in the main cohort. Top, genomic instability scores (GISs); dotted black line indicates a GIS threshold of 42 for HRD approved by the US Food and Drug Administration. Right, sample count with a mutated gene of interest. Germline mutations are highlighted with the "+" sign. Silent mutations with clear functional consequences are highlighted with the "*" sign.

(F) Uniform manifold approximation and projection (UMAP) embedding of all cells in the main cohort with major cell types annotated.

(G) Major cell type composition and clinical metadata for each sample.

FIGO, The International Federation of Gynecology and Obstetrics; HRD, homologous recombination deficiency; HRP, homologous recombination proficiency; BRCAm, mutated *BRCA1/2*; BRCAwt, wild-type *BRCA1/2*; GIS, genomic instability score; ISD, individualized starting dose; TC, paclitaxel and carboplatin; CR, complete response; PR, partial response; NR, non-response; RR, response rate; GCIG, the Gynecologic Cancer InterGroup; CA125, cancer antigen 125. See also Figure S1 and Tables S1 and S2.
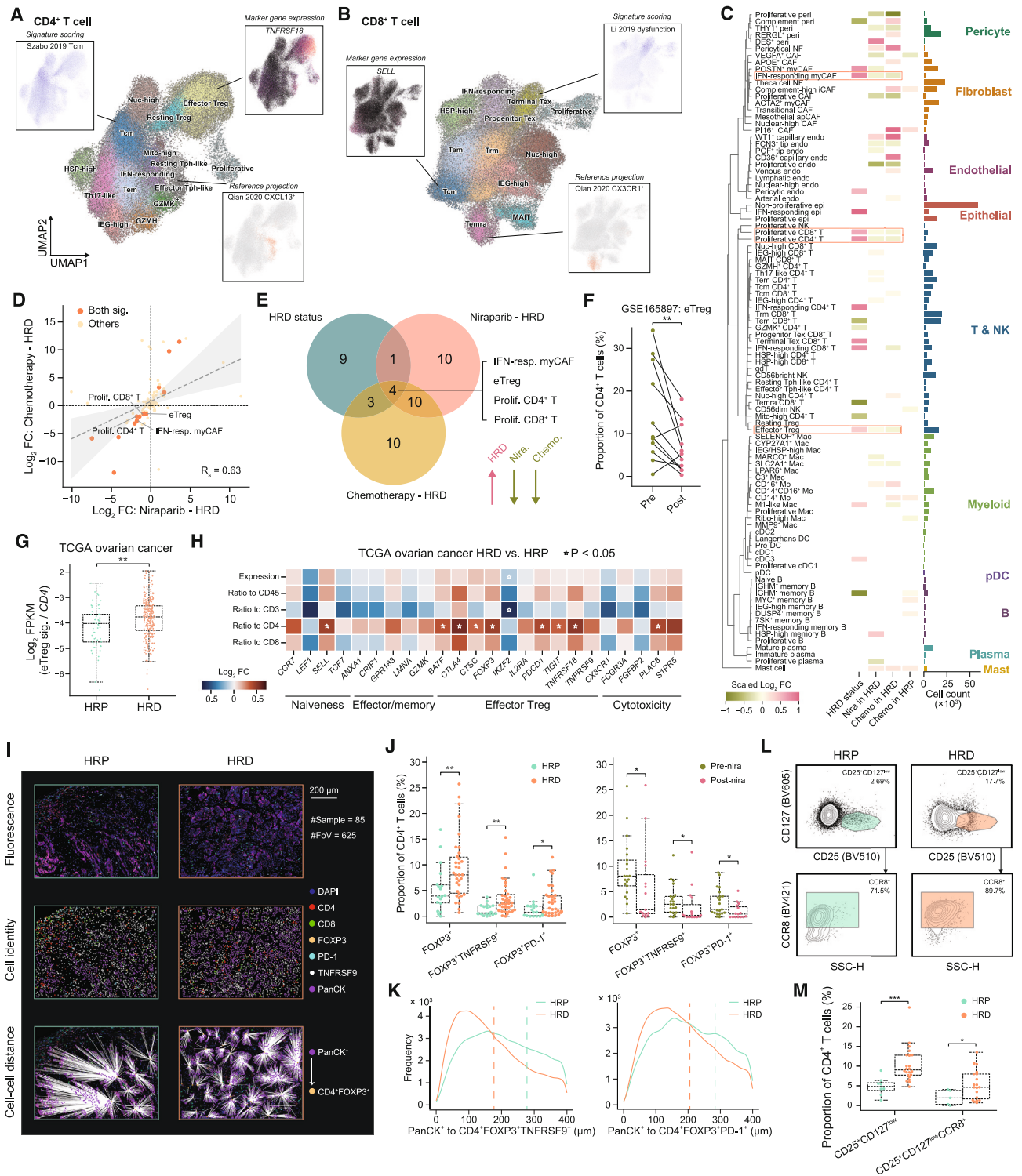
Figure 2. Tregs are enriched in pre-treatment HRD tumors and suppressed by neoadjuvant treatment

(A and B) Cell-state annotations of CD4^{+} (A) and CD8^{+} (B) T lymphocytes. Zoom-in boxes indicate marker genes, signatures, or reference projections.

(C) Differential abundance testing of 97 cell states across 10 major cell types. Left, dendrogram showing cell-state transcriptional similarities. Middle, scaled log2 FC of cell-state abundance in each comparison (two-sided Mann-Whitney U test for the HRD status comparison; two-sided paired Wilcoxon rank-sum test for the treatment comparisons). Differences with a raw $p > 0.05$ are masked in the heatmap. Right, cell count of each state. Four cell states with significant abundance changes across comparisons are highlighted.

(Figure S1E). Finally, we computationally integrated >620,000 post-QC cells and assigned them to 10 major cell types based on the expression patterns of well-established marker genes (Figures 1F and S1F–S1H). All samples contained the 10 cell types and showed a balanced distribution of cell counts, indicating a comprehensive and robust sampling of the HGSOC TME (Figure 1G). In addition to this main cohort, we performed single-cell T cell receptor sequencing (scTCR-seq), multiplex immunohistochemistry (mIHC), flow cytometry, and bulk TCR-seq for additional tumors and patient-matched peripheral blood samples (Figure 1D; Tables S3, S4, S5, and S6). Together, this rich, multimodal, and high-quality dataset represents a unique resource to elucidate how tumor-intrinsic HRD status and real-world therapies affect the TME of ovarian cancer.

HRD-tumor-enriched eTregs underlie the TME response to neoadjuvant therapies

Intertumoral TME heterogeneity established before therapeutic interventions often portends diverse patient outcomes.[24,25] At the level of major cell types, we observed a trend toward an increase of lymphocytes and endothelial cells while a decrease of epithelial cells and myeloid cells in pre-treatment metastatic tumors (Figure S2A), in line with previous studies,[11,26,27] albeit not reaching statistical significance except for B cells. Similarly, no major cell types showed a significant difference between pre-treatment HRD and HRP tumors (Figure S2B). For the effects of NACT and niraparib, we identified mast cells and endothelial cells to be significantly enriched in post-treatment tumors, respectively (Figures S2C and S2D), which merits further investigation.

These results prompted us to examine the impact of HRD and neoadjuvant therapies at a finer scale. For this purpose, we first built a cell-state hierarchy that covered all major cell types through an extensive search of the literature for transcriptional evidence supporting the identities of 97 cell states (Figure S3; STAR Methods). For example, our annotation revealed 15 and 12 states in the CD4$^+$ and the CD8$^+$ T cell compartments, respectively (Figures 2A and 2B). We then compared cell-state proportions between HRD subtypes and treatment phases,

identifying a wide range of cell-state shifts (Figure 2C). Interestingly, many cell states showed concordant abundance changes in chemotherapy and niraparib treatment (Figure 2D).

To focus on the most convergent signals, we identified four overlapped cell states out of the three comparisons, namely interferon (IFN)-responding myofibroblastic cancer-associated fibroblasts (myCAFs), effector regulatory T cells (eTregs), and proliferative CD4$^+$/CD8$^+$ T cells (Figures 2C, 2E, and S2E–S2G), all of which had higher abundance in the treatment-naive HRD TME while decreased in post-treatment HRD tumors. The Treg is the most abundant T cell population in our dataset, and its eTreg subset is well known for immunosuppressive functions.[28,29] We thus focused on validating the related observations. First, we analyzed a published scRNA-seq cohort,[30] under a matched T cell annotation scheme (Figure S4), to recapitulate a dramatic decrease of eTregs but not resting Tregs in post-NACT HGSOC tumors (Figure 2F). Second, we observed through a signature-based analysis of the TCGA HGSOC cohort that eTregs had a significantly higher infiltration level in HRD tumors (Figure 2G), which, when extended to contrast with other non-Treg T cell-state marker genes, further revealed the unique enrichment of eTregs (Figure 2H). Third, we performed mIHC of 85 HGSOC tumors (Table S3) and confirmed total Tregs and eTregs showing a significantly higher abundance in HRD tumors while markedly reduced after niraparib treatment (Figures 2I and 2J). Importantly, cancer cells (panCK$^+$) and eTregs resided nearby in HRD tumors, implying a more frequent functional interaction (Figures 2I and 2K). Lastly, we quantified the proportion of total Tregs and eTregs in another 35 treatment-naive tumors using flow cytometry (Table S4) and confirmed their stronger presence in the HRD TME (Figures 2L and 2M). These results show that the marked reduction of HRD-enriched eTregs represents the most robust change upon neoadjuvant therapies.

Tregs and Texs among tumor-reactive T cell populations coordinated by HRD

Our systematic analysis across nearly 100 cell states revealed that three out of the final four top candidates were T cell

---

(D) Correlation of cell state log$_2$ FC between niraparib therapy and chemotherapy for HRD samples only.

(E) Overlap between top hits of the three differential abundance tests.

(F) Difference in eTreg proportion among all CD4$^+$ T cells between pre- and post-chemotherapy tumors based on data from GSE165897 ($n = 11$ patients).

(G) Difference in log$_2$ ratio of the geometric FPKM average of an eTreg signature to *CD4* FPKM between HRP and HRD ovarian cancer samples from TCGA ($n = 61$ HRP samples, $n = 293$ HRD samples).

(H) Log$_2$ FC of either expression levels or expression level ratios in FPKM across T cell marker genes. Entries with a statistically significant difference are marked by an asterisk sign.
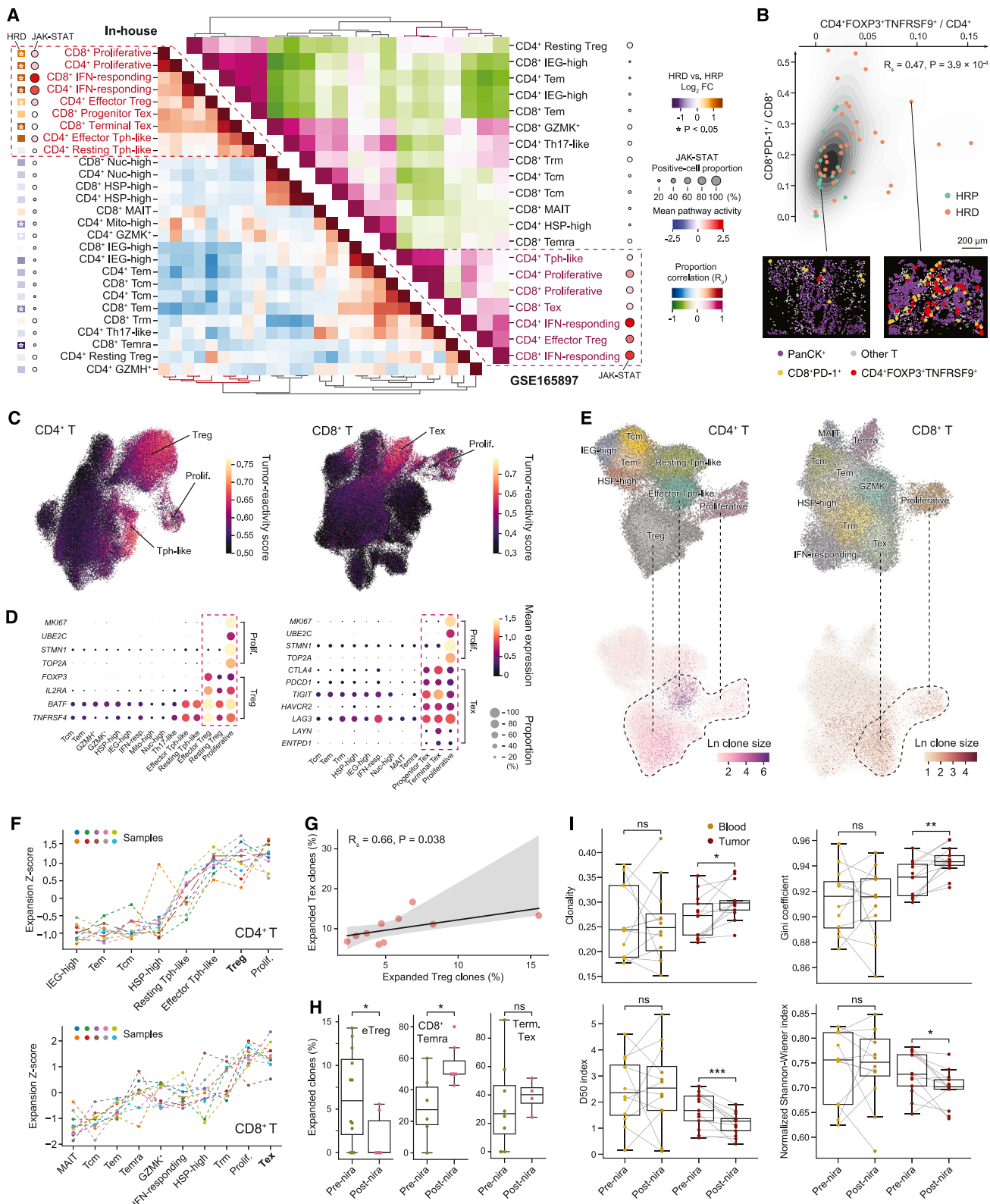
(I) Representative fields of view for pseudocolor (top), cell identity (middle), or the proximity of PanCK$^+$-CD4$^+$FOXP3$^+$ phenotype pairs (bottom) for one HRP tissue and one HRD tissue. Scale bars, 200 μm.

(J) Difference in proportion of FOXP3$^+$, FOXP3$^+$TNFRSF9$^+$, and FOXP3$^+$PD-1$^+$ cells among CD4$^+$ T cells between HRP and HRD samples (left, $n = 18$ HRP samples, $n = 34$ HRD samples) or between pre-nira and post-nira samples (right, $n = 21$ pre-nira samples, $n = 15$ post-nira samples) based on mIHC measurements.

(K) Difference in distribution of panCK$^+$-FOXP3$^+$TNFRSF9$^+$ (left) or panCK$^+$-FOXP3$^+$PD-1$^+$ (right) nearest-neighbor distance between HRP and HRD samples. Vertical lines indicate the median nearest-neighbor distance.

(L) Representative flow cytometry plots of a CD25$^+$CD127^{low} population in all CD4$^+$ T cells and a CCR8$^+$ population in all Tregs.

(M) Difference in the proportion of CD25$^+$CD127^{low} and CD25$^+$CD127^{low}CCR8$^+$ cells among CD4$^+$ T cells between HRP and HRD samples according to flow cytometry results ($n = 8$ HRP samples, $n = 21$ HRD samples for CD25$^+$CD127^{low} cells; $n = 5$ HRP samples, $n = 19$ samples for CD25$^+$CD127^{low}CCR8$^+$ cells).

FC, fold change; R$_s$, Spearman rank correlation coefficient. FPKM, fragments per kilobase of transcript per million mapped reads. For boxplots, the middle line in the box is the mean, the bottom and top of the box are the first and third quartiles, and the whiskers extend to the 1.5× interquartile range of the lower and the upper quartiles, respectively. p values were calculated using a two-sided paired Wilcoxon rank-sum test for (F) and a two-sided unpaired t test for (G), (H), (J), and (M). *$p < 0.05$, **$p < 0.01$, ***$p < 0.001$. See also Figures S2, S3, and S4 and Tables S3, S4, and S7.

Cell
Article

(legend on next page)

Cell
Article

CellPress
OPEN ACCESS

populations, including the eTreg (Figure 2E), suggesting a dominant role of eTreg-centric T cell-state shifts mediating HRD and treatment effects. In further investigating this phenomenon, we identified a cluster of CD4^{+} and CD8^{+} T cell states co-occurring with eTregs and recapitulated the pattern in an independent HGSOC cohort (Figure 3A). Notably, almost all of these T cell populations were enriched in HRD tumors and showed elevated JAK-STAT signaling (Figure 3A). Given that HGSOC tumors with HRD are known to harbor higher tumor mutational burden (TMB)[3,31] and potentially produce more neoantigens,[32] this observation suggested a commonly activated state among the T cells responding to accrued tumor antigens. Indeed, in addition to eTregs,[33,34] this cluster contained several populations known to be enriched for tumor-reactive T cells, such as exhausted CD8^{+} T cells (Texs)[35,36] and CXCL13^{+}PD-1^{+}CXCR5^{−} peripheral T helper-like ("Tph-like") cells (Figure 3A).[37,38] Accordingly, using mIHC, we validated that eTregs and Texs co-occurred and both had a stronger presence in HRD tumors (Figure 3B).

Next, we provided multiple lines of evidence of their tumor reactivity, specifically in our HGSOC context. First, most of the reactive populations showed a uniquely heightened gene expression signature[36] derived from T cells bearing validated neoantigen-specific TCRs (Figure 3C). Second, proliferative CD4^{+} and CD8^{+} T cells expressed Treg and Tex programs, respectively, at a level almost on par with non-proliferative Tregs and Texs (Figure 3D), suggesting that Tregs and Texs bore remarkable proliferative potential. Third, using our paired scRNA-seq/TCR-seq data (Table S5) of enriched tumor-infiltrating T cells, we identified Treg, Tex, Tph-like, and proliferative T cells as the most expanded populations (Figure 3E). Importantly, these expansions were universally strong across all surveyed samples (Figure 3F), demonstrating their robust activation in the HGSOC TME. Finally, Tregs and Texs showed intertumoral co-expansion, again pointing to functional coordination potentially orchestrated by varying tumor antigen burdens (Figure 3G).

Although the co-existence of immunosuppressive eTregs with other activated, reactive T cell populations in HRD tumors presented a well-regulated balance of anti- and pro-tumor forces, the neoadjuvant therapies specifically counteracted eTregs, Treg-like proliferative CD4^{+} T cells, and Tex-like proliferative CD8^{+} T cells (Figure 2C), securing an anti-tumor net effect. To further study the treatment effect from a T cell clonal expansion standpoint, which is an axis of tumor reactivity independent of transcriptional phenotypes, we turned back to our treatment-experienced main scRNA-seq cohort to delineate the longitudinal TCR repertoire dynamics using the TCR repertoire utilities for solid tissue 4 (TRUST4) algorithm (Figure S5A).[39] Supporting the validity of the inferred data, we found that the TCRs (1) were exclusively enriched in transcriptome-defined T cells (Figure S5B), (2) formed clones with extremely high privacy (Figures S5C and S5D), and (3) recapitulated Treg dominance in the CD4^{+} population and overall stronger CD8^{+} expansion, with Tex among the top (Figures S5E and S5F). With these data, the only observed treatment-induced differential expansions after niraparib treatment happened in eTregs and CD8^{+} effector memory re-expressing CD45RA (Temra) cells, with the former suppressed while the latter elevated. By contrast, Tex expansion was not changed by niraparib treatment (Figure 3H). We thus reasoned that the suppression of eTregs by NANT in the HRD TME, both abundance-wise and clonal-expansion-wise, should lead to even more heightened tumor reactivity. Indeed, longitudinally sequenced bulk TCR repertoires of 60 tumors and matched peripheral blood mononuclear cells (PBMCs) from 23 patients in the NANT trial revealed a tumor-restricted significant decrease in TCR diversity and an increase in clonality in most patients (Figure 3I). Together, these results unraveled the complex kinetics of HRD-dependent and therapy-perturbed tumor-reactivity landscape of tumor-infiltrating T cells wherein the key immunoregulatory role of eTregs was highlighted.

Figure 3. HRD drives co-occurring hyper-expanded tumor-reactive T cell populations

(A) Abundance co-variation between CD4^{+} and CD8^{+} T cell states across treatment-naive samples for in-house data (lower triangle) and data from GSE165897 (upper triangle). A cluster of highly correlated cell states containing eTregs is highlighted. Circles on both sides of the main heatmap denote in size the proportion of cells within a cell state with a positive JAK-STAT activity score and in color gradient the mean JAK-STAT activity score. The leftmost squares denote in color gradient the $\log_2$ FC of cell-state abundance in HRD over HRP tumors. Squares with a statistically significant difference are marked by an asterisk. FC, fold change.

(B) Correlation between the proportion of CD4^{+}FOXP3^{+}TNFRSF9^{+} cells among CD4^{+} cells and that of CD8^{+}PD-1^{+} cells over CD8^{+} cells across treatment-naive samples based on mIHC (n = 18 HRP samples, n = 34 HRD samples). Representative cell identity maps highlight the co-occurrence of CD4^{+}FOXP3^{+}TNFRSF9^{+} cells and CD8^{+}PD-1^{+} cells. Scale bars, 200 μm.

(C) UMAP embeddings of CD4^{+} (left) and CD8^{+} (right) T cells showing tumor-reactivity score. Cell states with uniquely high scores are labeled.

(D) Average gene expression levels of state marker genes across CD4^{+} (left) and CD8^{+} (right) T cell states. The circle size denotes the proportion of cells within a cell state where a gene expression is non-zero.

(E) UMAP embeddings of CD4^{+} (left) and CD8^{+} (right) T cells with colors denoting cell-state annotations (top) or color grade representing log-transformed TCR clone size (bottom).

(F) Expansion magnitude of CD4^{+} (top) and CD8^{+} (bottom) T cell states across 10 samples.

(G) Correlation between the proportion of expanded Tregs and that of expanded Texs across 10 samples.

(H) Difference in TCR clonotype expansion proportions of eTreg (left), CD8^{+} Temra (middle), and terminal Tex (right) between pre- and post-niraparib samples (n = 12 pre-nira samples, n = 6 post-nira samples for eTreg; n = 6 pre-nira samples, n = 7 post-nira samples for CD8^{+} Temra; n = 8 pre-nira samples, n = 4 post-nira samples for terminal Tex).

(I) Difference in total clonal diversity between pre- and post-niraparib blood or tumor TCR repertoire, as measured by clonality, Gini coefficient, D50 index, and normalized Shannon-Wiener index (n = 12 patients).

For boxplots, the middle line in the box is the mean, the bottom and top of the box are the first and third quartiles, and the whiskers extend to the 1.5× interquartile range of the lower and the upper quartiles, respectively. R_s, Spearman rank correlation coefficient. p values were calculated using a two-sided Mann-Whitney U test for (A), a two-sided unpaired t test for (H), and a two-sided paired Wilcoxon rank-sum test for (I). ns, non-significant, $*p < 0.05$, $**p < 0.01$, $***p < 0.001$. See also Figure S5 and Tables S5 and S7.
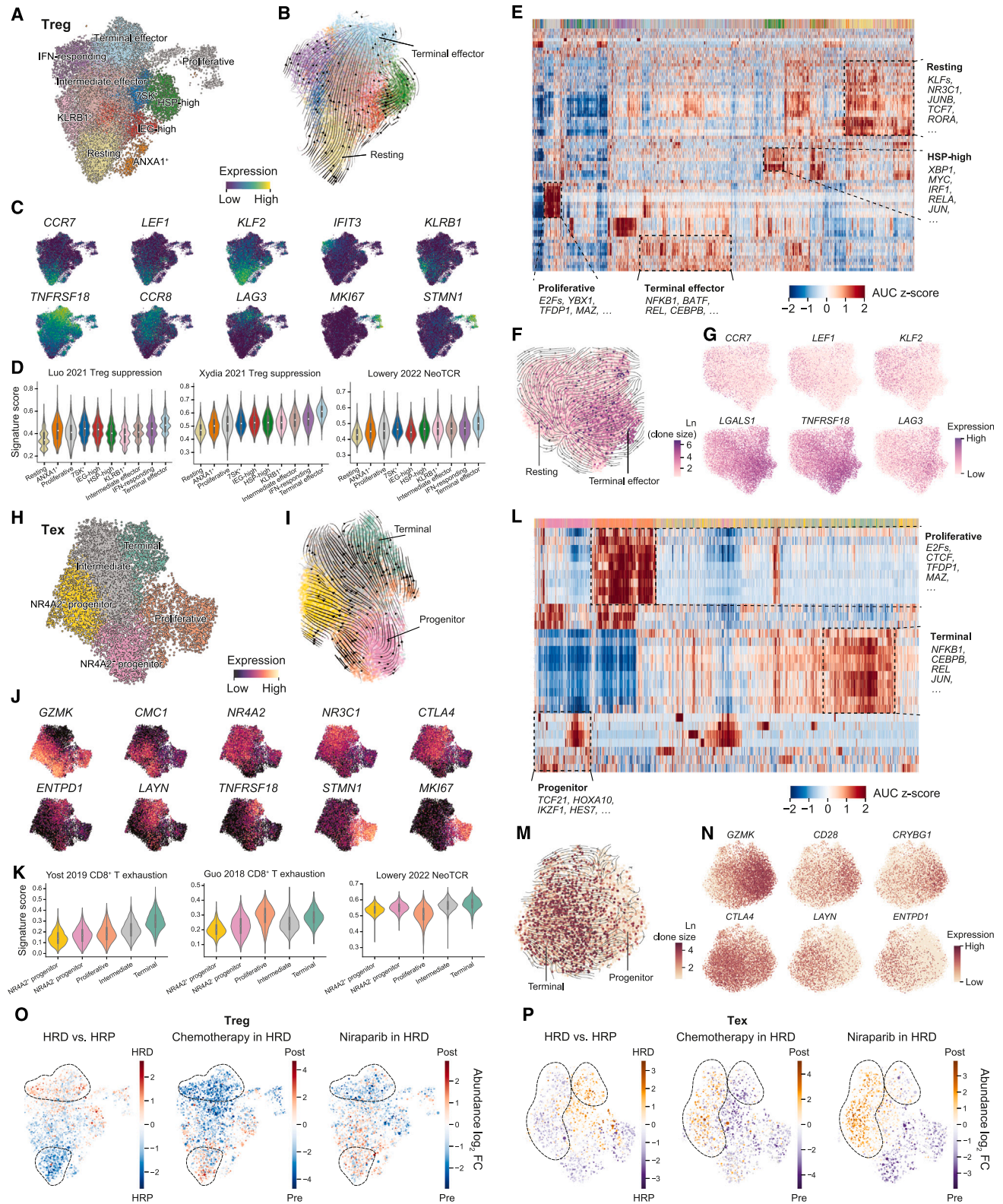
(legend on next page)

Intra-Treg/Tex cell-state shifts driven by HRD and neoadjuvant therapeutic responses

Analysis of tumor-infiltrating Tregs[40–42] and Texs[43–45] has revealed high intra-population heterogeneity for both. However, it remains unclear to what extent Texs behave similarly to and potentially coordinate with their terminally differentiated CD4+ counterparts, eTregs, on a finer scale. Our scRNA-seq data captured >20,000 Tregs and ~10,000 Texs, thereby allowing a deep interrogation into the Treg and Tex sub-states (Figures 4A–4P). We were able to further classify eTregs into 9 sub-states, and along with resting Tregs, we identified 10 sub-states of Tregs in total (Figure 4A); in parallel, we identified 5 sub-states of Texs (Figure 4H). For Tregs, we observed a clear differentiation gradient supported by RNA velocity, with the resting population as the starting point and the terminal effector one as the endpoint (Figure 4B). Texs showed a similar progenitor-to-terminal trajectory by RNA velocity, although with a greater level of complexity (Figure 4I). In Tregs, resting cells highly expressed known T cell naiveness/memory markers such as *CCR7*, *LEF1*, and *KLF2*, while the terminal cells were enriched for Treg markers like *TNFRSF18*, *CCR8*, and *LAG3* (Figure 4C). Similarly, Texs showed a state separation based on enriched expressions of progenitor markers such as *GZMK* or *CMC1* and terminal exhaustion markers such as *ENTPD1* or *LAYN* (Figure 4J). Additionally, both terminally differentiated Tregs and Texs showed the strongest suppression/exhaustion and tumor-reactivity signatures (Figures 4D and 4K). Gene regulatory networks constructed through single-cell regulatory network inference and clustering (SCENIC)[46] revealed state-specific transcription factor activities in Tregs and Texs. Regulons of known lineage drivers, such as TCF7 and NR3C1 for T cell memory and BATF and NFKB1 for Treg maturation, were specifically overrepresented in cells of matched Treg states (Figure 4E). Likewise, Texs exhibited TCF21 and IFZF1 activities in the progenitor state, while NFKB1, REL, CEBPB, and JUN were present in the terminal state (Figure 4L). Beyond their transcriptional states, we recapitulated a clear resting/progenitor-to-terminal trajectory by integrating RNA velocity and clonal expansion in our scRNA-seq/TCR-seq cohort, with the terminal domains enriched for the most expanded clones (Figures 4F and 4M). These state transitions were again confirmed by differential expression patterns of canonical marker genes (Figures 4G and 4N).

Armed with these finest cell-state maps, we next investigated how the interaction between HRD and therapies was manifested through cell-state perturbations within Tregs and Texs. Graph-based differential abundance testing using Milo[47] pinpointed the terminal states of Tregs and Texs as significantly enriched in HRD tumors while depleted after treatment (Figures 4O and 4P). We thus revealed an intriguing consequence of neoadjuvant therapies to be the reversal of Treg and Tex differentiation gradients.

Differential intratumoral and peripheral clonal origins of Tregs and Texs

To further understand how these differentiated and reactive populations were instituted in the TME under HRD and later perturbed by treatment, we interrogated their clonal origins using our scRNA/TCR-seq data. Associating the cell states by their TCR repertoire overlaps, we found CD8+ states to be more extensively exchanged among each other, while CD4+ state exchanges were largely confined to a few cases (Figure 5A). Interestingly, effector Tph-like cells and Tregs had many shared clones, and both showed little overlap with the other CD4+ states. The exception was with the proliferative population, again indicating a tumor-reactive convergence constantly replenished by a proliferative pool (Figures 3A, 3C, and 5A). By contrast, the Tex repertoire in the CD8+ compartment had large overlaps with all effectors as well as the resident memory and the proliferative populations (Figure 5A). There was limited sharing of Texs with central memory cells and Temras, suggesting a differentiation path diverging from the rest of the lineage (Figure 5A).

We then traced Treg and Tex clonal evolution across all individuals by assessing the extent these clones could be found in other populations in the private lineage history of each patient. Tregs showed moderate clonal kinship with proliferative CD4+ T cells in most samples and with Tph-like cells in several samples (Figure 5B). For Texs, besides their strong connection with GZMK+ progenitors, tissue-resident memory (Trm) and several effector subsets provided a possible source as well (Figure 5B). Notably, a TCR repertoire overlap does not necessarily indicate a directional evolutionary relationship between two populations. But overall, our clonal tracing results implicated intratumoral non-Treg and non-Tex populations as the predecessors in the Treg and Tex differentiation trajectories, respectively.

Figure 4. The dynamics of fine-grained Treg and Tex subsets under HRD and neoadjuvant treatment

(A) UMAP embedding of Tregs with colors indicating cell-state annotations.

(B) UMAP embedding of Tregs of the same color annotations in (A) overlayed with streamlines denoting RNA velocity.

(C) UMAP embeddings of Tregs showing gene expression patterns of cell-state markers.

(D) Difference in gene signature scores across Treg cell states.

(E) SCENIC results showing the activities of transcription factor regulons in each cell. Colored bars on top of the heatmap indicate cell-state annotations. The names of cell-state-specific representative transcription factors are highlighted.

(F) UMAP embeddings of Tregs with color grade representing TCR clone size and streamlines indicating RNA velocity.

(G) UMAP embeddings of Tregs showing expression patterns of cell-state gene markers.

(H–N) Same as (A)–(G) but for Texs.

(O) UMAP embedding of Tregs with Milo differential abundance testing results overlayed in color grade. Nodes are neighborhoods, colored by the abundance $\log_2$ FC between HRD and HRP samples (left) or between pre- and post-treatment samples under chemotherapy (middle) or niraparib therapy (right). Node sizes correspond to the number of cells in each neighborhood. Areas with strong enrichment signals are highlighted with a black dashed circle. FC, fold change.

(P) Same as (O) but for Texs.

See also Table S7.
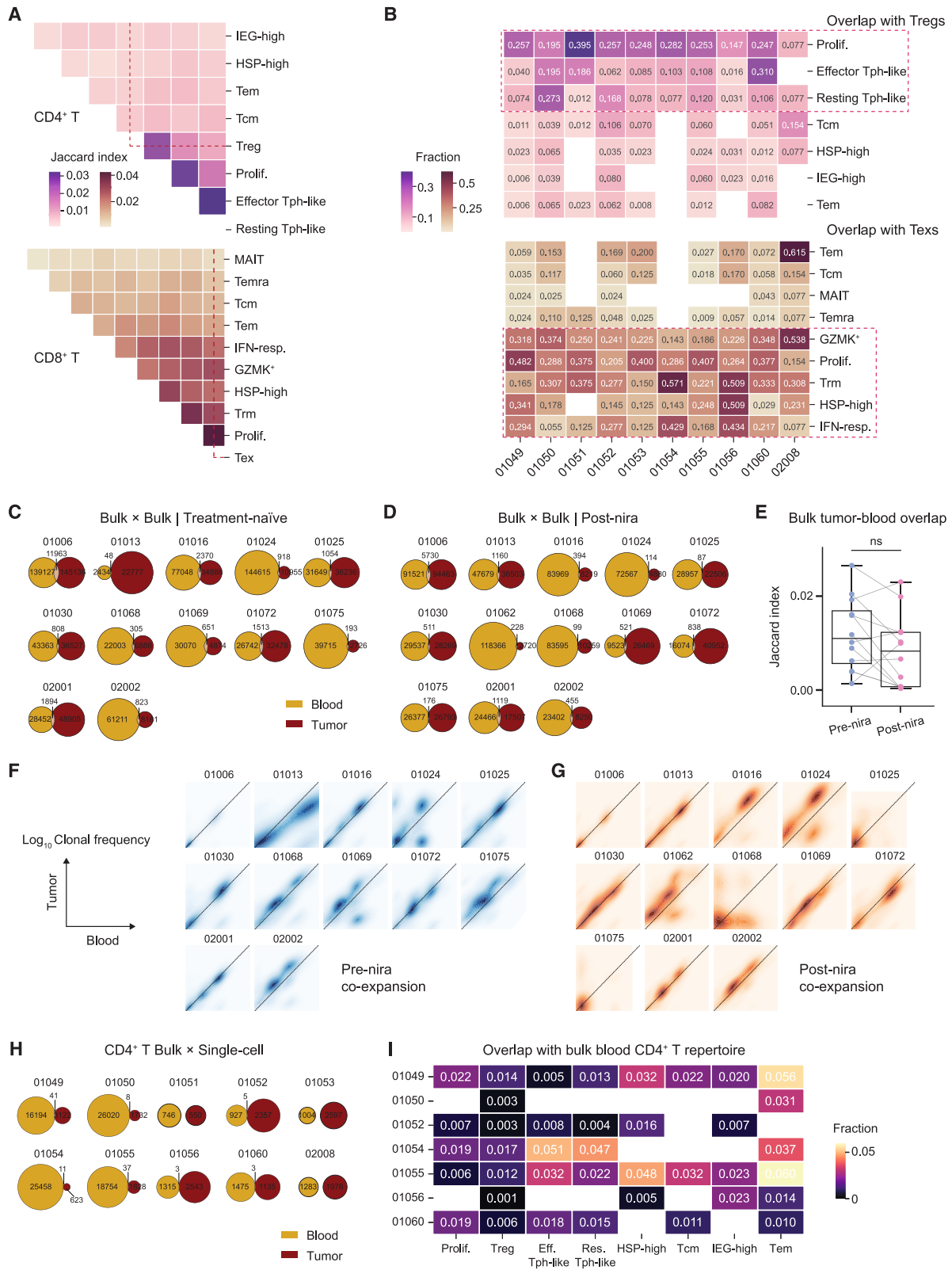
(legend on next page)

Cell
Article

Several studies have suggested, outside of the induction from conventional CD4+ T cells, a possibility of peripheral replenishment of tumor-infiltrating Tregs, albeit in a context-specific manner.[42,48] To gauge how frequently tumor and blood TCR repertoire engaged in crosstalk in HGSOC, we first calculated the blood-tumor repertoire overlap across patients using our bulk TCR-seq data (Table S6). The proportion of shared clones varied greatly across individuals and was independent of niraparib treatment (Figures 5C–5E). Importantly, for most individuals, overlapped clones showed a strong co-expansion pattern, indicating an effective clonal supplement from the circulation (Figures 5F and 5G).

Since bulk TCR-seq data lacked a cell-state resolution, we directly searched for the peripheral presence of intratumoral Treg clones by profiling bulk TCR repertoires of purified blood CD4+ T cells from the same patients in our scRNA-seq/TCR-seq cohort (Table S6). Surprisingly, this analysis revealed negligible clonal exchanges between the two compartments (Figure 5H). Few CD4+ cell states had >5% of their TCR clones found in the periphery blood, and Tregs showed the weakest signals with an average overlap of <1% (Figure 5I). Thus, Tregs seemed to possess a strong but tumor-restricted self-expansion capability through a constant exchange with the CD4+ proliferative pool. By contrast, highly expanded Texs could converge from multiple effector CD8+ subsets.

IFN-induced MHC class II expression in HRD tumor cells potentially contributes to eTreg enrichment
To understand where terminal eTregs or terminal Texs, two populations of the utmost interest based on our previous analyses, were positioned in a hierarchical and coordinated TME response, we examined TME-wide the cell states they co-occur with. Interestingly, such cell states were commonly marked by the activation of IFN signaling (Figures 6A and 6D). These included M1-like macrophages, IFN-responding myCAFs, IFN-responding cancer cells, and THY1+ pericytes (Figures 6A and 6D). Importantly, the direction and magnitude of these co-variations were strictly aligned with the Treg/Tex differentiation gradients (Figures 6B and 6E). Additionally, they remained significant when we switched the calculation of cell-state proportion to one level above, namely eTregs over CD4+ T cells and Texs over CD8+ T cells (Figures S6A–S6F).

Behaviors of cancer cells are fundamental driving forces of the TME and are often the direct targets of chemotherapy and targeted therapies such as niraparib.[49] Among the three major cancer cell populations in our dataset, the IFN-responding population strongly co-occurred with terminal eTregs (Figure 6C)

and, to a lesser extent, with terminal Texs (Figure 6F). To understand how IFN-responding cancer cells would specifically contribute to Treg enrichment, we first evaluated the differential antigen-dependent Treg interactions among cancer cell states by comparing their antigen presentation machinery expressions. Interestingly, IFN-responding cancer cells, enriched in HRD tumors (Figure 6G), had significantly upregulated major histocompatibility complex (MHC) class II expressions. MHC class I genes already had a strong presence at baseline in non-IFN-responding states and were of even higher abundance in the IFN-responding population (Figure 6H). This reflected a well-established role of IFN in upregulating both MHC class I and MHC class II gene expression through activating the master regulators, CITA and CIITA.[50,51]

Epithelial cells, especially those lining the intestine, have long been known to possess MHC class II-dependent Treg-promoting capabilities.[52,53] However, only recently have several lines of evidence emerged to support a similar model in tumor contexts.[54,55] In our data, IFN-responding cancer cells did not express CD80/86 genes at all and had minimal expressions of most alternative co-stimulatory molecules (Figure 6H). This was in sharp contrast to canonical antigen-presenting cells such as dendritic cells and macrophages, which not only possessed a full set of MHC class I/MHC class II complexes but had a strong presence of co-stimulatory genes (Figures 6H and S6G). We further observed that even in the other cancer cell populations not typified by enhanced IFN signaling, HRD had a strong positive contribution to elevated MHC class II gene expressions, based on a transcriptome-wide pseudobulk analysis (Figure 6I). This close connection between HRD and MHC class II activation is well aligned with HRD-driven genomic instability being a major activator of the cyclic GMP-AMP synthase (cGAS)-stimulator of interferon genes (STING) DNA sensing pathway.[56,57] Conversely, the expression level of MHC class I genes showed no difference between HRD and HRP cancer cells in all three states (Figures S6H and S6I). To validate these findings, we experimentally demonstrated the MHC class II responsiveness to IFN treatment or BRCA1/2 deficiency in multiple ovarian or breast cancer cell lines (Figure 6J). Therefore, interacting with MHC class II-positive cancer cells for CD4+ T cells may lead to a Treg phenotype through aberrant stimulation of the TCR signaling without essential subsequent co-stimulatory signals.[58,59]

Besides passively sequestering T cells into regulatory and dysfunctional states, cancer cells may actively propagate suppressive signaling through the upregulation of co-inhibitory molecules.[58,60] Indeed, our sample-level analysis showed

Figure 5. Tracing Treg/Tex origins in the TME and the circulation
(A) TCR repertoire overlaps between CD4+ (top) and CD8+ (bottom) T cell states.
(B) Fraction of Treg clonotypes found in non-Treg cells (top) or of Tex clonotypes found in non-Tex cells (bottom) across samples.
(C and D) Number of TCR clonotypes shared between matched PBMC and tumor samples for pre- (C) or post-niraparib (D) patients based on bulk TCR-seq.
(E) Difference in blood and tumor repertoire overlap between pre- and post-niraparib samples (n = 12 patients, two-sided paired Wilcoxon rank-sum test, ns, non-significant).
(F and G) TCR repertoire co-expansion between PBMC and patient-matched tumor across pre- (F) and post-niraparib (G) samples.
(H) Number of CD4+ TCR clonotypes shared between matched PBMC and tumor samples for treatment-naive patients based on bulk TCR-seq and scTCR-seq, respectively.
(I) Fraction of intratumoral TCR clonotypes observed in sample-matched PBMC across CD4+ T cell states.
See also Tables S5 and S6.
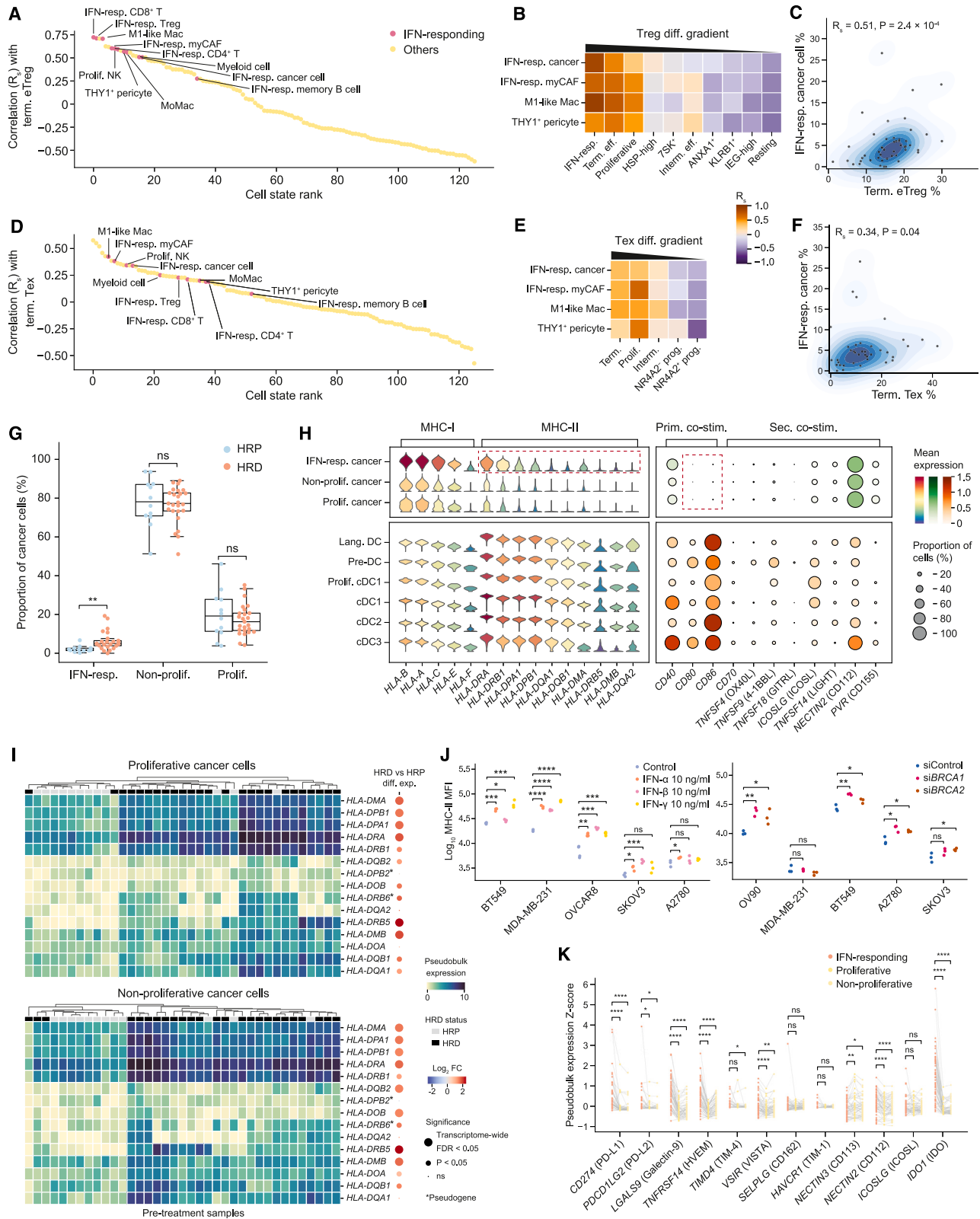
(legend on next page)

strongly increased expressions of many co-inhibitory molecules in IFN-responding cancer cells (Figure 6K), including factors with established roles in favoring Texs and/or Tregs, such as PD-L1,[61,62] Galectin-9,[63,64] indoleamine 2,3-dioxygenase (IDO),[65,66] and ICOSL.[67,68]

Treg depletion as an effective therapeutic strategy to suppress HRD tumors

Our systematic analyses highlighted the abundant enrichment of immunosuppressive eTregs in HRD tumors and their marked post-treatment reduction, which may be a key contributor to the HRD-dependent clinical benefits of PARP inhibition in HGSOC patients. Indeed, eTregs appeared as one of the peripheral immune subsets significantly reduced by maintenance PARPi in epithelial ovarian cancer patients in a recent translational study.[69] In our NANT trial, the post-treatment CA125 level across patients showed a strong positive correlation with the proportion of tumor-infiltrating terminal eTregs (Figure 7A). This link between patient response and remaining eTregs prompted us to hypothesize that directly targeting eTregs in combination with niraparib would achieve an improved tumor-suppressing effect in the HRD context.

To test this hypothesis, we utilized a humanized therapeutic monoclonal antibody (mAb), ZL-1218, currently being tested to treat advanced solid tumors in a phase I clinical trial (NCT05859464), to target a well-established phenotypic and therapeutic eTreg marker, CCR8.[70–72] To evaluate its efficacy, we first constructed an orthotopic HGSOC mouse model through intrabursal injection of ID8-Luc cells with CRISPR-edited *Trp53* and *Brca1* into *CCR8*-humanized (h*CCR8*) mice. These HRD *Trp53*$^{-/-}$ tumors harbored a significantly higher proportion of eTregs and terminal Texs than their HRP counterparts, demonstrating human HGSOC relevance (Figure 7B). We then administered niraparib and/or CCR8 mAb to tumor-bearing mice after about 2 weeks of transplantation (Figure 7C). Although tumor progression was attenuated by niraparib or CCR8 mAb alone, their combination indeed showed a significantly more pronounced inhibitory effect (Figures 7D–7F). Importantly, the development of hemorrhagic ascites, a lethal hallmark of ovarian cancer,[73,74] was dramatically curbed by the combination ther-apy (Figure 7G). PD-1$^+$ Treg frequency was significantly reduced by all therapies, with the largest reduction seen in the combination treatment group, as measured independently by flow cytometry (Figure 7H) and IHC (Figures 7I and 7J). In addition to CCR8 targeting, we explored another Treg-depleting therapy and observed similar anti-tumor effects in conjunction with PARP inhibition. Specifically, niraparib and CD25 mAb together (Figure 7K) significantly slowed tumor progression (Figures 7L and 7M), prevented hemorrhagic ascites (Figure 7N), and dampened PD-1$^+$ Tregs (Figure 7O) in the same orthotopic model but without the humanized *CCR8*. Exhibiting broader applicability, the combination regimen had its superior anti-tumor effect recapitulated in two orthotopic breast cancer mouse models, namely h*CCR8* mice bearing *Brca2*-deficient EO771 cells (Figures 7P–7R) or wild-type (WT) mice bearing *Brca1*-deficient EO771 cells (Figures 7S–7U), both at the inguinal mammary fat pad. Notably, the non-response to single-agent niraparib in the *Brca2*$^{-/-}$ breast cancer model stood in contrast to responses in the *Brca1*$^{-/-}$ models, likely because *BRCA1* and *BRCA2* mutations differentially reshaped the TME in different cancer contexts. Finally, we evaluated the potential toxicities induced by different therapies with routine blood and biochemical examinations in mice. Notably, there was no significant myelosuppression (Figures S7A and S7B) or tissue damage (Figures S7C and S7D) in mice treated with the combination therapy compared with those receiving the monotherapy or control. Thus, the depletion of eTregs by combining niraparib and CCR8/CD25 mAbs represents a promising intervention strategy for tumors harboring HRD. Further investigations are merited to determine whether the combination therapy can provide long-term memory responses and survival benefits.

DISCUSSION

Through comprehensive profiling of a neoadjuvant trial cohort, our study was endowed with a unique "window of opportunity"[75] to investigate for the first time the interaction effects of HRD and PARP inhibition on the TME of treatment-naive HGSOC tumors. Although previous *in vitro* and preclinical studies showed that PARP-1 deletion or inhibition promotes Treg differentiation and

---

Figure 6. IFN-responding cancer cells contribute to Treg induction through MHC class II

(A) Ranking of cell types and cell states by abundance co-variation with terminal eTregs (among all Tregs) across all samples.

(B) Abundance co-variation between top IFN-responding cell states and all Treg cell states (among all Tregs).

(C) Abundance co-variation between IFN-responding cancer cells (among all cancer cells) and terminal eTregs (among all Tregs) (*n* = 48 samples).

(D–F) Same as (A)–(C) but for terminal Texs (F, *n* = 38 samples).

(G) Difference in cancer cell-state proportion between pre-treatment HRD and HRP samples (*n* = 12 HRP samples, *n* = 25 HRD samples). For boxplots, the middle line in the box is the mean, the bottom and top of the box are the first and third quartiles, and the whiskers extend to the 1.5× interquartile range of the lower and the upper quartiles, respectively.

(H) Average expression levels of MHC class I and MHC class II genes (left) or of primary and secondary co-stimulatory T cell ligand genes (right) across cancer (top) and DC (bottom) cell states. Circle size denotes the proportion of cells within a cell state where a gene expression is non-zero. Labels in parentheses are common protein names.

(I) Pseudobulk (sample-average) expression levels of MHC class II genes in proliferative (left) and non-proliferative cancer cells (right). Heatmaps on the top show the HRD status of each pre-treatment sample. Colored dots on the right indicate pseudobulk DESeq2 results where the color denotes log$_2$ fold change, and the size denotes statistical significance.

(J) Change of log-transformed MHC class II MFI in IFN-treated (left) or *BRCA1/2*-deficient (right) cells (*n* = 3 replicates).

(K) Difference in pseudobulk gene expression *Z* scores of co-inhibitory molecules among cancer cell states (*n* = 67 samples). Lines connect data points of the same sample. Labels in parentheses are common protein names.

DC, dendritic cell; MFI, median fluorescence intensity; R$_s$, Spearman rank correlation coefficient. *p* values were calculated using a two-sided unpaired t test for (G) and (J) and a two-sided paired t test for (K). ns, non-significant, *p < 0.05, **p < 0.01, ***p < 0.001, ****p < 0.0001. See also Figure S6.

(legend on next page)

Cell
Article

CellPress
OPEN ACCESS
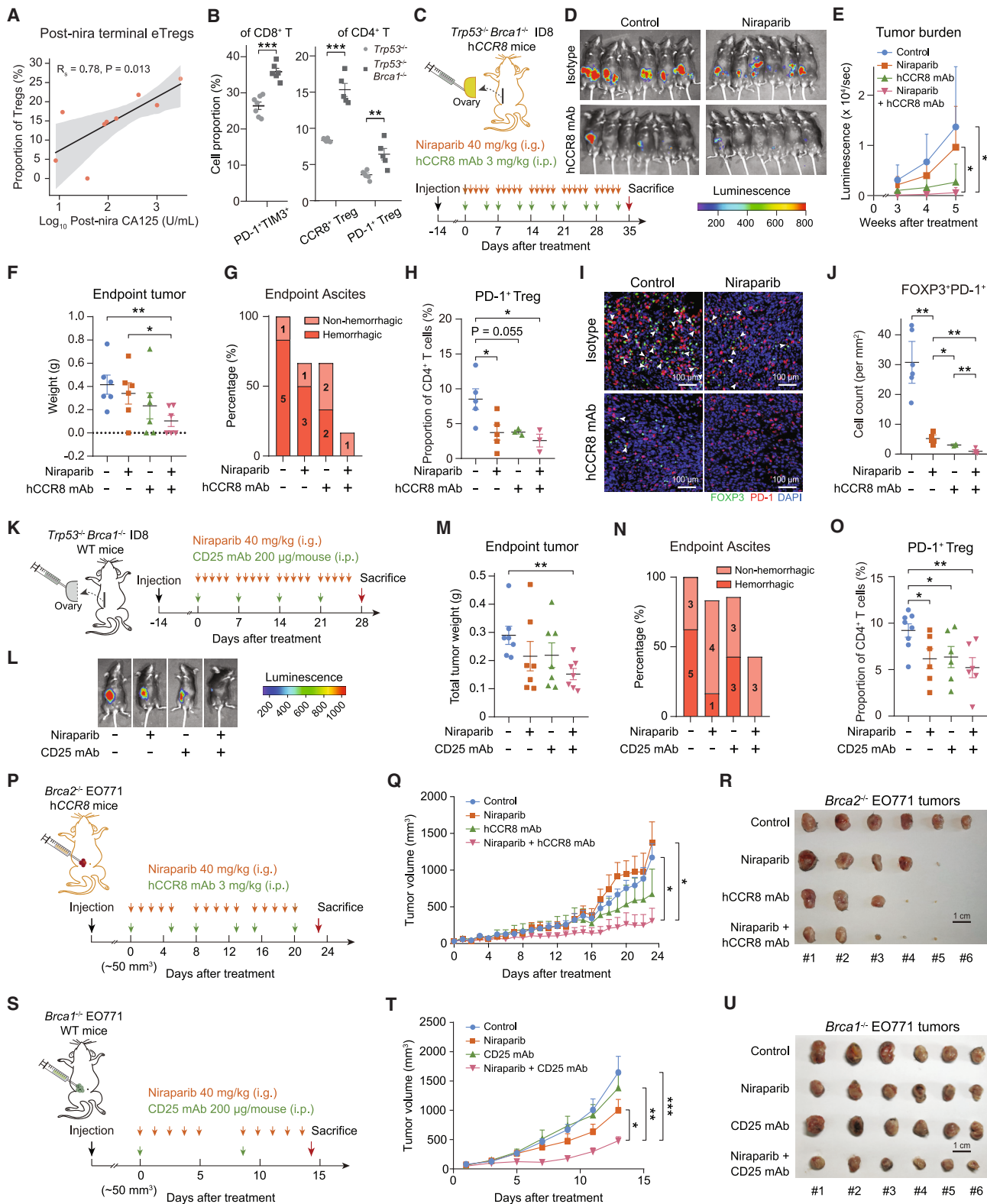
suppressive functions in non-cancer contexts,[76–79] our observation of eTreg depletion by PARPi is the net effect of a series of complex TME events, succeeding a collective emergence of eTregs and Texs in response to heightened TMB induced by HRD. In searching for an underlying mechanism, we identified a group of HRD-enriched IFN-responding cancer cells bearing aberrantly high expressions of MHC molecules and co-inhibitory ligands while lacking co-stimulatory molecules, thus potentially reinforcing the presence of Tregs/Texs.

Although IFN signaling has traditionally been deemed as an essential stimulator of anti-tumor immunity, recent studies have revealed its central role in immune surveillance and escape through both tumor-intrinsic and microenvironmental mechanisms.[80–84] The net effect of IFN on the TME may heavily rely on the location, timing, and duration of exposure. Depending on the tissue context and progression status of a tumor, these parameters can drastically vary among cancer patients. Considering this, chronic IFN signaling underlying adaptive immunosuppression is particularly relevant in HGSOC because most HGSOC tumors are diagnosed at an advanced stage with widespread affected areas.[85,86] A long latency period as such allows HGSOC tumors with genomic instability to produce IFN persistently.

In our data, rampant IFN signaling leads to widespread immunoediting within the TME, manifested through the delicate balance where the emergence of immunosuppressive eTregs goes hand in hand with the surge of tumor-reactive effector T cells. Echoing a recent study by Oliveira et al. that established tumor-reactive Tregs to be a major mediator of immune evasion in high-TMB melanoma,[54] our study hints at, in the absence of direct evidence supporting Treg tumor reactivity, a similar maneuver adopted by HGSOC and potentially HRD tumors in general. Accordingly, when the anti-CCR8 mAb was used to directly and highly specifically deplete eTregs, HRD tumors were effectively suppressed in multiple syngeneic mouse

models. Our strategy highlighted a focus on removing the dominant immunosuppressive force to secure a net gain of anti-tumor effects. However, HRD is a unique genomic feature whose definition and utility are largely restricted to a few cancer types (e.g., ovarian cancer, breast cancer, and prostate cancer). The extent to which the effect of HRD on the TME can be generalized to other cancer types with different kinds of genomic instability is a key question in future research.

In summary, our in-depth analysis of patient samples from a well-controlled trial cohort together with mechanistic interrogations in highly relevant preclinical models (1) revealed cancer-cell-extrinsic mechanisms underlying HRD as a valuable biomarker; (2) confirmed the potential of niraparib as a candidate for chemo-free neoadjuvant therapeutics; and (3) unraveled a rational realm of eTreg-centered immunotherapeutic opportunities in HGSOC. Future efforts are warranted to take this potential to transform the current treatment landscape where well-established ICIs have failed to generate promising responses.

Limitations of the study

Our study has several limitations regarding data collection, analysis, and interpretation. First, we heavily relied on scRNA-seq data to derive cell type/state proportions, which may obscure the measurements of certain populations due to sampling and processing bias. However, for our major focus, the T lymphocytes, mIHC and flow cytometry analyses on a large number of tumor samples validated the findings regarding Treg enrichment in HRD and reduction after treatment. Second, previous studies have demonstrated intratumoral or site-specific TME heterogeneity by profiling multiple tumor sites within a patient. Our analysis did not consider this factor, mainly due to ensuring and maximizing patient well-being in obtaining pre-treatment diagnostic laparoscopic biopsies to avoid additional trauma and bleeding. Also, maximizing the patient count per cohort ensured

---

Figure 7. eTreg depletion combined with PARP inhibition reduces HGSOC burden

(A) Correlation between the CA125 level of post-niraparib patients and the proportion of terminal eTregs (among all Tregs) in their tumors. R_s, Spearman rank correlation coefficient.

(B) Difference in the proportion of terminal Texs among CD8$^+$ cells (left, n = 6–7 mice/group) or CCR8$^+$/PD-1$^+$ Tregs among all CD4$^+$ cells (right, n = 5–7 mice/group) between $Trp53^{-/-}$ $Brca1^{-/-}$ and $Trp53^{-/-}$ ID8 tumors.

(C) Schematic illustration of $Trp53^{-/-}$ $Brca1^{-/-}$ ID8 cells transplanted into $CCR8$-humanized (h$CCR8$) mice via intrabursal injection 2 weeks before treatment with niraparib (i.g.) and/or CCR8 mAb (i.p.) (n = 6 mice/group).

(D) Bioluminescent images of all mice in each group.

(E) Dynamics of tumor burdens at 3, 4, and 5 weeks of treatment, as monitored by luminescence intensity (n = 6 mice/group).

(F–H) Difference in the weight of surgically resected tumors (F, n = 6 mice/group), the percentage of mice with hemorrhagic or non-hemorrhagic ascites (G, n = 6 mice/group), or the proportion of PD-1$^+$ Tregs among CD4$^+$ cells in the tumor (H, n = 3–5 mice/group) at endpoint among treatment groups.

(I) Representative immunofluorescent images showing FOXP3 (green), PD-1 (red), and nucleus (blue). White arrows mark FOXP3$^+$PD-1$^+$ cells. Scale bars, 100 μm.

(J) Difference in the density of FOXP3$^+$ (left) or FOXP3$^+$PD-1$^+$ (right) cells among treatment groups (n = 3–6 mice/group). 4 fields of view were randomly selected for each slide to obtain an average count.

(K) Schematic illustration of $Trp53^{-/-}$ $Brca1^{-/-}$ ID8 cells transplanted into wild-type (WT) mice via intrabursal injection 2 weeks before treatment with niraparib (i.g.) and/or CD25 mAb (i.p.) (n = 7–8 mice/group).

(L–O) Same as (D) and (F)–(H) but for niraparib (i.g.) and/or CD25 mAb (i.p.) in wild-type (WT) mice (M, n = 7 mice/group; O, n = 6–7 mice/group).

(P) Schematic illustration of $Brca2^{-/-}$ EO771 cells transplanted into the inguinal mammary fat pad of h$CCR8$ mice and the administration of niraparib (i.g.) and/or CCR8 mAb (i.p.) (n = 6 mice/group) after the tumor volume reached ~50 mm^3.

(Q) Change in tumor volumes at multiple time points among treatment groups (n = 6 mice/group, two-way analysis of variance, $^*p$ < 0.05).

(R) Images of surgically resected $Brca2^{-/-}$ EO771 tumors at endpoint among treatment groups. Scale bars, 1 cm.

(S–U) Same as (P)–(R) but for niraparib (i.g.) and/or CD25 mAb (i.p.) in WT mice (T, n = 6 mice/group; U, scale bars, 1 cm).

i.g., intragastric administration; i.p., intraperitoneal administration. Data are shown as mean values ± SEM. p values were calculated using a two-sided unpaired t test except for (Q) and (T) where two-way analysis of variance (ANOVA) was used. $^*p$ < 0.05, $^{**}p$ < 0.01, $^{***}p$ < 0.001. See also Figure S7.

CellPress
OPEN ACCESS

Cell
Article

sufficient statistical power for inter-tumor comparisons, which is a focus of our study. Third, we used computational methods to infer key biological processes from our scRNA-seq data, such as longitudinal TCR repertoire dynamics and Tex differentiation trajectory. Although these inference data cannot replace direct measurements, subsequent multifaceted analyses validated good inference quality and led to important discoveries that would otherwise be masked.

STAR★METHODS

Detailed methods are provided in the online version of this paper and include the following:

- KEY RESOURCES TABLE
- RESOURCE AVAILABILITY
  - Lead contact
  - Materials availability
  - Data and code availability
- EXPERIMENTAL MODEL AND STUDY PARTICIPANT DETAILS
  - Patient recruitment and sample collection
  - Animals
- METHOD DETAILS
  - Sample collection and processing
  - HRD assay
  - scRNA-seq library preparation and sequencing
  - Flow cytometry and sorting for scTCR-seq and bulk TCR-seq
  - scTCR-seq library preparation and sequencing
  - Bulk RNA isolation and TCR sequencing
  - Flow cytometry for Treg quantification in human tumors
  - Multiplex immunohistochemistry (mIHC)
  - Cell culture and treatment
  - Transfection of small interfering RNA (siRNA)
  - Total RNA extraction and real-time PCR
  - CRISPR/Cas9
  - Mouse models
  - Flow cytometry for Treg and Tex quantification in mouse tumors
  - Dual-target immunofluorescence for Treg quantification in mouse tumors
  - HRD and mutation analysis
  - scRNA-seq data preprocessing and quality control
  - scRNA-seq data integration and annotation
  - scRNA-seq data analysis of T cells in an external cohort
  - Comparative and correlative analysis of cell state proportions
  - Graph-based differential abundance testing
  - Inference of eTreg infiltration in bulk RNA-seq data
  - RNA velocity analysis
  - Gene regulatory network analysis
  - Paired scRNA/TCR-seq data analysis
  - TCR clonotype reconstruction from non-VDJ-enriched scRNA-seq data
  - Bulk TCR-seq data processing and analysis
  - Pseudobulk analysis
  - mIHC Image analysis
- QUANTIFICATION AND STATISTICAL ANALYSIS

SUPPLEMENTAL INFORMATION

Supplemental information can be found online at https://doi.org/10.1016/j.cell.2024.06.013.

ACKNOWLEDGMENTS

AUTHOR CONTRIBUTIONS

Y.L., Y.X., D.L., Xiong Li, D.M., Y.F., H. Liang, and Q.G. designed the study. Y.X., H. Li, J.L., D.Z., Xin Li, Y.Q., C.X., K.T., G.L., S.X., Z.W., T.F., S.W., Z.P., P.J., N.J., S.S., Y.C., M. Wang, X. Jiao, M.L., W.G., Y.W., and G.Z. processed tissue biopsies. H. Li, J.L., Z.W., and X.H. generated scRNA-seq libraries. Y.L., D.L., Xiong Li, Y.Z., W.P., Q.Z., and X. Liu performed data processing, and Y.L., D.L., and Y.X. performed published analyses. Y.F., H. Liang, and Q.G. guided computational analysis. Y.X., Y.Y., and Y.D. generated scRNA-seq/VDJ-seq libraries. Y.Z., Y.Y., Y.D., and X. Ji performed mutation calling analysis. Q.G. led the clinical trial and oversaw sample allocation. Ronghua Liu, W.Z., W.S., Z.H., Rong Liu, M. Wu, G.C., L.H., D.M., Y.F., and Q.G. contributed to clinical trial oversight and execution. D.M. provided advice on the study design. Y.L., Y.X., D.L., Xiong Li, H. Li, Y.Z., S.X., H. Liang, and Q.G. wrote the paper with input from all authors.

DECLARATION OF INTERESTS

Y.Y., Y.D., Y.Z., X.H., and X. Ji are full-time employees and H. Liang is a shareholder and scientific advisor of Precision Scientific Ltd. Z.H. is a full-time employee of BioMap Intelligence Technology.

REFERENCES

1. Heeke, A.L., Pishvaian, M.J., Lynce, F., Xiu, J., Brody, J.R., Chen, W.-J., Baker, T.M., Marshall, J.L., and Isaacs, C. (2018). Prevalence of homologous recombination–related gene mutations across multiple cancer types. JCO Precis. Oncol. 2, 1–13. https://doi.org/10.1200/po.17.00286.

2. Nguyen, L., W M Martens, J., Van Hoeck, A., and Cuppen, E. (2020). Pan-cancer landscape of homologous recombination deficiency. Nat. Commun. 11, 5584. https://doi.org/10.1038/s41467-020-19406-4.

3. Rempel, E., Kluck, K., Beck, S., Ourailidis, I., Kazdal, D., Neumann, O., Volckmar, A.L., Kirchner, M., Goldschmid, H., Pfarr, N., et al. (2022). Pan-cancer analysis of genomic scar patterns caused by homologous repair deficiency (HRD). NPJ Precis. Oncol. 6, 36. https://doi.org/10.1038/s41698-022-00276-6.

4. Farmer, H., McCabe, N., Lord, C.J., Tutt, A.N.J., Johnson, D.A., Richardson, T.B., Santarosa, M., Dillon, K.J., Hickson, I., Knights, C., et al. (2005). Targeting the DNA repair defect in BRCA mutant cells as a therapeutic strategy. Nature 434, 917–921. https://doi.org/10.1038/nature03445.

5. Bryant, H.E., Schultz, N., Thomas, H.D., Parker, K.M., Flower, D., Lopez, E., Kyle, S., Meuth, M., Curtin, N.J., and Helleday, T. (2005). Specific killing of BRCA2-deficient tumours with inhibitors of poly(ADP-ribose) polymerase. Nature 434, 913–917. https://doi.org/10.1038/nature03443.

6. Groelly, F.J., Fawkes, M., Dagg, R.A., Blackford, A.N., and Tarsounas, M. (2023). Targeting DNA damage response pathways in cancer. Nat. Rev. Cancer 23, 78–94. https://doi.org/10.1038/s41568-022-00535-5.

7. Gao, Q., Zhu, J., Zhao, W., Huang, Y., An, R., Zheng, H., Qu, P., Wang, L., Zhou, Q., Wang, D., et al. (2022). Olaparib maintenance monotherapy in Asian patients with platinum-sensitive relapsed ovarian cancer: Phase III trial (L-MOCA). Clin. Cancer Res. 28, 2278–2285. https://doi.org/10.1158/1078-0432.CCR-21-3023.

8. Trigos, A.S., Pasam, A., Banks, P., Wallace, R., Guo, C., Keam, S., Thorne, H., kConFab, Mitchell, C., Lade, S., et al. (2022). Tumor immune microenvironment of primary prostate cancer with and without germline mutations in homologous recombination repair genes. J. Immunother. Cancer 10, e003744. https://doi.org/10.1136/jitc-2021-003744.

9. Launonen, I.M., Lyytikäinen, N., Casado, J., Anttila, E.A., Szabó, A., Hal-tia, U.M., Jacobson, C.A., Lin, J.R., Maliga, Z., Howitt, B.E., et al. (2022). Single-cell tumor-immune microenvironment of BRCA1/2 mutated high-grade serous ovarian cancer. Nat. Commun. 13, 835. https://doi.org/10.1038/s41467-022-28389-3.

10. Mehta, A.K., Cheney, E.M., Hartl, C.A., Pantelidou, C., Oliwa, M., Castril-lon, J.A., Lin, J.R., Hurst, K.E., de Oliveira Taveira, M., Johnson, N.T., et al. (2021). Targeting immunosuppressive macrophages overcomes PARP inhibitor resistance in BRCA1-associated triple-negative breast cancer. Nat. Cancer 2, 66–82. https://doi.org/10.1038/s43018-020-00148-7.

11. Vázquez-García, I., Uhlitz, F., Ceglia, N., Lim, J.L.P., Wu, M., Mohibullah, N., Niyazov, J., Ruiz, A.E.B., Boehm, K.M., Bojilova, V., et al. (2022). Ovarian cancer mutational processes drive site-specific immune evasion. Nature 612, 778–786. https://doi.org/10.1038/s41586-022-05496-1.

12. Wright, A.A., Bohlke, K., Armstrong, D.K., Bookman, M.A., Cliby, W.A., Coleman, R.L., Dizon, D.S., Kash, J.J., Meyer, L.A., Moore, K.N., et al. (2016). Neoadjuvant chemotherapy for newly diagnosed, advanced ovarian cancer: Society of Gynecologic Oncology and American Society of Clinical Oncology Clinical Practice Guideline. J. Clin. Oncol. 34, 3460–3473. https://doi.org/10.1200/JCO.2016.68.6907.

13. Liu, J., Jiao, X., and Gao, Q. (2020). Neoadjuvant chemotherapy-related platinum resistance in ovarian cancer. Drug Discov. Today 25, 1232–1238. https://doi.org/10.1016/j.drudis.2020.04.015.

14. Peng, Z., Li, M., Li, H., and Gao, Q. (2023). PD-1/PD-L1 immune check-point blockade in ovarian cancer: dilemmas and opportunities. Drug Dis-cov. Today 28, 103666. https://doi.org/10.1016/j.drudis.2023.103666.

15. Hamanishi, J., Takeshima, N., Katsumata, N., Ushijima, K., Kimura, T., Takeuchi, S., Matsumoto, K., Ito, K., Mandai, M., Nakai, H., et al. (2021). Nivolumab versus gemcitabine or pegylated liposomal doxoru-bicin for patients with platinum-resistant ovarian cancer: open-label, ran-domized trial in Japan (NINJA). J. Clin. Oncol. 39, 3671–3681. https://doi.org/10.1200/JCO.21.00334.

16. Pujade-Lauraine, E., Fujiwara, K., Ledermann, J.A., Oza, A.M., Kristeleit, R., Ray-Coquard, I.L., Richardson, G.E., Sessa, C., Yonemori, K., Bane-rjee, S., et al. (2021). Avelumab alone or in combination with chemo-therapy versus chemotherapy alone in platinum-resistant or platinum-re-fractory ovarian cancer (JAVELIN Ovarian 200): an open-label, three-arm, randomised, phase 3 study. Lancet Oncol. 22, 1034–1046. https://doi.org/10.1016/S1470-2045(21)00216-3.

17. Monk, B.J., Colombo, N., Oza, A.M., Fujiwara, K., Birrer, M.J., Randall, L., Poddubskaya, E.V., Scambia, G., Shparyk, Y.V., Lim, M.C., et al. (2021). Chemotherapy with or without avelumab followed by avelumab maintenance versus chemotherapy alone in patients with previously un-treated epithelial ovarian cancer (JAVELIN Ovarian 100): an open-label, randomised, phase 3 trial. Lancet Oncol. 22, 1275–1289. https://doi.org/10.1016/S1470-2045(21)00342-9.

18. Kurtz, J.E., Pujade-Lauraine, E., Oaknin, A., Belin, L., Leitner, K., Cibula, D., Denys, H., Rosengarten, O., Rodrigues, M., De Gregorio, N., et al. (2023). Atezolizumab combined with bevacizumab and platinum-based therapy for platinum-sensitive ovarian cancer: placebo-controlled ran-domized Phase III ATALANTE/ENGOT-ov29 trial. J. Clin. Oncol. 41, 4768–4778. https://doi.org/10.1200/JCO.23.00529.

19. Moore, K.N., Bookman, M., Sehouli, J., Miller, A., Anderson, C., Scam-bia, G., Myers, T., Taskiran, C., Robison, K., Mäenpää, J., et al. (2021). Atezolizumab, bevacizumab, and chemotherapy for newly diagnosed stage III or IV ovarian cancer: placebo-controlled randomized phase III trial (IMagyn050/GOG 3015/ENGOT-OV39). J. Clin. Oncol. 39, 1842–1855. https://doi.org/10.1200/JCO.21.00306.

20. Zamarin, D., Burger, R.A., Sill, M.W., Powell, D.J., Lankes, H.A., Feld-man, M.D., Zivanovic, O., Gunderson, C., Ko, E., Mathews, C., et al. (2020). Randomized phase II trial of nivolumab versus nivolumab and ipi-limumab for recurrent or persistent ovarian cancer: an NRG oncology study. J. Clin. Oncol. 38, 1814–1823. https://doi.org/10.1200/JCO.19.02059.

21. Zhou, D., Liu, J., Liu, R., Li, H., Huang, Y., Ma, D., Hong, L., and Gao, Q. (2022). Effectiveness and safety of niraparib as neoadjuvant therapy in advanced ovarian cancer with homologous recombination deficiency (NANT): study protocol for a prospective, multicenter, exploratory, Phase 2, single-arm study. Front. Oncol. 12, 852772. https://doi.org/10.3389/fonc.2022.852772.

22. Rustin, G.J.S., Vergote, I., Eisenhauer, E., Pujade-Lauraine, E., Quinn, M., Thigpen, T., Du Bois, A., Kristensen, G., Jakobsen, A., Sagae, S., et al. (2011). Definitions for response and progression in ovarian cancer clinical trials incorporating recist 1.1 and CA 125 agreed by the gyneco-logical cancer intergroup (GCIG). Int. J. Gynecol. Cancer 21, 419–423. https://doi.org/10.1097/IGC.0b013e3182070f17.

23. Coleman, R.L., Brady, M.F., Herzog, T.J., Sabbatini, P., Armstrong, D.K., Walker, J.L., Kim, B.G., Fujiwara, K., Tewari, K.S., O'Malley, D.M., et al. (2017). Bevacizumab and paclitaxel–carboplatin chemotherapy and sec-ondary cytoreduction in recurrent, platinum-sensitive ovarian cancer (NRG Oncology/Gynecologic Oncology Group study GOG-0213): a mul-ticentre, open-label, randomised, phase 3 trial. Lancet Oncol. 18, 779–791. https://doi.org/10.1016/S1470-2045(17)30279-6.

24. Binnewies, M., Roberts, E.W., Kersten, K., Chan, V., Fearon, D.F., Merad, M., Coussens, L.M., Gabrilovich, D.I., Ostrand-Rosenberg, S., Hedrick, C.C., et al. (2018). Understanding the tumor immune microenvironment (TIME) for effective therapy. Nat. Med. 24, 541–550. https://doi.org/10.1038/s41591-018-0014-x.

25. de Visser, K.E., and Joyce, J.A. (2023). The evolving tumor microenviron-ment: from cancer initiation to metastatic outgrowth. Cancer Cell 41, 374–403. https://doi.org/10.1016/j.ccell.2023.02.016.

26. Jiménez-Sánchez, A., Memon, D., Pourpe, S., Veeraraghavan, H., Li, Y., Vargas, H.A., Gill, M.B., Park, K.J., Zivanovic, O., Konner, J., et al. (2017). Heterogeneous tumor-immune microenvironments among differentially growing metastases in an ovarian cancer patient. Cell 170, 927–938.e20. https://doi.org/10.1016/j.cell.2017.07.025.

27. Jiménez-Sánchez, A., Cybulska, P., Mager, K.L.V., Koplev, S., Cast, O., Couturier, D.L., Memon, D., Selenica, P., Nikolovski, I., Mazaheri, Y., et al. (2020). Unraveling tumor–immune heterogeneity in advanced ovarian cancer uncovers immunogenic effect of chemotherapy. Nat. Genet. 52, 582–593. https://doi.org/10.1038/s41588-020-0630-5.

28. Shan, F., Somasundaram, A., Bruno, T.C., Workman, C.J., and Vignali, D.A.A. (2022). Therapeutic targeting of regulatory T cells in cancer. Trends Cancer 8, 944–961. https://doi.org/10.1016/j.trecan.2022.06.008.

29. Bruni, D., Angell, H.K., and Galon, J. (2020). The immune contexture and Immunoscore in cancer prognosis and therapeutic efficacy. Nat. Rev. Cancer 20, 662–680. https://doi.org/10.1038/s41568-020-0285-7.

30. Zhang, K., Erkan, E.P., Jamalzadeh, S., Dai, J., Andersson, N., Kaipio, K., Lamminen, T., Mansuri, N., Huhtinen, K., Carpén, O., et al. (2022). Longi-tudinal single-cell RNA-seq analysis reveals stress-promoted chemore-sistance in metastatic ovarian cancer. Sci. Adv. 8, eabm1831. https://doi.org/10.1126/sciadv.abm1831.

CellPress
OPEN ACCESS

Cell
Article

31. Budczies, J., Kluck, K., Beck, S., Ourailidis, I., Allgäuer, M., Menzel, M., Kazdal, D., Perkhofer, L., Kleger, A., Schirmacher, P., et al. (2022). Homologous recombination deficiency is inversely correlated with microsatellite instability and identifies immunologically cold tumors in most cancer types. J. Pathol. Clin. Res. 8, 371–382. https://doi.org/10.1002/cjp2.271.

32. Fares, C.M., Fenerty, K.E., Chander, C., Theisen, M.K., and Konecny, G.E. (2022). Homologous recombination deficiency and molecular subtype are associated with immunogenicity in ovarian cancer. Biomark. Med. 16, 771–782. https://doi.org/10.2217/bmm-2022-0044.

33. Kniemeyer, O., Brakhage, A.A., Ferreira, F., Wallner, M., and Sawitzki, B. (2016). Regulatory T cell Specificity Directs Tolerance versus Allergy against aeroantigens in Humans. Cell 167, 1067–1078.e16. https://doi.org/10.1016/j.cell.2016.09.050.

34. Bacher, P., and Scheffold, A. (2018). Antigen-specific regulatory T-cell responses against aeroantigens and their role in allergy. Mucosal Immunol. 11, 1537–1550. https://doi.org/10.1038/s41385-018-0038-z.

35. Liu, B., Zhang, Y., Wang, D., Hu, X., and Zhang, Z. (2022). Single-cell meta-analyses reveal responses of tumor-reactive CXCL13 + T cells to immune-checkpoint blockade. Nat. Cancer 3, 1123–1136. https://doi.org/10.1038/s43018-022-00433-7.

36. Lowery, F.J., Krishna, S., Yossef, R., Parikh, N.B., Chatani, P.D., Zacharakis, N., Parkhurst, M.R., Levin, N., Sindiri, S., Sachs, A., et al. (2022). Molecular signatures of antitumor neoantigen-reactive T cells from metastatic human cancers. Science 375, 877–884. https://doi.org/10.1126/science.abl5447.

37. Yoshitomi, H., and Ueno, H. (2021). Shared and distinct roles of T peripheral helper and T follicular helper cells in human diseases. Cell. Mol. Immunol. 18, 523–527. https://doi.org/10.1038/s41423-020-00529-z.

38. Cui, C., Wang, J., Fagerberg, E., Chen, P.M., Connolly, K.A., Damo, M., Cheung, J.F., Mao, T., Askari, A.S., Chen, S., et al. (2021). Neoantigen-driven B cell and CD4 T follicular helper cell collaboration promotes anti-tumor CD8 T cell responses. Cell 184, 6101–6118.e13. https://doi.org/10.1016/j.cell.2021.11.007.

39. Song, L., Cohen, D., Ouyang, Z., Cao, Y., Hu, X., and Liu, X.S. (2021). TRUST4: immune repertoire reconstruction from bulk and single-cell RNA-seq data. Nat. Methods 18, 627–630. https://doi.org/10.1038/s41592-021-01142-2.

40. Shan, F., Cillo, A.R., Cardello, C., Yuan, D.Y., Kunning, S.R., Cui, J., Lampenfeld, C., Williams, A.M., McDonough, A.P., Pennathur, A., et al. (2023). Integrated BATF transcriptional network regulates suppressive intratumoral regulatory T cells. Sci. Immunol. 8, eadf6717. https://doi.org/10.1126/sciimmunol.adf6717.

41. Dykema, A.G., Zhang, J., Cheung, L.S., Connor, S., Zhang, B., Zeng, Z., Cherry, C.M., Li, T., Caushi, J.X., Nishimoto, M., et al. (2023). Lung tumor–infiltrating Treg have divergent transcriptional profiles and function linked to checkpoint blockade response. Sci. Immunol. 8, eadg1487. https://doi.org/10.1126/sciimmunol.adg1487.

42. Xydia, M., Rahbari, R., Ruggiero, E., Macaulay, I., Tarabichi, M., Lohmayer, R., Wilkening, S., Michels, T., Brown, D., Vanuytven, S., et al. (2021). Common clonal origin of conventional T cells and induced regulatory T cells in breast cancer patients. Nat. Commun. 12, 1119. https://doi.org/10.1038/s41467-021-21297-y.

43. Daniel, B., Yost, K.E., Hsiung, S., Sandor, K., Xia, Y., Qi, Y., Hiam-Galvez, K.J., Black, M., J Raposo, C., Shi, Q., et al. (2022). Divergent clonal differentiation trajectories of T cell exhaustion. Nat. Immunol. 23, 1614–1627. https://doi.org/10.1038/s41590-022-01337-5.

44. Tsui, C., Kretschmer, L., Rapelius, S., Gabriel, S.S., Chisanga, D., Knöpper, K., Utzschneider, D.T., Nüssing, S., Liao, Y., Mason, T., et al. (2022). MYB orchestrates T cell exhaustion and response to checkpoint inhibition. Nature 609, 354–360. https://doi.org/10.1038/s41586-022-05105-1.

45. Giles, J.R., Ngiow, S.F., Manne, S., Baxter, A.E., Khan, O., Wang, P., Staupe, R., Abdel-Hakeem, M.S., Huang, H., Mathew, D., et al. (2022).

46. Aibar, S., González-Blas, C.B., Moerman, T., Huynh-Thu, V.A., Imrichova, H., Hulselmans, G., Rambow, F., Marine, J.C., Geurts, P., Aerts, J., et al. (2017). SCENIC: single-cell regulatory network inference and clustering. Nat. Methods 14, 1083–1086. https://doi.org/10.1038/nmeth.4463.

47. Dann, E., Henderson, N.C., Teichmann, S.A., Morgan, M.D., and Marioni, J.C. (2022). Differential abundance testing on single-cell data using k-nearest neighbor graphs. Nat. Biotechnol. 40, 245–253. https://doi.org/10.1038/s41587-021-01033-z.

48. Ahmadzadeh, M., Pasetto, A., Jia, L., Deniger, D.C., Stevanović, S., Robbins, P.F., and Rosenberg, S.A. (2019). Tumor-infiltrating human CD4+ regulatory T cells display a distinct TCR repertoire and exhibit tumor and neoantigen reactivity. Sci. Immunol. 4, eaao4310. https://doi.org/10.1126/sciimmunol.aao4310.

49. Marusyk, A., Janiszewska, M., and Polyak, K. (2020). Intratumor heterogeneity: the Rosetta Stone of therapy resistance. Cancer Cell 37, 471–484. https://doi.org/10.1016/j.ccell.2020.03.007.

50. Steimle, V., Siegrist, C.A., Mottet, A., Lisowska-Grospierre, B., and Mach, B. (1994). Regulation of MHC class II expression by interferon-γ mediated by the transactivator gene CIITA. Science 265, 106–109. https://doi.org/10.1126/science.8016643.

51. Kobayashi, K.S., and Van Den Elsen, P.J. (2012). NLRC5: A key regulator of MHC class I-dependent immune responses. Nat. Rev. Immunol. 12, 813–820. https://doi.org/10.1038/nri3339.

52. Wosen, J.E., Mukhopadhyay, D., MacAubas, C., and Mellins, E.D. (2018). Epithelial MHC class II expression and its role in antigen presentation in the gastrointestinal and respiratory tracts. Front. Immunol. 9, 2144. https://doi.org/10.3389/fimmu.2018.02144.

53. Heuberger, C., Pott, J., and Maloy, K.J. (2021). Why do intestinal epithelial cells express MHC class II? Immunology 162, 357–367. https://doi.org/10.1111/imm.13270.

54. Oliveira, G., Stromhaug, K., Cieri, N., Iorgulescu, J.B., Klaeger, S., Wolff, J.O., Rachimi, S., Chea, V., Krause, K., Freeman, S.S., et al. (2022). Landscape of helper and regulatory antitumour CD4+ T cells in melanoma. Nature 605, 532–538. https://doi.org/10.1038/s41586-022-04682-5.

55. Huang, H., Wang, Z., Zhang, Y., Pradhan, R.N., Ganguly, D., Chandra, R., Murimwa, G., Wright, S., Gu, X., Maddipati, R., et al. (2022). Mesothelial cell-derived antigen-presenting cancer-associated fibroblasts induce expansion of regulatory T cells in pancreatic cancer. Cancer Cell 40, 656–673.e7. https://doi.org/10.1016/j.ccell.2022.04.011.

56. Kwon, J.K., and Bakhoum, S.F. (2020). The cytosolic DNA-sensing cGAS–sting pathway in cancer. Cancer Discov. 10, 26–39. https://doi.org/10.1158/2159-8290.CD-19-0761.

57. Hopfner, K.P., and Hornung, V. (2020). Molecular mechanisms and cellular functions of cGAS–STING signalling. Nat. Rev. Mol. Cell Biol. 21, 501–521. https://doi.org/10.1038/s41580-020-0244-x.

58. Chen, L., and Flies, D.B. (2013). Molecular mechanisms of T cell co-stimulation and co-inhibition. Nat. Rev. Immunol. 13, 227–242. https://doi.org/10.1038/nri3405.

59. Edner, N.M., Carlesso, G., Rush, J.S., and Walker, L.S.K. (2020). Targeting co-stimulatory molecules in autoimmune disease. Nat. Rev. Drug Discov. 19, 860–883. https://doi.org/10.1038/s41573-020-0081-9.

60. Schnell, A., Bod, L., Madi, A., and Kuchroo, V.K. (2020). The yin and yang of co-inhibitory receptors: toward anti-tumor immunity without autoimmunity. Cell Res. 30, 285–299. https://doi.org/10.1038/s41422-020-0277-x.

61. Shimizu, K., Sugiura, D., Okazaki, I.M., Maruhashi, T., Takegami, Y., Cheng, C., Ozaki, S., and Okazaki, T. (2020). PD-1 imposes qualitative

Shared and distinct biological circuits in effector, memory and exhausted CD8+ T cells revealed by temporal single-cell transcriptomics and epigenetics. Nat. Immunol. 23, 1600–1613. https://doi.org/10.1038/s41590-022-01338-4.

control of cellular transcriptomes in response to T cell activation. Mol. Cell 77, 937–950.e6. https://doi.org/10.1016/j.molcel.2019.12.012.

62. Hui, E., Cheung, J., Zhu, J., Su, X., Taylor, M.J., Wallweber, H.A., Sasmal, D.K., Huang, J., Kim, J.M., Mellman, I., et al. (2017). T cell costimulatory receptor CD28 is a primary target for PD-1-mediated inhibition. Science 355, 1428–1433. https://doi.org/10.1126/science.aaf1292.

63. Oomizu, S., Arikawa, T., Niki, T., Kadowaki, T., Ueno, M., Nishi, N., Yamauchi, A., Hattori, T., Masaki, T., and Hirashima, M. (2012). Cell surface galectin-9 expressing Th Cells regulate Th17 and Foxp3+ Treg development by galectin-9 secretion. PLoS One 7, e48574. https://doi.org/10.1371/journal.pone.0048574.

64. Wu, C., Thalhamer, T., Franca, R.F., Xiao, S., Wang, C., Hotta, C., Zhu, C., Hirashima, M., Anderson, A.C., and Kuchroo, V.K. (2014). Galectin-9-CD44 interaction enhances stability and function of adaptive regulatory T cells. Immunity 41, 270–282. https://doi.org/10.1016/j.immuni.2014.06.011.

65. Sharma, M.D., Hou, D.Y., Baban, B., Koni, P.A., He, Y., Chandler, P.R., Blazar, B.R., Mellor, A.L., and Munn, D.H. (2010). Reprogrammed Foxp3+ regulatory T cells provide essential help to support cross-presentation and CD8+ T cell priming in naive mice. Immunity 33, 942–954. https://doi.org/10.1016/j.immuni.2010.11.022.

66. Baban, B., Chandler, P.R., Sharma, M.D., Pihkala, J., Koni, P.A., Munn, D.H., and Mellor, A.L. (2009). IDO activates regulatory T cells and blocks their conversion into Th17-like T cells. J. Immunol. 183, 2475–2483. https://doi.org/10.4049/jimmunol.0900986.

67. Lee, H.J., Kim, S.N., Jeon, M.S., Yi, T., and Song, S.U. (2017). ICOSL expression in human bone marrow-derived mesenchymal stem cells promotes induction of regulatory T cells. Sci. Rep. 7, 44486. https://doi.org/10.1038/srep44486.

68. Iwata, R., Hyoung Lee, J., Hayashi, M., Dianzani, U., Ofune, K., Maruyama, M., Oe, S., Ito, T., Hashiba, T., Yoshimura, K., et al. (2020). ICOSLG-mediated regulatory T-cell expansion and IL-10 production promote progression of glioblastoma. Neuro. Oncol 22, 333–344. https://doi.org/10.1093/neuonc/noz204.

69. Park, J., Kim, J.C., Lee, M., Lee, J.H., Kim, Y.N., Lee, Y.J., Kim, S., Kim, S.W., Park, S.H., and Lee, J.Y. (2023). Frequency of peripheral PD-1+regulatory T cells is associated with treatment responses to PARP inhibitor maintenance in patients with epithelial ovarian cancer. Br. J. Cancer 129, 1841–1851. https://doi.org/10.1038/s41416-023-02455-z.

70. Glasner, A., Rose, S.A., Sharma, R., Gudjonson, H., Chu, T., Green, J.A., Rampersaud, S., Valdez, I.K., Andretta, E.S., Dhillon, B.S., et al. (2023). Conserved transcriptional connectivity of regulatory T cells in the tumor microenvironment informs new combination cancer therapy strategies. Nat. Immunol. 24, 1020–1035. https://doi.org/10.1038/s41590-023-01504-2.

71. Tay, C., Tanaka, A., and Sakaguchi, S. (2023). Tumor-infiltrating regulatory T cells as targets of cancer immunotherapy. Cancer Cell 41, 450–465. https://doi.org/10.1016/j.ccell.2023.02.014.

72. Plitas, G., Konopacki, C., Wu, K., Bos, P.D., Morrow, M., Putintseva, E.V., Chudakov, D.M., and Rudensky, A.Y. (2016). Regulatory T cells exhibit distinct features in human breast cancer. Immunity 45, 1122–1134. https://doi.org/10.1016/j.immuni.2016.10.032.

73. Rickard, B.P., Conrad, C., Sorrin, A.J., Ruhi, M.K., Reader, J.C., Huang, S.A., Franco, W., Scarcelli, G., Polacheck, W.J., Roque, D.M., et al. (2021). Malignant ascites in ovarian cancer: cellular, acellular, and biophysical determinants of molecular characteristics and therapy response. Cancers (Basel) 13, 4318. https://doi.org/10.3390/cancers13174318.

74. Ford, C.E., Werner, B., Hacker, N.F., and Warton, K. (2020). The untapped potential of ascites in ovarian cancer research and treatment. Br. J. Cancer 123, 9–16. https://doi.org/10.1038/s41416-020-0875-x.

75. Topalian, S.L., Forde, P.M., Emens, L.A., Yarchoan, M., Smith, K.N., and Pardoll, D.M. (2023). Neoadjuvant immune checkpoint blockade: A window of opportunity to advance cancer immunotherapy. Cancer Cell 41, 1551–1566. https://doi.org/10.1016/j.ccell.2023.07.011.

76. Nasta, F., Laudisi, F., Sambucci, M., Rosado, M.M., and Pioli, C. (2010). Increased Foxp3+ regulatory T cells in poly(ADP-ribose) Polymerase-1 deficiency. J. Immunol. 184, 3470–3477. https://doi.org/10.4049/jimmunol.0901568.

77. Zhang, P., Maruyama, T., Konkel, J.E., Abbatiello, B., and Zamarron, B. (2013). PARP-1 controls immunosuppressive function of regulatory T cells by destabilizing Foxp3. PLoS One 8, e71590. https://doi.org/10.1371/journal.pone.0071590.

78. Gu, W., Ge, R., Zhu, F., Li, D., Liang, R., Ge, J., Wang, Y., Li, B., and Qiu, J. (2020). PARP-1 inhibitor-AG14361 suppresses acute allograft rejection via stabilizing CD4+FoxP3+ regulatory T cells. Pathol. Res. Pract. 216, 153021. https://doi.org/10.1016/j.prp.2020.153021.

79. Luo, X., Nie, J., Wang, S., Chen, Z., Chen, W., Li, D., Hu, H., and Li, B. (2015). Poly(ADP-ribosyl)ation of FOXP3 Protein Mediated by PARP-1 Protein regulates the function of regulatory T cells. J. Biol. Chem. 290, 28675–28682. https://doi.org/10.1074/jbc.M115.661611.

80. Pai, C.S., Huang, J.T., Lu, X., Simons, D.M., Park, C., Chang, A., Tamaki, W., Liu, E., Roybal, K.T., Seagal, J., et al. (2019). Clonal deletion of tumor-specific T cells by interferon-γ confers therapeutic resistance to combination immune checkpoint blockade. Immunity 50, 477–492.e8. https://doi.org/10.1016/j.immuni.2019.01.006.

81. Dubrot, J., Du, P.P., Lane-Reticker, S.K., Kessler, E.A., Muscato, A.J., Mehta, A., Freeman, S.S., Allen, P.M., Olander, K.E., Ockerman, K.M., et al. (2022). In vivo CRISPR screens reveal the landscape of immune evasion pathways across cancer. Nat. Immunol. 23, 1495–1506. https://doi.org/10.1038/s41590-022-01315-x.

82. Li, G., Choi, J.E., Kryczek, I., Sun, Y., Liao, P., Li, S., Wei, S., Grove, S., Vatan, L., Nelson, R., et al. (2023). Intersection of immune and oncometabolic pathways drives cancer hyperprogression during immunotherapy. Cancer Cell 41, 304–322.e7. https://doi.org/10.1016/j.ccell.2022.12.008.

83. Benci, J.L., Johnson, L.R., Choa, R., Xu, Y., Qiu, J., Zhou, Z., Xu, B., Ye, D., Nathanson, K.L., June, C.H., et al. (2019). Opposing functions of interferon coordinate adaptive and innate immune responses to cancer immune checkpoint blockade. Cell 178, 933–948.e14. https://doi.org/10.1016/j.cell.2019.07.019.

84. Song, E., and Chow, R.D. (2023). Mutations in IFN-γ signaling genes sensitize tumors to immune checkpoint blockade. Cancer Cell 41, 651–652. https://doi.org/10.1016/j.ccell.2023.02.013.

85. National Cancer Institute - SEER Program (2022). Cancer Stat Facts: Ovarian Cancer (National Cancer Institute). https://seer.cancer.gov/statfacts/html/ovary.html.

86. Nadler, D.L., and Zurbenko, I.G. (2014). Estimating cancer latency times using a Weibull model. Adv. Epidemiol. 2014, 1–8. https://doi.org/10.1155/2014/746769.

87. Hao, Y., Hao, S., Andersen-Nissen, E., Mauck, W.M., Zheng, S., Butler, A., Lee, M.J., Wilk, A.J., Darby, C., Zager, M., et al. (2021). Integrated analysis of multimodal single-cell data. Cell 184, 3573–3587.e29. https://doi.org/10.1016/j.cell.2021.04.048.

88. Andreatta, M., Corria-Osorio, J., Müller, S., Cubas, R., Coukos, G., and Carmona, S.J. (2021). Interpretation of T cell states from single-cell transcriptomics data using reference atlases. Nat. Commun. 12, 2965. https://doi.org/10.1038/s41467-021-23324-4.

89. Nieto, P., Elosua-Bayes, M., Trincado, J.L., Marchese, D., Massoni-Badosa, R., Salvany, M., Henriques, A., Nieto, J., Aguilar-Fernández, S., Mereu, E., et al. (2021). A single-cell tumor immune atlas for precision oncology. Genome Res. 31, 1913–1926. https://doi.org/10.1101/gr.273300.120.

90. Zheng, L., Qin, S., Si, W., Wang, A., Xing, B., Gao, R., Ren, X., Wang, L., Wu, X., Zhang, J., et al. (2021). Pan-cancer single-cell landscape of tumor-infiltrating T cells. Science 374, abe6474. https://doi.org/10.1126/science.abe6474.

91. Qian, J., Olbrecht, S., Boeckx, B., Vos, H., Laoui, D., Etlioglu, E., Wauters, E., Pomella, V., Verbandt, S., Busschaert, P., et al. (2020). A pan-cancer blueprint of the heterogeneous tumor microenvironment revealed by single-cell profiling. Cell Res. 30, 745–762. https://doi.org/10.1038/s41422-020-0355-0.

92. Han, X., Zhou, Z., Fei, L., Sun, H., Wang, R., Chen, Y., Chen, H., Wang, J., Tang, H., Ge, W., et al. (2020). Construction of a human cell landscape at single-cell level. Nature 581, 303–309. https://doi.org/10.1038/s41586-020-2157-4.

93. Dinh, H.Q., Lin, X., Abbasi, F., Nameki, R., Haro, M., Olingy, C.E., Chang, H., Hernandez, L., Gayther, S.A., Wright, K.N., et al. (2021). Single-cell transcriptomics identifies gene expression networks driving differentiation and tumorigenesis in the human fallopian tube. Cell Rep. 35, 108978. https://doi.org/10.1016/j.celrep.2021.108978.

94. Fan, X., Bialecka, M., Moustakas, I., Lam, E., Torrens-Juaneda, V., Borggreven, N.V., Trouw, L., Louwe, L.A., Pilgram, G.S.K., Mei, H., et al. (2019). Single-cell reconstruction of follicular remodeling in the human adult ovary. Nat. Commun. 10, 3164. https://doi.org/10.1038/s41467-019-11036-9.

95. Buechler, M.B., Pradhan, R.N., Krishnamurty, A.T., Cox, C., Calviello, A.K., Wang, A.W., Yang, Y.A., Tam, L., Caothien, R., Roose-Girma, M., et al. (2021). Cross-tissue organization of the fibroblast lineage. Nature 593, 575–579. https://doi.org/10.1038/s41586-021-03549-5.

96. Mulder, K., Patel, A.A., Kong, W.T., Piot, C., Halitzki, E., Dunsmore, G., Khalilnezhad, S., Irac, S.E., Dubuisson, A., Chevrier, M., et al. (2021). Cross-tissue single-cell landscape of human monocytes and macrophages in health and disease. Immunity 54, 1883–1900.e5. https://doi.org/10.1016/j.immuni.2021.07.007.

97. Cheng, S., Li, Z., Gao, R., Xing, B., Gao, Y., Yang, Y., Qin, S., Zhang, L., Ouyang, H., Du, P., et al. (2021). A pan-cancer single-cell transcriptional atlas of tumor infiltrating myeloid cells. Cell 184, 792–809.e23. https://doi.org/10.1016/j.cell.2021.01.010.

98. Jin, S., Guerrero-Juarez, C.F., Zhang, L., Chang, I., Ramos, R., Kuan, C.H., Myung, P., Plikus, M.V., and Nie, Q. (2021). Inference and analysis of cell-cell communication using CellChat. Nat. Commun. 12, 1088. https://doi.org/10.1038/s41467-021-21246-9.

99. Kotliar, D., Veres, A., Nagy, M.A., Tabrizi, S., Hodis, E., Melton, D.A., and Sabeti, P.C. (2019). Identifying gene expression programs of cell-type identity and cellular activity with single-cell RNA-Seq. eLife 8, 310599. https://doi.org/10.7554/eLife.43803.

100. Badia-I-Mompel, P., Vélez Santiago, J., Braunger, J., Geiss, C., Dimitrov, D., Müller-Dott, S., Taus, P., Dugourd, A., Holland, C.H., Ramirez Flores, R.O., et al. (2022). decoupleR: ensemble of computational methods to infer biological activities from omics data. Bioinform. Adv. 2, vbac016. https://doi.org/10.1093/bioadv/vbac016.

101. Bannon, D., Moen, E., Schwartz, M., Borba, E., Kudo, T., Greenwald, N., Vijayakumar, V., Chang, B., Pao, E., Osterman, E., et al. (2021). DeepCell Kiosk: scaling deep learning–enabled cellular image analysis with Kubernetes. Nat. Methods 18, 43–45. https://doi.org/10.1038/s41592-020-01023-0.

102. Love, M.I., Huber, W., and Anders, S. (2014). Moderated estimation of fold change and dispersion for RNA-seq data with DESeq2. Genome Biol. 15, 550. https://doi.org/10.1186/s13059-014-0550-8.

103. Wickham, H., François, R., Henry, L., Müller, K., and Vaughan, D. (2023). dplyr: A Grammar of Data Manipulation. R package version 1.1.4. https://github.com/tidyverse/dplyr.

104. Lun, A.T.L., Riesenfeld, S., Andrews, T., Dao, T.P., Gomes, T., and Marioni, J.C. (2019). EmptyDrops: distinguishing cells from empty droplets in droplet-based single-cell RNA sequencing data. Genome Biol. 20, 1–9. https://doi.org/10.1186/s13059-019-1662-y.

105. Wickham, H. (2016). ggplot2: Elegant Graphics for Data Analysis (Springer-Verlag New York).

106. Kassambara, A. (2023). ggpubr: "ggplot2" Based Publication Ready Plots. https://CRAN.R-project.org/package=ggpubr.

107. Xiao, N. (2024). ggsci: Scientific Journal and Sci-Fi Themed Color Palettes for "ggplot2". https://cran.r-project.org/web/packages/ggsci/ggsci.pdf.

108. van der Auwera, G., and O'Connor, B.D. (2020). Genomics in the Cloud: Using Docker, GATK, and WDL in Terra (O'Reilly Media).

109. Korsunsky, I., Millard, N., Fan, J., Slowikowski, K., Zhang, F., Wei, K., Baglaenko, Y., Brenner, M., Loh, P.R., and Raychaudhuri, S. (2019). Fast, sensitive and accurate integration of single-cell data with Harmony. Nat. Methods 16, 1289–1296. https://doi.org/10.1038/s41592-019-0619-0.

110. Patel, A.P., Tirosh, I., Trombetta, J.J., Shalek, A.K., Gillespie, S.M., Wakimoto, H., Cahill, D.P., Nahed, B.V., Curry, W.T., Martuza, R.L., et al. (2014). Single-cell RNA-seq highlights intratumoral heterogeneity in primary glioblastoma. Science 344, 1396–1401. https://doi.org/10.1126/science.1254257.

111. Kluyver, T., Ragan-Kelley, B., Pérez, F., Granger, B., Bussonnier, M., Frederic, J., Kelley, K., Hamrick, J., Grout, J., Corlay, S., et al. (2016). Jupyter Notebooks – a publishing format for reproducible computational workflows. In Positioning and Power in Academic Publishing: Players, Agents and Agendas, F. Loizides and B. Schmidt, eds. (IOS Press), pp. 87–90.

112. Melsted, P., Booeshaghi, A.S., Liu, L., Gao, F., Lu, L., Min, K.H.J., da Veiga Beltrame, E., Hjörleifsson, K.E., Gehring, J., and Pachter, L. (2021). Modular, efficient and constant-memory single-cell RNA-seq preprocessing. Nat. Biotechnol. 39, 813–818. https://doi.org/10.1038/s41587-021-00870-2.

113. Mayakonda, A., Lin, D.C., Assenov, Y., Plass, C., and Koeffler, H.P. (2018). Maftools: efficient and comprehensive analysis of somatic variants in cancer. Genome Res. 28, 1747–1756. https://doi.org/10.1101/gr.239244.118.

114. Hunter, J.D. (2007). Matplotlib: A 2D graphics environment. Comput. Sci. Eng. 9, 90–95. https://doi.org/10.1109/MCSE.2007.55.

115. Bolotin, D.A., Poslavsky, S., Mitrophanov, I., Shugay, M., Mamedov, I.Z., Putintseva, E.V., and Chudakov, D.M. (2015). MiXCR: software for comprehensive adaptive immunity profiling. Nat. Methods 12, 380–381. https://doi.org/10.1038/nmeth.3364.

116. Harris, C.R., Millman, K.J., van der Walt, S.J., Gommers, R., Virtanen, P., Cournapeau, D., Wieser, E., Taylor, J., Berg, S., Smith, N.J., et al. (2020). Array programming with NumPy. Nature 585, 357–362. https://doi.org/10.1038/s41586-020-2649-2.

117. The Pandas Develompent Team (2020). Pandas-dev/pandas: pandas. Zenodo 21, 1–9.

118. Johnson, K.S. (2022). phenoptr: inForm Helper Functions. R package version 0.3.2. https://akoyabio.github.io/phenoptr/.

119. Bankhead, P., Loughrey, M.B., Fernández, J.A., Dombrowski, Y., McArt, D.G., Dunne, P.D., McQuaid, S., Gray, R.T., Murray, L.J., Coleman, H.G., et al. (2017). QuPath: open source software for digital pathology image analysis. Sci. Rep. 7, 16878. https://doi.org/10.1038/s41598-017-17204-5.

120. Wolf, F.A., Angerer, P., and Theis, F.J. (2018). SCANPY: large-scale single-cell gene expression data analysis. Genome Biol. 19, 15. https://doi.org/10.1186/s13059-017-1382-0.

121. Virtanen, P., Gommers, R., Oliphant, T.E., Haberland, M., Reddy, T., Cournapeau, D., Burovski, E., Peterson, P., Weckesser, W., Bright, J., et al. (2020). SciPy 1.0: fundamental algorithms for scientific computing in python. Nat. Methods 17, 261–272.

122. Sturm, G., Szabo, T., Fotakis, G., Haider, M., Rieder, D., Trajanoski, Z., and Finotello, F. (2020). Scirpy: A Scanpy extension for analyzing single-cell T-cell receptor-sequencing data. Bioinformatics 36, 4817–4818. https://doi.org/10.1093/bioinformatics/btaa611.

123. Wolock, S.L., Lopez, R., and Klein, A.M. (2019). Scrublet: computational identification of cell doublets in single-cell transcriptomic data. Cell Syst. *8*, 281–291.e9. https://doi.org/10.1016/j.cels.2018.11.005.

124. Bergen, V., Lange, M., Peidli, S., Wolf, F.A., and Theis, F.J. (2020). Generalizing RNA velocity to transient cell states through dynamical modeling. Nat. Biotechnol. *38*, 1408–1414. https://doi.org/10.1038/s41587-020-0591-3.

125. Waskom, M.L. (2021). seaborn: statistical data visualization. J. Open Source Softw. *6*, 3021. https://doi.org/10.21105/joss.03021.

126. Pedregosa, F., Varoquaux, G., Gramfort, A., Michel, V., Thirion, B., Grisel, O., Blondel, M., Prettenhofer, P., Weiss, R., Dubourg, V., et al. (2011). Scikit-learn: machine learning in python. J. Mach. Learn. Res. *12*, 2825–2830.

127. Kang, J.B., Nathan, A., Weinand, K., Zhang, F., Millard, N., Rumker, L., Moody, D.B., Korsunsky, I., and Raychaudhuri, S. (2021). Efficient and precise single-cell reference atlas mapping with Symphony. Nat. Commun. *12*, 5890. https://doi.org/10.1038/s41467-021-25957-x.

128. Ascensión, A.M., Ibáñez-Solé, O., Inza, I., Izeta, A., and Araúzo-Bravo, M.J. (2022). Triku: A feature selection method based on nearest neighbors for single-cell data. GigaScience *11*, 1–16. https://doi.org/10.1093/gigascience/giac017.

129. Andreatta, M., and Carmona, S.J. (2021). UCell: robust and scalable single-cell gene signature scoring. Comput. Struct. Biotechnol. J. *19*, 3796–3798. https://doi.org/10.1016/j.csbj.2021.06.043.

130. La Manno, G., Soldatov, R., Zeisel, A., Braun, E., Hochgerner, H., Petukhov, V., Lidschreiber, K., Kastriti, M.E., Lönnerberg, P., Furlan, A., et al. (2018). RNA velocity of single cells. Nature *560*, 494–498. https://doi.org/10.1038/s41586-018-0414-6.

131. Li, L., Gu, Y., Zhang, M., Shi, X., Li, Z., Xu, X., Sun, T., Dong, Y., Xue, C., Zhu, X., et al. (2023). HRD effects on first-line adjuvant chemotherapy and PARPi maintenance therapy in Chinese ovarian cancer patients. NPJ Precis. Oncol. *7*, 51. https://doi.org/10.1038/s41698-023-00402-y.

132. Zhang, W., Du, Y., Su, Z., Wang, C., Zeng, X., Zhang, R., Hong, X., Nie, C., Wu, J., Cao, H., et al. (2015). Imonitor: A robust pipeline for TCR and BCR repertoire analysis. Genetics *201*, 459–472. https://doi.org/10.1534/genetics.115.176735.

133. Walton, J., Blagih, J., Ennis, D., Leung, E., Dowson, S., Farquharson, M., Tookman, L.A., Orange, C., Athineos, D., Mason, S., et al. (2016). CRISPR/Cas9-mediated Trp53 and BRCA2 knockout to generate improved murine models of ovarian high-grade serous carcinoma. Cancer Res. *76*, 6118–6129. https://doi.org/10.1158/0008-5472.CAN-16-1272.

134. Richards, S., Aziz, N., Bale, S., Bick, D., Das, S., Gastier-Foster, J., Grody, W.W., Hegde, M., Lyon, E., Spector, E., et al. (2015). Standards and guidelines for the interpretation of sequence variants: A joint consensus recommendation of the American College of Medical Genetics and Genomics and the Association for Molecular Pathology. Genet. Med. *17*, 405–424. https://doi.org/10.1038/gim.2015.30.

135. Li, M.M., Datto, M., Duncavage, E.J., Kulkarni, S., Lindeman, N.I., Roy, S., Tsimberidou, A.M., Vnencak-Jones, C.L., Wolff, D.J., Younes, A., et al. (2017). Standards and guidelines for the interpretation and reporting of sequence variants in cancer: A joint consensus recommendation of the association for molecular pathology, American Society of Clinical Oncology, and College of American Pathologists. J. Mol. Diagn. *19*, 4–23. https://doi.org/10.1016/j.jmoldx.2016.10.002.

136. Li, H., van der Leun, A.M., Yofe, I., Lubling, Y., Gelbard-Solodkin, D., van Akkooi, A.C.J., van den Braber, M., Rozeman, E.A., Haanen, J.B.A.G., Blank, C.U., et al. (2019). Dysfunctional CD8 T cells form a proliferative, dynamically regulated compartment within human melanoma. Cell *176*, 775–789.e18. https://doi.org/10.1016/j.cell.2018.11.043.

137. Tirosh, I., Izar, B., Prakadan, S.M., Wadsworth, M.H., Treacy, D., Trombetta, J.J., Rotem, A., Rodman, C., Lian, C., Murphy, G., et al. (2016). Dissecting the multicellular ecosystem of metastatic melanoma by single-cell RNA-seq. Science *352*, 189–196. https://doi.org/10.1126/science.aad0501.

138. Lawrenson, K., Fonseca, M.A.S., Liu, A.Y., Segato Dezem, F., Lee, J.M., Lin, X., Corona, R.I., Abbasi, F., Vavra, K.C., Dinh, H.Q., et al. (2019). A study of high-grade serous ovarian cancer origins implicates the SOX18 transcription factor in tumor development. Cell Rep. *29*, 3726–3735.e4. https://doi.org/10.1016/j.celrep.2019.10.122.

139. Bell, D., Berchuck, A., Birrer, M., Chien, J., Cramer, D.W., Dao, F., Dhir, R., Disaia, P., Gabra, H., and Glenn, P. (2011). Integrated genomic analyses of ovarian carcinoma. Nature *474*, 609–615. https://doi.org/10.1038/nature10166.

140. Martin, M. (2011). Cutadapt removes adapter sequences from high-throughput sequencing reads. EMBnet J. *17*, 10. https://doi.org/10.14806/ej.17.1.200.

141. Dobin, A., Davis, C.A., Schlesinger, F., Drenkow, J., Zaleski, C., Jha, S., Batut, P., Chaisson, M., and Gingeras, T.R. (2013). STAR: ultrafast universal RNA-seq aligner. Bioinformatics *29*, 15–21. https://doi.org/10.1093/bioinformatics/bts635.

142. Liao, Y., Smyth, G.K., and Shi, W. (2014). FeatureCounts: an efficient general purpose program for assigning sequence reads to genomic features. Bioinformatics *30*, 923–930. https://doi.org/10.1093/bioinformatics/btt656.

143. Squair, J.W., Gautier, M., Kathe, C., Anderson, M.A., James, N.D., Hutson, T.H., Hudelle, R., Qaiser, T., Matson, K.J.E., Barraud, Q., et al. (2021). Confronting false discoveries in single-cell differential expression. Nat. Commun. *12*, 5692. https://doi.org/10.1038/s41467-021-25960-2.

144. Chan, J.M., Quintanal-Villalonga, Á., Gao, V.R., Xie, Y., Allaj, V., Chaudhary, O., Masilionis, I., Egger, J., Chow, A., Walle, T., et al. (2021). Signatures of plasticity, metastasis, and immunosuppression in an atlas of human small cell lung cancer. Cancer Cell *39*, 1479–1496.e18. https://doi.org/10.1016/j.ccell.2021.09.008.

STAR★METHODS

KEY RESOURCES TABLE

REAGENT OR RESOURCES	SOURCE	IDENTIFIER
Antibodies		
APC Hamster Anti-Mouse CD3e	BD Biosciences	Cat# 553066; RRID: AB_398529
PerCP-Cy™5.5 Hamster Anti-Mouse CD3e	BD Biosciences	Cat# 551163; RRID: AB_394082
FITC Rat Anti-Mouse CD4	BD Biosciences	Cat# 553729; RRID: AB_395013
BV605 Rat Anti-Mouse CD8a	BD Biosciences	Cat# 563152; RRID: AB_2738030
BV605 Mouse Anti-Human CD127	BD Biosciences	Cat# 562662; RRID: AB_2737706
BV510 Mouse Anti-Human CD25	BD Biosciences	Cat# 563351; RRID: AB_2744336
BV421 Mouse Anti-Human CCR8 (CD198)	BD Biosciences	Cat# 566379; RRID: AB_2744265
PE-Cy™7 Rat Anti-Mouse CD45	BD Biosciences	Cat# 552848; RRID: AB_394489
BV421 Rat Anti-Mouse Foxp3	BD Biosciences	Cat# 562996; RRID: AB_2737940
PE Mouse Anti-Mouse CD366 (TIM3)	BD Biosciences	Cat# 566346; RRID: AB_2739702
APC anti-human CD3	BioLegend	Cat# 300312; RRID: AB_314048
PerCP/Cyanine5.5 anti-human CD3	BioLegend	Cat# 317336; RRID: AB_2561628
PerCP/Cyanine5.5 anti-human CD4	BioLegend	Cat# 300529; RRID: AB_893328
Brilliant Violet 785™ anti-human CD4	BioLegend	Cat# 300554; RRID: AB_2564382
APC anti-human CD8a	BioLegend	Cat# 300912; RRID: AB_314116
FITC anti-human CD8a	BioLegend	Cat# 300905; RRID: AB_314109
FITC anti-human CD19	BioLegend	Cat# 302206; RRID: AB_314236
PE anti-human CD45	BioLegend	Cat# 368510; RRID: AB_2566370
PE anti-human HLA-DR	BioLegend	Cat# 307606; RRID: AB_314684
APC anti-mouse CD198 (CCR8)	BioLegend	Cat# 150310; RRID: AB_2629602
Brilliant Violet 785™ anti-mouse CD279 (PD-1)	BioLegend	Cat# 135225; RRID: AB_2563680
Brilliant Violet 510™ anti-mouse CD25	BioLegend	Cat# 102042; RRID: AB_2562270
Anti-mouse PD-1	Cell Signal Technology	Cat# 84651; RRID: AB_2800041
Anti-human PD-1	Cell Signal Technology	Cat# 86163; RRID: AB_2728833
Anti-human TNFRSF9	Cell Signal Technology	Cat# 19541
Anti-human CD4	Abcam	Cat# ab133616; RRID: AB_2750883
Anti-human CD8α	Abcam	Cat# ab237709; RRID: AB_2892677
Anti-human/mouse FOXP3	Abcam	Cat# ab215206; RRID: AB_2860568
Anti-human Pan-Cytokeratin	Abcam	Cat# ab7753; RRID: AB_306047
InVivoPlus anti-mouse CD25 (IL-2Rα)	Bioxcell	Cat# BP0012
In vivo anti-human CCR8	Zai Lab (Shanghai) Co., Ltd.	ZL-1218
Library preparation and sequencing reagents		
Tumor Dissociation Kit, human	Miltenyi Biotec	Cat# 130-095-929
Tumor Dissociation Kit, mouse	Miltenyi Biotec	Cat# 130-096-730
Red Blood Cell Lysis Solution (10x)	Miltenyi Biotec	Cat# 130-094-183
Dead Cell Removal Kit	Miltenyi Biotec	Cat# 130-090-101
Tissue Storage Solution	Miltenyi Biotec	Cat# 130-100-008
gentleMACSTM Octo Dissociator with Heaters	Miltenyi Biotec	Cat# 130-096-427
Chromium Next GEM Single Cell 3' Gel Bead Kit v.3.1	10x Genomics	Cat# 1000122
Chromium Next GEM Single Cell 3' GEM Kit v.3.1	10x Genomics	Cat# 1000123

(*Continued on next page*)

Continued

REAGENT OR RESOURCES	SOURCE	IDENTIFIER
Chromium Next GEM Single Cell 3' Library Kit v.3.1	10x Genomics	Cat# 1000157
Dynabeads Myone Silane	10x Genomics	Cat# 2000048
Dual Index Kit TT Set A	10x Genomics	Cat# 1000215
SPRIselect Reagent Kit	Beckman Coulter	Cat# B23318
Chromium Next GEM Chip G Single Cell Kit	10x Genomics	Cat# 1000120
Chromium Controller	10x Genomics	Cat# 120270
Acridine Orange (AO) / Propidium Iodide (PI) assay	DENOVix	Cat# CD-AO-PI-1.5
GEXSCOPE® Single Cell RNA Library Kit Tissue V2	Singleron	Cat# 5180012
sCircle™ Single Cell Full Length Immuno TCR Library Kit Cell	Singleron	Cat# 4153011
QIAamp DNA Mini Kit	QIAGEN	Cat# 51306
Multiplex PCR Kit	QIAGEN	Cat# 206145
Magnetic beads	Beckman Coulter	Cat# A63882
KAPA HiFi HotStart ReadyMix PCR Kit	KAPA BioSystems	Cat# KK2631
Agilent 2100 Bioanalyzer and the DNA HS kit	Agilent Technologies	N/A
Qubit fluorometer and the Qubit dsDNA HS (High Sensitivity) Assay Kit	Invitrogen	Cat# Q33231
Multiplex PCR Kit	QIAGEN	Cat# 206143
Reagents and Kit		
DNeasy Blood &Tissue Kit	QIAGEN	Cat# 69504
Precision Human HRD Assay	Precision Scientific	N/A
Zombie NIR™ Fixable Viability Kit	BioLegend	Cat# 423105
Ficoll	TBD Science	Cat# LTS1077
Human IFN-γ Recombinant Protein	PeproTech	Cat# 300-02
Human IFN-β Recombinant Protein	PeproTech	Cat# 300-02BC
Human IFN-α Protein	Acro biosystems	Cat# IFA-H52H9
X-tremeGENE HP DNA Transfection Reagent	Roche	Cat# 6366236001
Polybrene	YEASEN	Cat# 40804ES76
Puromycin	Selleck	Cat# S7417
Blunt Simple Cloning Kit	Transgen	Cat# CB111-01
FastPfu Fly PCR SuperMix(-dye)	Transgen	Cat# AS231
Fixation/Permeabilization Solution Kit	BD Biosciences	Cat# 554715
Opal 6-Plex Manual Detection Kit	Akoya Biosciences	Cat# NEL81100KT
Reverse Transcription Kit	Vazyme	Cat# R323-01
Platinum™ SuperFi II DNA Polymerase	Thermo Fisher Scientific	Cat# 12361010
Bortezomib	Selleck	Cat# S1013
Niraparib	Zai Lab (Shanghai) Co., Ltd.	N/A
DMEM	Thermo Fisher Scientific	Cat# 10566016
RPMI 1640 medium	Thermo Fisher Scientific	Cat# 61870036
MCDB 105 medium	Sigma-Aldrich	Cat# M6395-1L
199 medium	Thermo Fisher Scientific	Cat# 12340030
McCoy's 5A medium	Thermo Fisher Scientific	Cat# 12330031
FBS	Gibco	Cat# A5669801
Penicillin-streptomycin solution	Thermo Fisher Scientific	Cat# 10378016
DAPI	Thermo Fisher Scientific	Cat# 62247

Continued

REAGENT OR RESOURCES	SOURCE	IDENTIFIER
Lipofectamine™ 3000	Thermo Fisher Scientific	Cat# L3000001
TRI reagent	Sigma-Aldrich	Cat# T9424
SYBR Green	Bio-Rad Laboratories	Cat# 1725124
Experimental models: Cell lines		
BT-549	ATCC	Cat# HTB-122
MDA-MB-231	ATCC	Cat# CRM-HTB-26
OV90	ATCC	Cat# CRL-3585
SKOV3	ATCC	Cat# HTB-77
HEK293T	ATCC	Cat# CRL-3216
A2780	Sigma-Aldrich	Cat# 93112519
OVCAR8	MDACC's Characterized Cell Line Core	N/A
ID8	Sigma-Aldrich	Cat# SCC145
EO771	ATCC	Cat# CRL-3461
Experimental models: Organisms/strains		
C57BL/6N mice	Vital River	Strain Code 213
C57BL/6Smoc-$Ccr8^{em3(hCCR8)/Smoc}$	Shanghai Model Organisms Center, Inc.	Cat# NM-HU-2000054
C57BL/6-$Ccr8^{tm1(CCR8)Bcgen}$/Bcgen	Biocytogen	Cat# 110096
Oligonucleotides		
Si*BRCA1* #1: CCACACGATTTGACGGAAA	Ribobio	N/A
Si*BRCA1* #2: GCAGGAAATGGCTGAACTA	Ribobio	N/A
Si*BRCA2* #1: GAAGAACAATATCCTACTA	Ribobio	N/A
Si*BRCA2* #2: CATGGAATCTGCTGAACAA	Ribobio	N/A
Brca1 gRNA sequence #1: GACTCCTTCCCAGGACAACT	Tsingke	N/A
Brca1 gRNA sequence #2: TGTCTACATTGAACTAGGTA	Tsingke	N/A
Brca2 gRNA sequence #1: TGCTTTGGCATATTATACGG	Tsingke	N/A
Brca2 gRNA sequence #2: TAGGACCGATAAGCCTCAAT	Tsingke	N/A
Trp53 gRNA sequence #1: TGAGCGCTGCTCCGATGGTGA	Tsingke	N/A
Trp53 gRNA sequence #2: AGTGAAGCCCTCCGAGTGTC	Tsingke	N/A
BRCA1 forward primer: CTGAAGACTGCTCAGGGCTATC	Tsingke	N/A
BRCA1 reverse primer: AGGGTAGCTGTTAGAAGGCTGG	Tsingke	N/A
BRCA2 forward primer: GGCTTCAAAAAGCACTCCAGATG	Tsingke	N/A
BRCA2 reverse primer: GGATTCTGTATCTCTTGACGTTCC	Tsingke	N/A
GAPDH forward primer: GTCTCCTCTGACTTCAACAGCG	Tsingke	N/A
GAPDH reverse primer: ACCACCCTGTTGCTGTAGCCAA	Tsingke	N/A
Brca1 forward primer: CTGAGTCCAAAGGTGACAGCT	Tsingke	N/A
Brca1 reverse primer: GTGTTGGAAGCAGGGAAGATC	Tsingke	N/A
Brca2 forward primer: GCCTTGGTCGTGGTGTCTG	Tsingke	N/A

(Continued on next page)

Cell
Article

Continued

REAGENT OR RESOURCES	SOURCE	IDENTIFIER
Brca2 reverse primer: TGCCCAAAGTCCCAGTTCA	Tsingke	N/A
Trp53 forward primer: ATCCACAGCCATCACCTCACT	Tsingke	N/A
Trp53 reverse primer: GAACTTTTGTCCCTCCCACTTT	Tsingke	N/A
LentiCRISPRv2 plasmid	Addgene	Cat# 52961
psPAX2	Addgene	Cat# 12260
pMD2.G	Addgene	Cat# 12259
Blunt Simple Cloning Kit	TRANS	Cat# CB111-01
Deposited data		
Single-cell RNA-seq data from human PBMC	Hao et al.[87]	GSE164378
Single-cell RNA-seq data from mouse melanoma and colon adenocarcinoma	Andreatta et al.[88]	https://doi.org/10.6084/m9.figshare.1247857
Single-cell RNA-seq data from multiple human cancer types	Nieto et al.[89]	https://doi.org/10.5281/zenodo.4263972
Single-cell RNA-seq data from multiple human cancer types	Zheng et al.[90]	GSE156728
Single-cell RNA-seq data from multiple human cancer types	Qian et al.[91]	http://blueprint.lambrechtslab.org
Single-cell RNA-seq data from human ovary	Han et al.[92]	GSE134355
Single-cell RNA-seq data from human fallopian tube	Dinh et al.[93]	GSE151214
Single-cell RNA-seq data from human ovary	Fan et al.[94]	GSE118127
Single-cell RNA-seq data from human pancreas, intestine, and lung	Buechler et al.[95]	https://www.fibroxplorer.com/
Single-cell RNA-seq data from multiple human cancer and tissue types	Mulder et al.[96]	GSE178209
Single-cell RNA-seq data from multiple human cancer types	Cheng et al.[97]	GSE154763
Single-cell RNA-seq data from pre- and post-chemotherapy ovarian cancer patients	Zhang et al.[30]	GSE165897
Single-cell RNA/TCR-seq and bulk TCR-seq profiles	This study	GSE222557
Raw data for 10x single-cell RNA-seq profiles	This study	GSA for Human: HRA007180
Raw data for Singleron single-cell RNA-seq profiles	This study	GSA for Human: HRA007216
Raw data for Singleron single-cell TCR-seq profiles	This study	GSA for Human: HRA007181
Raw data for bulk TCR-seq profiles	This study	GSA for Human: HRA007230
Software and algorithms		
Adobe Illustrator	Adobe	https://www.adobe.com/products/illustrator.html
BioRender	BioRender	https://app.biorender.com/
CeleScope v.1.11.0b0	Singleron Biotechnologies	https://github.com/singleron-RD/CeleScope
CellChat v.1.5.0	Jin et al.[98]	https://github.com/sqjin/CellChat
cNMF v.1.4	Kotliar et al.[99]	https://github.com/dylkot/cNMF
decoupleR v.1.5.0	Badia-i-Mompel et al.[100]	https://github.com/saezlab/decoupleR

(Continued on next page)

Continued

REAGENT OR RESOURCES	SOURCE	IDENTIFIER
DeepCell v.0.12.2	Bannon et al.[101]	https://www.deepcell.org/about
DESeq2 v.1.30.1	Love et al.[102]	https://github.com/thelovelab/DESeq2
dplyr v.1.1.4	Wickham et al.[103]	https://dplyr.tidyverse.org
DropletUtils v.1.10.3	Lun et al.[104]	https://bioconductor.org/packages/DropletUtils
ggplot2 v.3.3.5	Wickham[105]	https://ggplot2.tidyverse.org
ggpubr v.0.6.0	Kassambara[106]	https://rpkgs.datanovia.com/ggpubr/index.html
ggsci v.3.1.0	Xiao[107]	https://nanx.me/ggsci/index.html
GATK v4.1.0.0	McKenna et al.[108]	https://github.com/broadinstitute/gatk
harmonypy v.0.0.9	Korsunsky et al.[109]	https://github.com/slowkow/harmonypy
inferCNVpy v.0.2.1.dev20	Patel et al.[110]	https://github.com/icbi-lab/infercnvpy
Jupyter Notebook v6.5.6	Kluyver et al.[111]	https://jupyter.org/
kb_python v.0.27.0	Melsted et al.[112]	https://github.com/pachterlab/kb_python
maftools v.2.20.0	Mayakonda et al.[113]	https://github.com/PoisonAlien/maftools
matplotlib v.3.7.3	Hunter[114]	https://matplotlib.org
milopy v.0.0.999	Dann et al.[47]	https://github.com/emdann/milopy
MiXCR v4.0.0b	Bolotin et al.[115]	https://github.com/milaboratory/mixcr
NumPy v.1.26.3	Harris et al.[116]	https://numpy.org/
pandas v.2.2.0	The Pandas Development Team[117]	https://pandas.pydata.org/
phenoptr v.0.3.2	Johnson[118]	https://akoyabio.github.io/phenoptr
Python v.3.10.13	Python Software Foundation	https://www.python.org
pyscenic v.0.11.1	Aibar et al.[46]	https://pyscenic.readthedocs.io
QuPath v.0.4.3	Bankhead et al.[119]	https://qupath.readthedocs.io
R v4.3.2	The R Foundation	https://www.r-project.org
Scanpy v.1.9.1	Wolf et al.[120]	https://scanpy.readthedocs.io
scipy v.1.12.0	Virtanen et al.[121]	https://github.com/scipy/scipy
Scirpy v.0.14.0	Sturm et al.[122]	https://scirpy.scverse.org
scrublet v.0.2.1	Wolock et al.[123]	https://github.com/swolock/scrublet
scVelo v.0.2.4	Bergen et al.[124]	https://scvelo.readthedocs.io
seaborn v.0.12.2	Waskom[125]	https://seaborn.pydata.org
Seurat v4.2.0	Hao et al.[87]	https://github.com/satijalab/seurat
scikit-learn v.1.4.0	Pedregosa et al.[126]	https://scikit-learn.org
symphony v.0.1.0	Kang et al.[127]	https://github.com/immunogenomics/symphony
Triku	Ascensión et al.[128]	https://triku.readthedocs.io
TRUST4 v.1.0.5	Song et al.[39]	https://github.com/liulab-dfci/TRUST4
UCell v.1.3.1	Andreatta et al.[129]	https://github.com/carmonalab/UCell
velocyto v.0.17	La Manno et al.[130]	https://velocyto.org/velocyto.py
Other		
Code	This study	https://zenodo.org/doi/10.5281/zenodo.10990093

RESOURCE AVAILABILITY

Lead contact
Further information and requests for resources and reagents should be directed to and will be fulfilled by the lead contact, Han Liang (hliang1@mdanderson.org).

Cell
Article

Materials availability

All unique/stable reagents generated in this study are available from the lead contact with a completed Materials Transfer Agreement.

Data and code availability

- Raw sequencing data have been deposited in the Genome Sequence Archive for Human at the National Genomics Data Center with accession number HRA007180 for 10x scRNA-seq, HRA007216 for Singleron scRNA-seq, HRA007181 for Singleron scTCR-seq, and HRA007230 for bulk TCR-seq. All records are under project PRJCA016620 (https://ngdc.cncb.ac.cn/bioproject/browse/PRJCA016620), which will be provided for scientific research upon request complying with the law due to human patient privacy concerns. Processed, de-identified scRNA-seq, scTCR-seq, and bulk TCR-seq profiles are publicly available at the Gene Expression Omnibus (GEO) with accession number GSE222557. This study also utilized existing, publicly available data, the accession numbers for which are listed in the key resources table.
- All original code has been deposited at Zenodo in the form of Jupyter Notebooks or R scripts (https://zenodo.org/doi/10.5281/zenodo.10990093).
- Any additional information required to reanalyze the data reported in this paper is available from the lead contact upon request.

EXPERIMENTAL MODEL AND STUDY PARTICIPANT DETAILS

Patient recruitment and sample collection

Niraparib-based neoadjuvant therapy in HGSOC patients with HRD is a multicenter, prospective, single-arm, open-label, phase II clinical study, and the comprehensive study design was described in our previous publication.[21] We consecutively recruited patients who were newly diagnosed with unresectable HGSOC (Fagotti score $\geq$ 8 or upper abdominal computed tomography [CT] score $\geq$ 3) and would receive neoadjuvant therapies followed by interval debulking surgery (IDS) to be the candidate population between March 5, 2021, and July 18, 2023.

HRD testing was performed on tumor biopsy samples (tumor content $\geq$ 30%) using a customized and validated HRD assay[131] that profiles germline and somatic mutations in a panel of 36 DNA damage repair genes and calculates a genomic instability score (GIS) in seven business days. Tumor samples with GIS $\geq$ 42 or with pathogenic or likely pathogenic BRCA mutations were defined as HRD, and the remaining were designated HRP. Niraparib was administered to eligible HRD patients at a dose of 200 or 300 mg (body weight $\geq$ 77 kg and platelet count $\geq$ 150000/UL) for 2 cycles, each lasting 28 days. Patients who were not interested in the clinical study (HRP or subjective rejection) were given carboplatin AUC = 5 and paclitaxel 175mg/m^2 every 3 weeks for 2–3 cycles. The responses to neoadjuvant therapies were determined according to Response Evaluation Criteria in Solid Tumors (RECIST), version 1.1 and the Gynecologic Cancer InterGroup (GCIG) CA125 response criteria,[22,23] as tumor burden changes and were categorized as complete response (CR), partial response (PR), or non-response (NR). Patients with CR or PR would subsequently receive IDS. The incidence of adverse events (AEs) at any grade during the treatment, surgery, and chemotherapy was estimated by Common Terminology Criteria for Adverse Events (CTCAE version 5.0).

This study was approved by the Ethics Committee of Tongji Medical College, Huazhong University of Science and Technology ([S122]-5) and strictly complied with the ethical principles in the Declaration of Helsinki, Good Clinical Practice, and applicable regulatory requirements. All patients provided informed consent for the collection of tissue and blood samples for research and genomic profiling. 34 patients were enrolled in the main scRNA-seq cohort, 17 of which received niraparib treatment, and 17 received chemotherapy. For these patients, we obtained a total of 67 tumor samples, including 24 matched pre- and post-treatment specimen pairs (Table S1). Additional tumor and blood specimens were collected for mIHC (Table S3), flow cytometry (Table S4), scRNA/TCR-seq (Table S5), and bulk TCR-seq (Table S6). Pre-treatment biopsies were collected via laparoscopic sampling before clinical enrollment. The site-matched post-niraparib tumor samples were collected via open laparotomy IDS when the patients completed the 2 cycles of niraparib, and an objective response assessment was performed. For patients with chemotherapy, the post-treatment samples were obtained through surgical resection, according to NCCN guidelines. All the tumor samples were collected strictly according to clinical practice guidelines.

Animals

Wild-type (WT) C57BL/6 mice were purchased from Vital River, homozygous B-h*CCR8* C57BL/6 mice (C57BL/6-*Ccr8*$^{tm1(CCR8)}$/Bcgen) were purchased from Biocytogen and h*CCR8* C57BL/6 mice (C57BL/6Smoc-*Ccr8*$^{em3(hCCR8)/Smoc}$) were purchased from Shanghai Model Organisms Center, Inc. All the mice studies were performed in compliance with the guidelines of Institutional Animal Care and the Ethics Committee of the Tongji Medical School, Huazhong University of Science and Technology (HUST, Wuhan, China).

METHOD DETAILS

Sample collection and processing

Peripheral blood was collected from donors using Streck Cyto-Chex BCT (Streck, La Vista, NE, USA). PBMCs were isolated from the peripheral blood with human PBMC separation liquid (Ficoll, TBD Science) and were re-suspended in 1 × PBS for further

immunostaining and T-cell sorting. Pre- and post-treatment tumor samples were site-matched and obtained as described above. Fresh pre-treatment tumor samples were shipped in Mylteni Biotec® Tissue Storage Solution and maintained at 4 °C until processing. An 8 cm^3 (2 × 2 × 2 cm) tumor tissue derived from each patient was cut into three pieces: one was sent to Precision Scientific laboratory for HRD testing, another was dissociated into a single-cell suspension for scRNA-seq, and the third was used to generate paraffin-embedded samples for IHC staining. The post-treatment tumor samples were divided into two pieces for scRNA-seq and IHC staining. To generate single-cell suspensions, tumor tissues were dissociated immediately after they arrived in the lab using the gentleMACS™ Dissociator with Heaters and the human tumor dissociation kit (Mylteni Biotec), as per the manufacturer's instructions. Following dissociation, single-cell suspensions were filtered using MACS SmartStrainers (70 μm and 40 μm). They were then treated with Red Blood Cell Lysis Solution and one or two rounds of dead cell removal using the Dead Cell Removal Kit, depending on the number of dead cells in each sample. Finally, cell pellets were re-suspended in 1 × PBS for further scRNA-seq or scTCR-seq.

HRD assay

Blood, formalin-fixed paraffin-embedded (FFPE) tissue specimens, and fresh tumor samples were collected for each participant. Genomic DNA was extracted from blood samples using the DNeasy Blood & Tissue Kit (QIAGEN). Blood samples were lysed in Proteinase K-supplemented lysis buffer. Buffering conditions were adjusted to provide optimal DNA-binding conditions, and the lysate was loaded onto the DNeasy Mini spin column or the DNeasy 96 plate. During centrifugation, the DNA was selectively bound to the DNeasy membrane, whereas contaminants passed through. The remaining contaminants and enzyme inhibitors were further removed in two wash steps, and the DNA was then eluted in water or buffer. The collected FFPE tumor specimens were stained with hematoxylin and eosin (H&E) to evaluate tumor purity. The process of HRD testing was only performed for samples with an estimated tumor purity of > 30%. Genomic DNA was extracted from fresh tumor samples using the DNeasy Blood &Tissue Kit and the above-mentioned protocol for blood samples. The purified DNA was quantified on a Qubit 4.0 (Life) to confirm a sufficient amount for downstream experiments. The extracted DNA from blood and fresh tumor samples was captured using the Precision Human HRD Assay (Precision Scientific (Beijing) Co., Ltd.), which is a customized panel of probes against sites of nucleotide polymorphisms to quantify GIS and genomic regions of 36 DNA damage repair genes for germline and somatic mutation calling. The captured DNA was sequenced on an Illumina NovaSeq 6000 NGS instrument.

scRNA-seq library preparation and sequencing

The scRNA-seq library was prepared with Chromium Next GEM Single Cell 3' Reagent Kits v.3.1 from 10x Genomics according to the manufacturer's instructions. In brief, the single-cell suspensions dissociated from tumors (derived from P01-P34) were centrifuged and washed twice with 1 × PBS, and then the single-cell pellets were re-suspended within 1 × PBS supplemented with 0.04% BSA at a final concentration of 1 × 10^6 cells/mL. About 10 μL of cell suspensions (≈ 10000 cells) were mixed with barcoded Single Cell 3' v.3.1 Gel Beads and Partitioning Oil to generate nanoliter-scale Gel beads in EMulsion (GEMs). Next, the GEMs were subjected to reverse transcription PCR using a T100 Thermal Cycler (Bio-Rad) in a 125 μL volume (program: 53 °C for 45 min, 85 °C for 5 min, hold at 4 °C) to obtain full-length cDNA with barcoding. After this, the first-strand cDNAs were incubated with Dynabeads Cleanup Mix to purify them from the PCR mix and then amplified using the Amplification Reaction Mix on a T100 Thermal Cycler (Bio-Rad) (program: 98 °C for 3 min, 98 °C for 15 seconds, 63 °C for 20 seconds, 72 °C for 1 min [step 2 to step 4 for total 12 of cycles], and hold at 4 °C). Subsequently, the amplified cDNA was used to generate a single-cell 3' gene expression dual index library using Chromium Next GEM Single Cell 3' Library Kit v.3.1 (10x Genomics). Finally, the well-prepared single cell 3' gene expression libraries were sequenced on an Illumina NovaSeq 6000 sequencer.

Flow cytometry and sorting for scTCR-seq and bulk TCR-seq

Single-cell suspensions were generated as described above. To sort CD3$^+$ T cells from tumors, the single-cell suspensions were pre-incubated with fixable viability dye (BioLegend) in 1 × PBS for ∼30 min and then labeled with surface antibodies: CD45-PE (BioLegend), CD3-APC (BioLegend), and CD19-FITC (BioLegend). To sort CD4$^+$ T cells, PBMCs were preincubated with a fixable viability dye and then stained with antibodies: CD4-PerCP/Cyanine5.5 (BioLegend) and CD8-FITC (BioLegend). After immunostaining, cell pellets were resuspended in 200 μL 1 × PBS supplemented with 0.5% BSA and EDTA. Sorting for scTCR-seq and bulk TCR-seq was performed on a FACSAria (BD Biosciences).

scTCR-seq library preparation and sequencing

The scTCR-seq library was generated using the sCircle® Single Cell Full-Length Immunoreceptor Library Kit (Singleron) according to the manufacturer's instructions. In brief, the sorted CD3$^+$ T cells from 10 patients were resuspended in cold PBS at a concentration of ∼ 3 × 10^5 cells/mL. Approximately 100 μL of homogenous cell suspension was injected into a prepared microchip via the inlet port slowly and let stand for 5 min at room temperature, allowing the suspension to fully enter the microwells. Following cell loading, 60 μL of the barcode beads suspension was loaded onto the microchip and incubated for 1 min. After three washes with PBS, 100 μL of prepared Lysis Mix was injected into the microchip to lyse the cells, leading to the released mRNA binding to the barcode beads. Immediately following mRNA capture, barcode bead retrieval was performed with a Singleron Magnetic Rack and pre-chilled wash buffer A (supplied by the Library Kit) to obtain the barcode beads with bound mRNA. The mRNA was reverse transcribed

on a thermal mixer preheated to 42 °C at 1300 rpm for 90 min, followed by cDNA amplification using a T100 Thermal Cycler (Bio-Rad). A portion of the purified cDNA was subjected to scRNA-seq library preparation. The remaining cDNA was used for scTCR-seq library preparation and programmed at cDNA circularization, digestion, and purification initially. After three rounds of TCR enrichment, the immune receptor enriched library was prepared through fragmentation, adapter ligation, purification of the adapter-ligated cDNA, enriched library amplification, and purification and size selection of the amplified enriched libraries. Lastly, the prepared libraries were sequenced on an Illumina NovaSeq 6000 Sequencer.

Bulk RNA isolation and TCR sequencing

DNA from CD4$^+$ T cells was extracted using the QIAamp DNA Mini Kit (QIAGEN). To generate the template library for the T-cell repertoire, multiplex PCR amplification of CDR3 of the TCR β chain (TRB) was conducted, including PCR1 and PCR2 inclusively and semi-quantitatively. Primers were designed to acquire maximum coverage of a heterogeneous set of target sequences of V and J families with a minimal PCR bias. Primer sequences were filed as part of a Chinese patent (CN105087789A). During the first round, 10 PCR cycles were used to amplify the CDR3 fragments using 32 forward primers for V genes and 13 reverse primers for J genes with a Multiplex PCR Kit (QIAGEN). Then, PCR1 was performed with 1 cycle of 95 °C for 15 min, 10 cycles of denaturation at 94 °C for 30 sec, and 10 cycles of annealing at 60 °C for 90 sec and extension for 30 sec at 72 °C. After a final extension for 5 min at 72 °C, the samples were held at 4 °C. The target fragment of the multiplex PCR products was purified with Agencourt magnetic beads (Beckman Coulter). In the second round, PCR2 was performed using universal primers with a KAPA HiFi HotStart ReadyMix PCR Kit (KAPA BioSystems) as follows: one cycle at 98 °C for 1 min; 20 cycles of denaturation at 98 °C for 20 sec, annealing at 60 °C for 30 sec, and extension at 72 °C for 30 sec; and a final extension at 72 °C for 5 min. The samples were then held at 4 °C. Final PCR products were purified again. The targeted fragments were retrieved using an E-Gel Power Snap Electrophoresis System (Invitrogen™). The library was assessed on an Agilent 2100 Bioanalyzer and the DNA HS kit (Agilent Technologies) to estimate fragment size distribution, while the library concentration was measured using a Qubit fluorometer and the Qubit dsDNA HS (High Sensitivity) Assay Kit (Invitrogen). Paired-end sequencing of libraries was carried out with a read length of 100 bp using the DNBSEQ-T7RS sequencer (MGI) platform.

DNA from patient-matched PBMC and tumor samples of ovarian cancer patients was extracted using the QIAamp DNA Mini Kit (QIAGEN) following the manufacturer's instructions. Multiplex PCR primers from Zhang et al.[132] were used to amplify the rearranged CDR3 regions of TCRβ, including 30 forward V primers and 13 reverse J primers. The reaction mix was prepared as follows: QIAGEN Multiplex PCR Master Mix (QIAGEN), 0.5 × Q solution, 0.2 μM VβF pool, and JβR pool were combined in a 50 μL volume. The cycling conditions were: 95 °C for 15 min, followed by 25–30 cycles at 94 °C for 30 sec, 60 °C for 90 sec, and 72 °C for 30 sec, with a final extension at 72 °C for 5 min. After multiplexed PCR, single-stranded PCR products were produced via denaturation and then underwent the circularization program. The replication of single-stranded circular DNA molecules was achieved through rolling cycle amplification, resulting in the generation of a DNA nanoball (DNB) containing multiple copies of DNA. High-quality DNBs were then loaded into patterned nanoarrays using MGISEQ 2000.

Flow cytometry for Treg quantification in human tumors

To determine Treg ratios in clinical specimens, fresh tumors derived from patients enrolled in the clinical trial were cut into pieces on ice and dissociated into single-cell suspensions using a gentleMACS™ Dissociator with Heaters and a Tumor Dissociation Kit, human (Miltenyi Biotec), as per the manufacturer's instructions. These single-cell suspensions were preincubated for ~30 min with Fixable Viability Dye (BioLegend) to stain dead cells and then labeled with surface antibodies, including CD45-PE (BioLegend), CD3-PC5.5 (BioLegend), CD4-BV785 (BioLegend), CD8-APC (BioLegend), CD25-BV510 (BD Biosciences), CD127-BV605 (BD Biosciences), and CCR8-BV421 (BD Biosciences). The fluorescence intensity was determined using a Beckman Coulter Cytoflex. FlowJo was used for data analysis.

Multiplex immunohistochemistry (mIHC)

For each clinical sample, a part of fresh tumor tissue was washed with PBS, fixed with formalin, and embedded in paraffin. Multiplex IHC was performed on serial tissue slides cut from these paraffine-embed samples following the manufacturer's instruction (Opal 6-plex Manual Detection Kit, NEL81100KT, Akoya Biosciences). Slides were stained with CD4 (Abcam), CD8 (Abcam), PD-1 (Cell Signaling Technology), TNFRSF9 (Cell Signaling Technology), FOXP3 (Abcam), pan-cytokeratin (Abcam), and DAPI (Thermo Fisher Scientific) in the order mentioned. All primary antibodies were incubated overnight in a cryogenic laboratory for more specific antigen-antibody binding. Then, the slides were blocked with an antifade mounting medium and scanned by PHENO IMAGER^{HT} (Akoya Biosciences).

Cell culture and treatment

Human breast cancer cell lines (BT-549 and MDA-MB-231), ovarian cancer cell lines (OV90 and SKOV3), and HEK293T cells were purchased from ATCC. Human ovarian cancer cell line A2780 was purchased from Sigma-Aldrich and OVCAR8 was obtained from MDACC's Characterized Cell Line Core. MDA-MB-231 and HEK293T cells were cultured in DMEM (Thermo Fisher Scientific) supplemented with 10% FBS (Gibco) and penicillin-streptomycin solution (Thermo Fisher Scientific). BT-549, A2780, and OVCAR8 cells were cultured in RPMI 1640 medium (Thermo Fisher Scientific) with 10% FBS (Gibco) and penicillin-streptomycin solution (Thermo Fisher Scientific). OV90 cells were cultured in MCDB 105 medium (Sigma-Aldrich) and 199 medium (Thermo Fisher Scientific) with

10% FBS (Gibco) and penicillin-streptomycin solution (Thermo Fisher Scientific). SKOV3 cells were cultured in McCoy's 5A medium (Thermo Fisher Scientific) supplemented with 10% FBS (Gibco) and penicillin-streptomycin solution (Thermo Fisher Scientific). Mouse breast cancer cell line EO771 was purchased from ATCC and mouse ovarian cancer cell line ID8 was obtained from Sigma-Aldrich. EO771 and ID8 cells were cultured in DMEM with 10% FBS (Gibco) and penicillin-streptomycin solution (Thermo Fisher Scientific).

All cells were seeded in 12-well culture plates at a density of 1×10^5 cells per well. Recombinant human IFN-α (Acro biosystems), IFN-β (PeproTech), and IFN-γ (PeproTech) were added to the wells at different final concentrations ranging from 0.1 ng/mL to 20 ng/mL to stimulate the tumor cells for 48 h. Subsequently, these treated cells were harvested and subjected to flow cytometry.

Transfection of small interfering RNA (siRNA)
Control siRNA, *BRCA1* siRNA, and *BRCA2* siRNA were purchased from Ribo Life Science (custom service). These siRNAs were transfected into tumor cells using Lipofectamine™ 3000 (Thermo Fisher Scientific) according to the manufacturer's instructions. The sequences are as follows:

si*BRCA1*
#1 CCACACGATTTGACGGAAA
#2 GCAGGAAATGGCTGAACTA
si*BRCA2*
#1 GAAGAACAATATCCTACTA
#2 CATGGAATCTGCTGAACAA

Total RNA extraction and real-time PCR
Total RNA from tumor cells was extracted using TRIzol reagent (Sigma-Aldrich) and reverse transcribed using a Reverse Transcription Kit (Vazyme) according to the manufacturer's protocol. Real-time PCR was performed using SYBR Green (Bio-Rad Laboratories) on a Bio-Rad CFX Connect instrument. The expressions were quantified using the comparative Ct ($2^{-\Delta\Delta Ct}$) method. The Ct value for each sample was normalized to that of the *GAPDH* gene. The primer sequences for *GAPDH*, *BRCA1*, and *BRCA2* are as follows:

GAPDH-F, GTCTCCTCTGACTTCAACAGCG
GAPDH-R, ACCACCCTGTTGCTGTAGCCAA
BRCA1-F, CTGAAGACTGCTCAGGGCTATC
BRCA1-R, AGGGTAGCTGTTAGAAGGCTGG
BRCA2-F, GGCTTCAAAAAGCACTCCAGATG
BRCA2-R, GGATTCTGTATCTCTTGACGTTCC

CRISPR/Cas9
The guide RNAs (gRNA) targeting *Trp53* exon5, *Brca1* exon 10, and *Brca2* exon 3 were designed according to a previous publication.[133] After being annealed in a thermocycler, these oligos were cloned into the LentiCRISPRv2 plasmid (Addgene). All plasmids were sequenced to confirm successful ligation and the gRNA sequences are as follows:

Trp53 exon 5, TGAGCGCTGCTCCGATGGTGA and AGTGAAGCCCTCCGAGTGTC
Brca1 exon 10, GACTCCTTCCCAGGACAACT and TGTCTACATTGAACTAGGTA
Brca2 exon 3, TGCTTTGGCATATTATACGG and TAGGACCGATAAGCCTCAAT

For virus packaging, HEK293T cells were plated on 6 cm dishes at 3,600,000 cells per dish in antibiotic-free DMEM overnight. Cells were co-transfected the following day with 6 mg of lentiviral transfer plasmid, 4.5 mg of psPAX2 (Addgene), and 3 mg of pMD2.G (Addgene) packaging plasmids using HP DNA Transfection Reagent (Roche). The culture medium was refreshed 18 h after transfection and harvested 48 h later.

For the generation of *Trp53*- or *Brca1/2*-deficient cell lines, EO771 and ID8 cells were transfected with lentiviruses using polybrene (2.5 μg/mL), selected under puromycin (2.5 μg/mL) for 72 h, and sorted into single wells for the single-cell clonal expansion. The expanded single-cell colonies were used for mouse model generation after verifications with DNA sequencing.

To validate the status of mutation in these engineered cells, total DNA was extracted using the QIAamp DNA Mini Kit (QIAGEN) according to the manufacturer's instructions. PCR was performed using Platinum™ SuperFi II DNA (Thermo Fisher Scientific) to amplify the DNA strands spanning potential sites of deletion. These PCR products were cloned into Blunt Simple Cloning Vector (TRANS) and subjected to Sanger sequencing to select clones with large fragment deletion or frameshift mutations in all alleles. PCR primer sequences are as follows:

Brca1-F, CTGAGTCCAAAGGTGACAGCT
Brca1-R, GTGTTGGAAGCAGGGAAGATC

Cell
Article

🔗 **CellPress**
OPEN ACCESS

Brca2-F, GCCTTGGTCGTGGTGTCTG
Brca2-R, TGCCCAAAGTCCCAGTTCA
Trp53-F, ATCCACAGCCATCACCTCACT
Trp53-R, GAACTTTTGTCCCTCCCACTTT

Mouse models

Mouse ovarian cancer model

To generate mouse orthotopic ovarian cancer models, mouse *Trp53* and *Brca1* double genetic knockout (KO) ID8 cells (3×10^6/mouse) were resuspended in 30 μL PBS mixed with Matrigel at a ratio of 1:1 and transplanted into h*CCR8* or WT C57BL/6 mice via intrabursal injection. After about 2 weeks of transplantation, the two types of tumor-bearing mice were randomly divided into 4 treatment cohorts, respectively: control, niraparib, anti-CCR8 or anti-CD25 monoclonal antibody (mAb), and niraparib combined with anti-CCR8 or anti-CD25 mAb. h*CCR8* C57BL/6 mice received niraparib (40 mg/kg, oral administration) 5 times a week and anti-CCR8 mAb (3 mg/kg, intraperitoneal administration) twice a week. WT C57BL/6 mice received niraparib (40 mg/kg, oral administration) 5 times a week and anti-CD25 mAb (200 μg/mouse, intraperitoneal administration) once a week. The tumor volumes were monitored every week and calculated as luminescence intensity per sec using an IVIS® Lumina III In Vivo Imaging System (PerkinElmer). After 4 or 5 weeks of treatment, the presence of ascites and tumor weights were recorded, and the immune status in tumors was accessed using flow cytometry and IHC staining.

Mouse breast cancer model

To generate mouse orthotopic breast cancer models, mouse *Brca2* KO EO771 cells (5×10^5/mouse) were resuspended in 100 μL PBS mixed with Matrigel at a ratio of 1:1 and transplanted into 4th inguinal mammary fat pad of h*CCR8* C57BL/6 mice. Mouse *Brca1* KO EO771 cells (5×10^5/mouse) were also transplanted into the 4th inguinal mammary fat pad of WT C57BL/6 mice. The tumor volumes were measured every day or every other day and calculated as L × W × W ×1/2, where L is length and W is width. Once the tumor volumes reached ∼50 mm³, the tumor-bearing h*CCR8* mice were treated with niraparib (40 mg/kg, oral administration) 5 times a week and anti-CCR8 mAb (3 mg/kg, intraperitoneal administration) twice a week, Tumor-bearing WT mice were treated with niraparib (40 mg/kg, oral administration) 5 times a week and anti-CD25 mAb (200 μg/mouse, intraperitoneal administration) once a week. The EO771 tumors were harvested, and their immune status was evaluated using flow cytometry and IHC staining.

Flow cytometry for Treg and Tex quantification in mouse tumors

To determine the ratios of Tregs in mouse tumors, fresh tumors were cut into pieces on ice and dissociated into single-cell suspensions using a gentleMACS™ Dissociator with Heaters and a Tumor Dissociation Kit, mice (Miltenyi Biotec), as per the manufacturer's instructions. After incubation with Fixable Viability Dye (BioLegend) and surface protein antibodies, including CD45-PE-CY7 (BD Biosciences), CD3-PC5.5 (BD Biosciences), CD4-FITC (BD Biosciences), CD8-BV610 (BD Biosciences), CD25-BV510 (BioLegend), CCR8-APC (BioLegend), and PD-1-BV785 (BioLegend), the cells were fixed and permeabilized with a Fixation/Permeabilization Solution Kit (BD Biosciences) according to manufacturer's instructions. The fixed cells were subsequently incubated with FOXP3-BV421 antibodies (BD Biosciences) in 1× perm buffer for 1 h at 4°C. For the determination of Tex cells in mouse tumors, CD45-PE-CY7 (BD Biosciences), CD3-APC (BD Biosciences), CD4-FITC (BD Biosciences), CD8-BV605 (BD Biosciences), TIM3-PE (BD Biosciences), and PD-1-BV785 (BioLegend) antibodies were used. After three washes with PBS, the fluorescence intensity was determined using a Beckman Coulter Cytoflex. FlowJo was used for data analysis.

Dual-target immunofluorescence for Treg quantification in mouse tumors

Treg density in mouse tumors was evaluated in FFPE tumor slide specimens using dual-target immunofluorescence. Briefly, antigen retrieval, nonspecific antigen blocking, and incubation of primary and fluorescence-labeled secondary antibodies and DAPI were sequentially performed. The following antibody combinations were used: anti-mouse PD-1 (Cell Signal Technology) and anti-human/mouse FOXP3 (Abcam). Whole slide scans were acquired using the Pannoramic SCAN (3DHISTECH) digital pathology scanning system.

HRD and mutation analysis

After mapping sequenced reads to the human reference genome (GRCh37), we first calculated the GIS using an in-house algorithm.[131] This algorithm estimated three genomic features, loss of heterozygosity, telomeric allelic imbalance, and large-scale transition. The GIS was the unweighted sum of the three values. We then called germline and somatic mutations using GATK HaplotypeCaller and Mutect2,[108] respectively. Non-silent somatic mutations (or somatic and germline mutations for *BRCA1/2* and *TP53*) with a prevalence of < 0.01 in cohorts of 1000 Genomes, ExAC, or gnomAD resources are summarized in Table S2 and were visualized using oncoplot.[113] Mutations were further manually curated to be pathogenic or likely pathogenic according to the recommendations of the American College of Medical Genetics and Genomics (ACMG)[134] and the AMP/ASCO/CAP Somatic Variants Guideline[135] in the interpretation of sequence variations. Finally, the HRD status of a sample was defined as positive if the GIS was ≥ 42 or if there were pathogenic/likely-pathogenic *BRCA1/2* germline or somatic mutations.

CellPress
OPEN ACCESS

Cell
Article

scRNA-seq data preprocessing and quality control

FASTQ files were processed using kallisto-bustools[112] to obtain gene-level UMI counts for each droplet, with the GENCODE v37 human genome as the reference. The kallisto-bustools workflow was set to "standard" so that only exonic reads would be counted towards the final UMI count. We then devised a biology-aware multi-layer workflow to process and quality-control these raw count matrices to ensure a robust balance between the removal of low-quality droplets and the preservation of small-RNA-content cells. This was an essential step tailored to scRNA-seq data generated from tumor samples where cell sizes of different populations can be drastically different, and a universal hard-set threshold would thus not be suitable.

First, we focused on assessing the overall data quality of each sample and leniently removing empty droplets by visualizing a panel of key droplet-level statistics. EmptyDrops in the DropletUtils[104] package was used to calculate the probability of each droplet being an empty droplet. The inflection point was used as a cutoff below which all droplets were deemed empty and would form an ambient pool for the remaining droplets to be compared against. Then, plots depicting multiple key metrics and the interactions thereof were inspected. These include (i) a scatter plot showing the relationship between UMI count and gene count in each droplet to evaluate the level of sequencing saturation and detect clear outliers; (ii) a knee plot showing the log rank of droplets by UMI count to judge the level of separation between empty droplets and cell-containing droplets; (iii) a knee plot showing the log rank of droplets by UMI count, the same as above; (iv) a density plot showing the distribution of mitochondrial DNA (mtDNA) UMI count proportion to help assess the magnitude of mitochondrial contamination; (v) a scatter plot showing the relationship between gene count and mtDNA UMI count proportion to detect the segregation between a low-mtDNA high-transcriptome-diversity (i.e., with a high gene count) cluster and a high-mtDNA low-transcriptome-diversity cluster; (vi) a scatter plot showing the relationship between UMI count and -log(empty drop probability) to visualize the estimation by EmptyDrops of the probability of each droplet being a real cell-containing data point. The samples that passed these criteria were retained, and within each sample, droplets that passed the EmptyDrops FDR threshold of 1% were retained.

Second, we took into consideration the clustering information that would inform the collectively abnormal behavior of a group of cells to further perform quality control on a reduced-dimension space. Scrublet[123] was employed to calculate a doublet score for each retained cell. We then followed the downstream analysis workflow implemented in Scanpy.[120] Specifically, we (i) applied the log1pCP10K normalization to the raw counts, (ii) selected highly variable genes using a dispersion-based method (the maximum and minimum average expression of a gene were set to be 3 and 0.0125, respectively, and the lower expression dispersion cutoff was set to 0.5) or through Triku,[128] (iii) regressed out the effects of the total count per cell and the percentage of mitochondrial gene count, (iv) scaled the normalized and regressed counts so that the data had unit variance and zero mean (any values above 10 were clipped), (v) calculated the first 50 principal components, (vi) reduced the data dimension through UMAP, and (vii) clustered the single cells using an unsupervised graph-based clustering algorithm, Leiden. By overlaying the UMI count, mitochondrial and ribosomal UMI proportions, doublet score, and EmptyDrops FDR values on top of the UMAP space, we identified clusters enriched for low-quality cells to discard. For example, a cluster where most cells had a low UMI count, high mitochondrial UMI fraction, and high empty droplet probability would most likely be apoptotic cancer cells and were filtered out. Importantly, this observation is usually not readily noticeable in the first layer of QC.

Third, we relied on prior biological knowledge to further investigate any aberrant entities in the dataset. Specifically, we built upon the UMAP space in the second layer of QC, identified cluster-specific marker genes using Student's t-test, and annotated the clusters based on the expression patterns of literature-derived marker genes along with the annotations from the original studies. This step helped us understand the presence/absence of biological identities that are common across cancer types or specific to ovarian cancer and thus served as a further control for data quality.

Notably, these three QC phases were not conducted in a strictly sequential manner. Instead, every piece of new information manifested in each stage could facilitate the clarification of unsolved situations in the other stages. For example, we may see a small cluster in stage 2 that shows a significantly lower UMI count than the rest of the dataset and mark it as a potential ambient droplet cluster. However, when QC stage 3 reveals that this cluster is annotated as T cells and that this sample is highly enriched in tumor cells, we would then discard the mark and instead choose to retain these cells. This is because we would then understand that this cluster being an outlier in terms of low UMI count reflects an authentic RNA content difference between immune cells and cancer cells.

scRNA-seq data integration and annotation

After the preprocessing and QC of each sample as described above, we started over with the count matrices and followed the same workflow in QC stages 2 and 3. Additionally, we applied Harmony[109] to remove sample-level batch effects after calculating the principal components and before conducting UMAP-based dimension reduction. We evaluated the effectiveness of data integration by (i) a qualitative visual inspection of the UMAP plots before and after integration to confirm that the cells were clustered by cell type instead of the sample source; (ii) a quantitative assessment of batch effect based on a sample-level silhouette coefficient across cell types where a lower value after integration indicated a reduction in sample-driven cell clustering.

For cell type annotation, we first identified 10 major cell types based on the expression patterns of well-established marker genes. These include *MS4A1* and *CD79A* for B cells, *EPCAM* and *KRT19* for epithelial cells, *PLVAP* and *PECAM1* for endothelial cells, *COL1A1* and *BGN* for fibroblasts, *TPSB2* and *CPA3* for mast cells, *AIF1* and *LST1* for myeloid cells, *MZB1* and *DERL3* for plasma cells, *RGS5* and *COL18A1* for pericytes, *CD2* and *CD3D* for T cells and NK cells, and *IRF7* and *LILRA4* for plasmacytoid

dendritic cells. Next, for each major cell type, we concatenated and reprocessed the count matrices using the same workflow and parameters as described above. We then identified the subordinate cell states through an extensive search of the literature and combined a set of complementary approaches to assign these states to each subpopulation (Figure S3), including (i) examining the expression distribution of known gene markers across cell clusters. For example, the area within the CD4^{+} T cell space that is positive for both *FOXP3* and *TNFRSF18* would be annotated as eTregs. (ii) Calculating for every single cell a score of a specific gene signature that was derived from the literature to mark a relevant cell state. For example, we annotated a cluster of CD8^{+} T cells as effector exhausted T cells because of their high scoring of the "CD8 dysfunction" signature from a study by Li et al.[136] We used UCell[129] for signature scoring. All public cell state gene signatures used to score single cells are listed in Table S7. (iii) Projecting the cells onto reference atlases that represent a comprehensive coverage of known cell states within a major cell type and have high-quality annotation information. For example, we identified mesothelial antigen-presenting cancer-associated fibroblasts based on a projected identity of these cells being "CALB2^{+} FIB" in a reference by Qian et al.[91] Symphony[127] was used for reference construction and application. All public scRNA-seq datasets used to build reference atlases are cataloged in Table S7.

Because cancer cells uniquely have their cell states largely driven by underlying patient-specific somatic alterations, we employed a different strategy to first distinguish malignant cells from normal epithelial cells and then their states. We first applied inferCNV[137] to compute a single-cell copy number variation (CNV) profile for all epithelial cells within each sample. Then, we used the CNV profiles rather than the original gene expression profiles as the basis for dimension reduction and clustering. We found a significant agreement between high-CNV-based cancer cell assignment and reference-projection-based secretory epithelial cell characterization (known to be the cells of origin for most ovarian cancers[138]), enabling a robust separation between normal and malignant epithelial cells. Finally, we used consensus non-negative matrix factorization (cNMF)[99] to identify recurrent cancer cell states across patient samples. This analysis led to a three-state annotation of cancer cells into an IFN-responding cluster, a proliferative cluster, and a non-proliferative cluster.

scRNA-seq data analysis of T cells in an external cohort

For independent validation, we downloaded single-cell gene expression profiles of ovarian cancer samples from a recent study[30] as UMI counts from the Gene Expression Omnibus (GEO) under the accession number GSE165897. This published cohort contains 11 HGSOC patients who received NACT and had paired pre- and post-treatment samples collected for scRNA-seq. No QC was further applied beyond what was already conducted by the original study. We first extracted T cells and then employed the same processing workflow for this dataset as for our in-house dataset. To ensure a direct comparative analysis between the two datasets, we used the same set of marker genes, signatures, and reference atlases to annotate the T cell states in this cohort under the same nomenclature scheme. We further interrogated the all-cluster-by-all-cluster overlap of cell state marker genes to demonstrate a good concordance between the two annotated T cell spaces.

Comparative and correlative analysis of cell state proportions

Annotated cell states were organized in a hierarchy supported by the literature. Differential abundance testing and correlation testing were performed on the proportion of a specific cell state (the numerator) among its immediate preceding cell state or cell type (the denominator). For example, the number of CD4^{+} T cells served as the denominator when testing for Treg abundance shift, while the number of Tregs was the denominator when testing for terminal eTreg abundance shift. To avoid spurious testing results, we removed samples in which the cell count of a cell state serving as the denominator was < 50.

Graph-based differential abundance testing

To detect cell-state abundance changes between different conditions in an annotation-free manner, in addition to the direct comparison based on population fractions, we performed differential abundance testing analysis using the milopy package.[47] Specifically, cell neighborhoods were first defined on a k-nearest neighbor (kNN) graph. Differential abundance testing was then performed for each neighborhood using a negative binomial general linear model framework.

Inference of eTreg infiltration in bulk RNA-seq data

To obtain an eTreg signature, we combined the top 10 differentially expressed genes in eTregs derived from our scRNA-seq data. To account for the infiltration level of total CD4^{+} T cells in a bulk tumor, we further calculated the ratio of the geometric FPKM average of the eTreg signature over the FPKM of the *CD4* gene. As FPKM values are of a linear scale, such ratios served as a proxy of the relative abundance of eTregs to all CD4^{+} T cells in a bulk tumor profiled by RNA-seq, allowing us to compare it between HRD and HRP HGSOC tumors in the Cancer Genome Atlas (TCGA).[139]

RNA velocity analysis

For scRNA-seq data generated through the 10x platform, spliced and unspliced UMI counts for each gene in each cell were counted using kallisto-bustools with the workflow set to "nucleus" and using an intron-containing index. For scRNA-seq data generated through the Singleron platform (for paired scRNA/TCR-seq), the same count tables were obtained using Velocyto[130] with intermediate bam files as the input. Subsequent analyses were performed using Scanpy and scVelo.[124] Specifically, library size

normalization and log transformation were applied to the count matrices. The top 2,000 genes with the highest expression dispersion were then selected for subsequent velocity computation. Next, for each cell, the moments (means and uncentered variances) of normalized spliced/unspliced counts were computed using the 30 nearest neighbors. RNA velocity estimation was then conducted with the mode set to "deterministic." We then used the gene expression graph used for clustering and annotation to embed RNA velocities in the UMAP space in the form of streamlines to facilitate a direct interpretation of velocities on top of the original annotated space.

Gene regulatory network analysis
Activated regulons in each subpopulation of Treg and Tex cells were analyzed using SCENIC[46] with a raw count matrix as input. Briefly, the co-expression network was calculated by GRNBoost2, and the regulons were identified by RcisTarget. Next, the regulon activity for each cell was scored by AUCell. The differentially activated regulons in each Treg or Tex subset were identified by a Wilcoxon test using cells from the other subsets as control. The Benjamini-Hochberg test was used to correct multiple hypotheses.

Paired scRNA/TCR-seq data analysis
For scRNA-seq data, FASTQ files were processed using the CeleScope (https://github.com/singleron-RD/CeleScope) "rna" workflow, designed for transcriptome sequencing data generated through the Singleron platform, to obtain gene-level UMI counts for each droplet, with GENCODE v37 human genome as the reference. Briefly, after using fastqc (https://www.bioinformatics.babraham.ac.uk/projects/fastqc/) and cutadapt[140] to QC and filter the data, reads were compared with the reference genome using STAR.[141] Finally, featureCounts[142] was used to generate the gene count matrices. The same preprocessing, QC, and downstream analysis workflows for the main cohort were applied again. For paired same-cell scTCR-seq data, FASTQ files were processed using CeleScope "flv_CR" workflow, designed for full-length VDJ enrichment sequencing data generated through the Singleron platform, to obtain TCR α- and β-chain CDR3 nucleotide sequences. Only the assembled chains that were productive, high confidence, full length, and had a valid cell barcode and an unambiguous chain type assignment were retained. If a cell had > 2 qualified chains of the same type, only the chain with the highest UMI count was qualified and retained. Single-cell CDR3 sequences were used for downstream analysis with Scirpy.[122] Clonotypes were determined based on identical CDR3 nucleotide sequences for both arms. Expanded clones were determined by a clonal size of > 1. The magnitude of TCR repertoire overlap between different T cell subpopulations was calculated using the Jaccard index.

TCR clonotype reconstruction from non-VDJ-enriched scRNA-seq data
TCR CDR3 sequences were extracted from the scRNA-seq FASTQ files using TRUST4,[39] and sample cells with at least one productive chain (either α- or β-chain) were retained. Samples with > 25 cells matching this criterion were retained for subsequent analysis with Scirpy. Due to data sparsity of the inferred CDR3 profiles, we employed a relaxed definition of TCR clone by only requiring either of the two chains to have identical CDR3 nucleotide sequences. We called expanded TCR clones based on them containing at least two cells. TCR clonotype overlap was measured by the Jaccard index. The quality of CDR3 inference by TRUST4 was evaluated by examining (i) the agreement between the enrichment of T cell gene marker expressions and that of TCR UMI count, (ii) the proportion of expanded clones that only contained cells from the same patient, thus meeting the standard of being a "private" clone, and (iii) the concordance between the relative expansion magnitudes across different T cell subpopulations based on the inferred CDR3 profiles and those based on VDJ-enriched *bona fide* CDR3 profiles.

Bulk TCR-seq data processing and analysis
Sequences were processed and analyzed using MiXCR.[115] PBMC bulk TCR-seq clonotypes were associated with patient-matched intratumoral single-cell TCR clonotypes by matching their TCR β-chains based on identical nucleotide sequences.

Pseudobulk analysis
To suppress false positive discoveries in differential expression analyses using single cells as data points for statistical testing, we employed a pseudo-bulk alternative.[143] Briefly, for cells of a specific combination of a cell state and an HRD status/treatment group, we first aggregated reads across biological replicates, transforming a genes-by-cells matrix to a genes-by-replicates matrix using matrix multiplication. Then, we ran DESeq2,[102] which used a Wald test of the negative binomial model coefficients to compute the statistical significance.

mIHC Image analysis
For each slide, 8 fields of view (FoVs) were obtained, and cell segmentation was performed using the adaptive cell segmentation setting in image analysis software (InForm v.2.6.0, Akoya Biosciences/PerkinElmer). Then, the cytoplasmic (CD4, CD8, PD-1, TNFRSF9, panCK) and nuclear (FOXP3) optical signals in the spectral unmixing image were isolated and quantified. The data was consolidated with the phenoptr v.0.3.2 package for R software and was analyzed with reference to described analysis in a previous study.[144] Specifically, thresholds for both the mean pixel intensity and the total pixel intensity for all channels were manually thresholded in each slide and evaluated by 4 independent researchers. The specificity and sensitivity of the positive threshold were further adjusted carefully in all FoVs using a visualization strategy where the positive cells of each marker are mapped onto the spectral
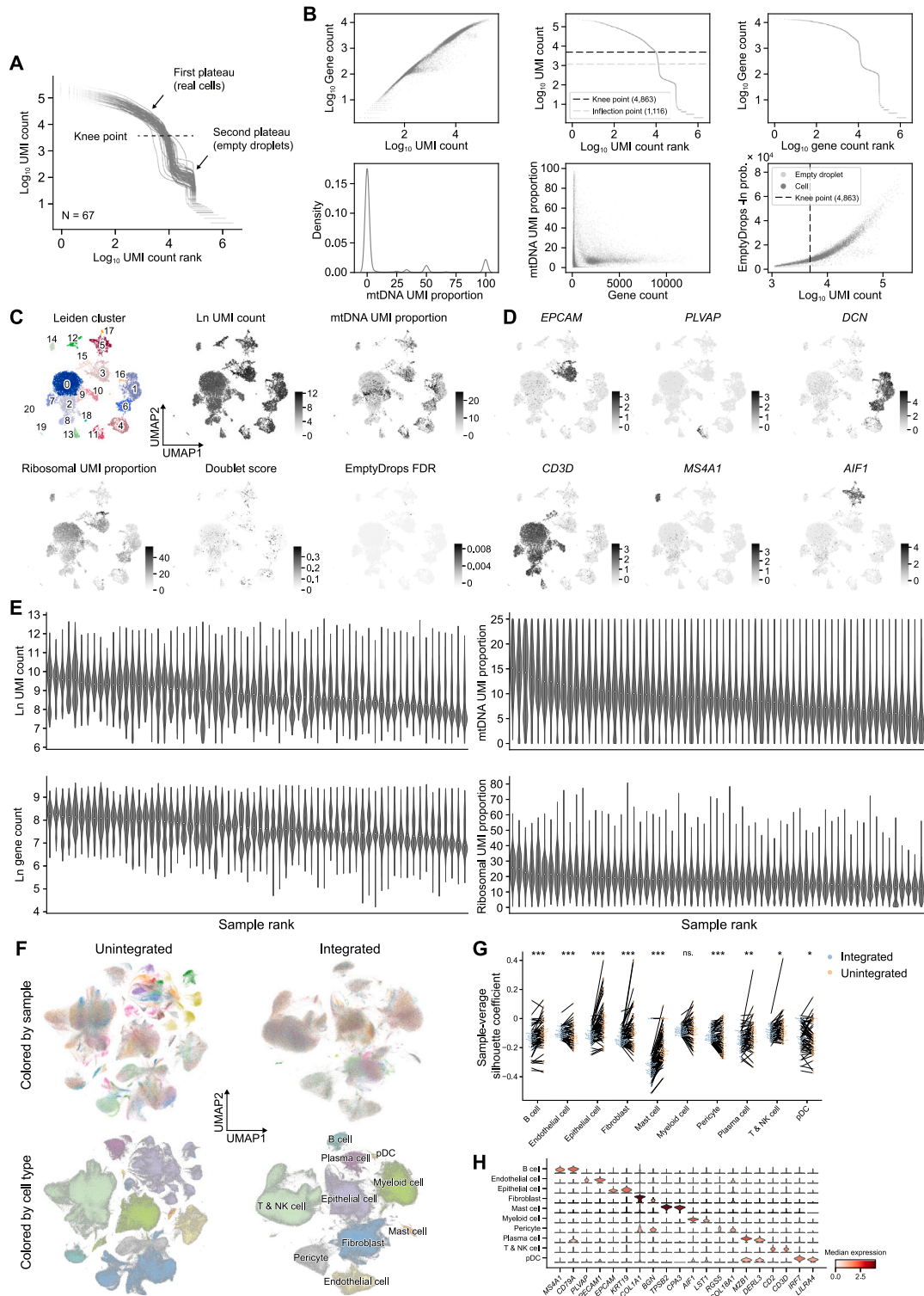
Cell
Article

CellPress
OPEN ACCESS

unmixing image of the corresponding channel. Each cell phenotype was evaluated as the average percentage of CD4$^+$ or CD8$^+$ T cells. The inter-cellular distance between nearest neighbors was calculated using the phenoptr package. Briefly, for each cell in a FoV, the distance matrix was used to find the nearest neighbor cell in each of the provided phenotypes, and the cell ID and distance to the nearest neighbor cell were reported. After that, the median distance from the panCK$^+$ cells to the target cells was computed among all cells of the desired marker combination.

QUANTIFICATION AND STATISTICAL ANALYSIS

All details related to statistical analysis can be found in figure legends and in the corresponding methods. No statistical methods were used to predetermine sample sizes. Data met the assumptions of the statistical tests used and were tested for normality. Statistical significance was set at $p < 0.05$.

Supplemental figures

Figure S1. Quality control and overview of scRNA-seq data, related to Figure 1

(A) Aggregated knee plots across samples show a robust separation between empty and cell-containing droplets.

(B) An example of the first-layer quality control. The first scatter plot shows the correlation between UMI count and gene count per cell. The second and third panels are knee plots showing the rank of droplets by UMI or gene count, respectively. The density plot in the fourth panel shows the distribution of the proportion of mtDNA UMI counts. The fifth panel is a scatter plot that shows the relationship between gene count per cell and mtDNA UMI proportion per cell. The scatter plot in the sixth panel shows the association between UMI count per cell and the probability of a droplet being empty as calculated by EmptyDrops. For the convenience of visualization, some metrics were logarithmically transformed, as labeled on the panels.

(C) An example of the second-layer QC. UMAP embedding of cells that have passed the first layer of QC filtering, overlaid with total UMI count, mtDNA UMI rate, ribosomal UMI rate, doublet score, and the false discovery rate (FDR) value of droplets being empty.

(D) An example of the third-layer QC. UMAP embedding of cells that have passed the second layer of QC filtering, overlaid with normalized expression levels of cell type-specific marker genes (*EPCAM* for epithelial cell, *PLVAP* for endothelial cell, *DCN* for fibroblast, *CD3D* for T cell, *MS4A1* for B cell, and *AIF1* for myeloid cell).

(E) The distributions of log-transformed UMI count (top left), gene count (bottom left), mtDNA UMI proportion (top right), and ribosomal UMI proportion (bottom right) of all scRNA-seq samples. Samples are ordered according to the median value of each metric.

(F) UMAP embeddings of unintegrated (left) contrasted with integrated (right) cells colored by sample (top) and cell type (bottom).

(G) Difference in cluster-average silhouette coefficient between unintegrated and integrated spaces across major cell types, using sample IDs as cluster labels (n = 67 samples, two-sided paired Wilcoxon rank-sum test, ns, non-significant, *$p < 0.05$, **$p < 0.01$, ***$p < 0.001$).
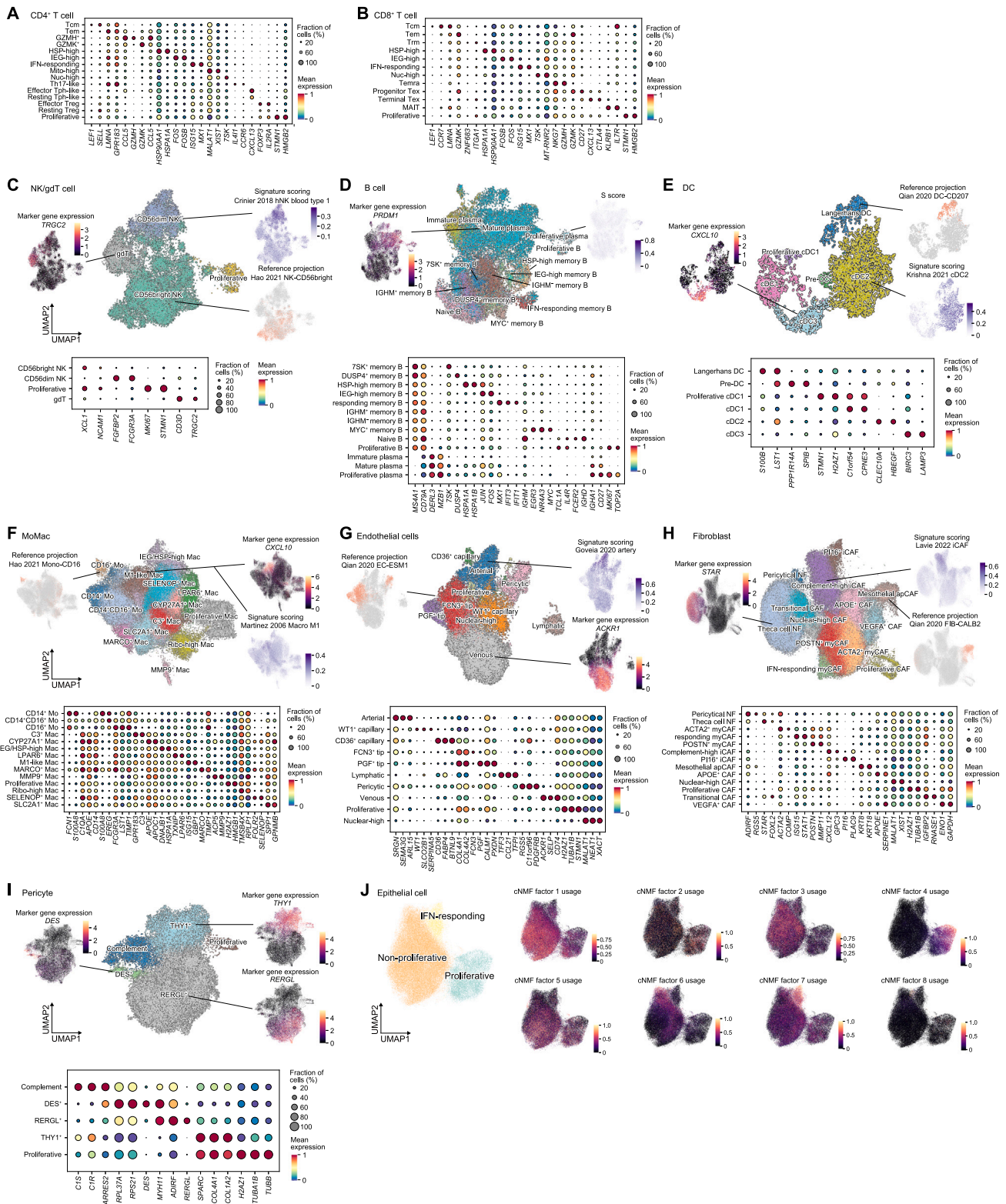
(H) Expression levels of marker genes across 10 major cell types.
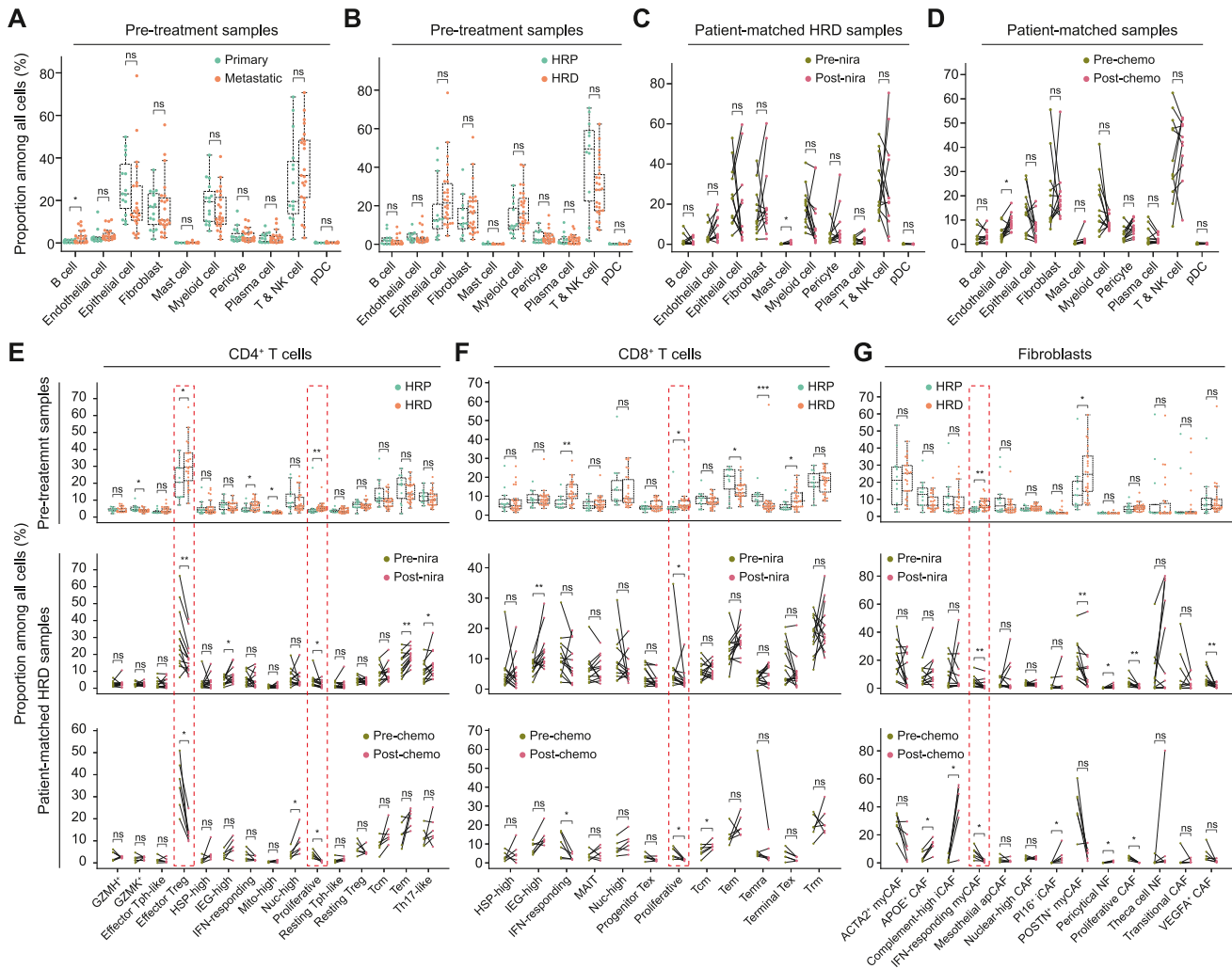
Figure S2. Differential abundance testing of major cell types and minor cell states, related to Figure 2

(A–D) Difference in major cell type proportion between pre-treatment primary versus metastatic (A, $n = 15$ primary samples, $n = 23$ metastatic samples, two-sided Mann-Whitney U test, ns, non-significant. $*p < 0.05$), pre-treatment HRP versus HRD (B, $n = 12$ HRP samples, $n = 26$ HRD samples, two-sided Mann-Whitney U test, ns, non-significant), pre-nira versus post-nira (C, $n = 12$ pre-nira samples, $n = 12$ post-nira samples, two-sided paired Wilcoxon rank-sum test, ns, non-significant. $*p < 0.05$), or pre-chemo versus post-chemo (D, $n = 12$ pre-chemo samples, $n = 12$ post-chemo samples, two-sided paired Wilcoxon rank-sum test, ns, non-significant. $*p < 0.05$) samples.

(E–G) Difference in cell-state proportion for CD4$^+$ T cells (E), CD8$^+$ T cells (F), and fibroblasts (G). Top, pre-treatment HRP versus HRD ($n = 12$ HRP samples, $n = 26$ HRD samples, two-sided Mann-Whitney U test, two-sided Mann-Whitney U test, ns, non-significant, $*p < 0.05$, $**p < 0.01$, $***p < 0.001$). Middle, pre-nira versus post-nira ($n = 12$ pre-nira samples, $n = 12$ post-nira samples, two-sided paired Wilcoxon rank-sum test, ns, non-significant, $*p < 0.05$, $**p < 0.01$). Bottom, pre-chemo versus post-chemo ($n = 12$ pre-chemo samples, $n = 12$ post-chemo samples, two-sided paired Wilcoxon rank-sum test, ns, non-significant, $*p < 0.05$). For boxplots, the middle line in the box is the mean, the bottom and top of the box are the first and third quartiles, and the whiskers extend to the 1.5× interquartile range of the lower and the upper quartiles, respectively.

Figure S3. Annotation of fine-grained cell states, related to Figure 2

(A and B) Normalized expression levels of cell state-specific marker genes for CD4$^+$ (A) and CD8$^+$ (B) T cells. The circle size denotes the proportion of cells within a cell state where a gene expression is non-zero.

(C–I) Top, UMAP embeddings of cells colored by cell states. Bottom, normalized expression levels of cell state-specific marker genes. Cell types annotated include natural killer (NK)/gamma delta T (gdT) cell (C), B cell (D), DC (E), monocyte and macrophage (MoMac) (F), endothelial cell (G), fibroblast (H), and pericyte (I). Insets of UMAP plots exemplify three different annotation approaches, including marker gene expression, signature scoring, and reference projection. The circle size denotes the proportion of cells within a cell state where a gene expression is non-zero.

(J) Left, UMAP embeddings of cancer cells colored by cell state. Right, UMAP embeddings overlaid with the usage score of consensus non-negative matrix factorization (cNMF) factors 1–8.
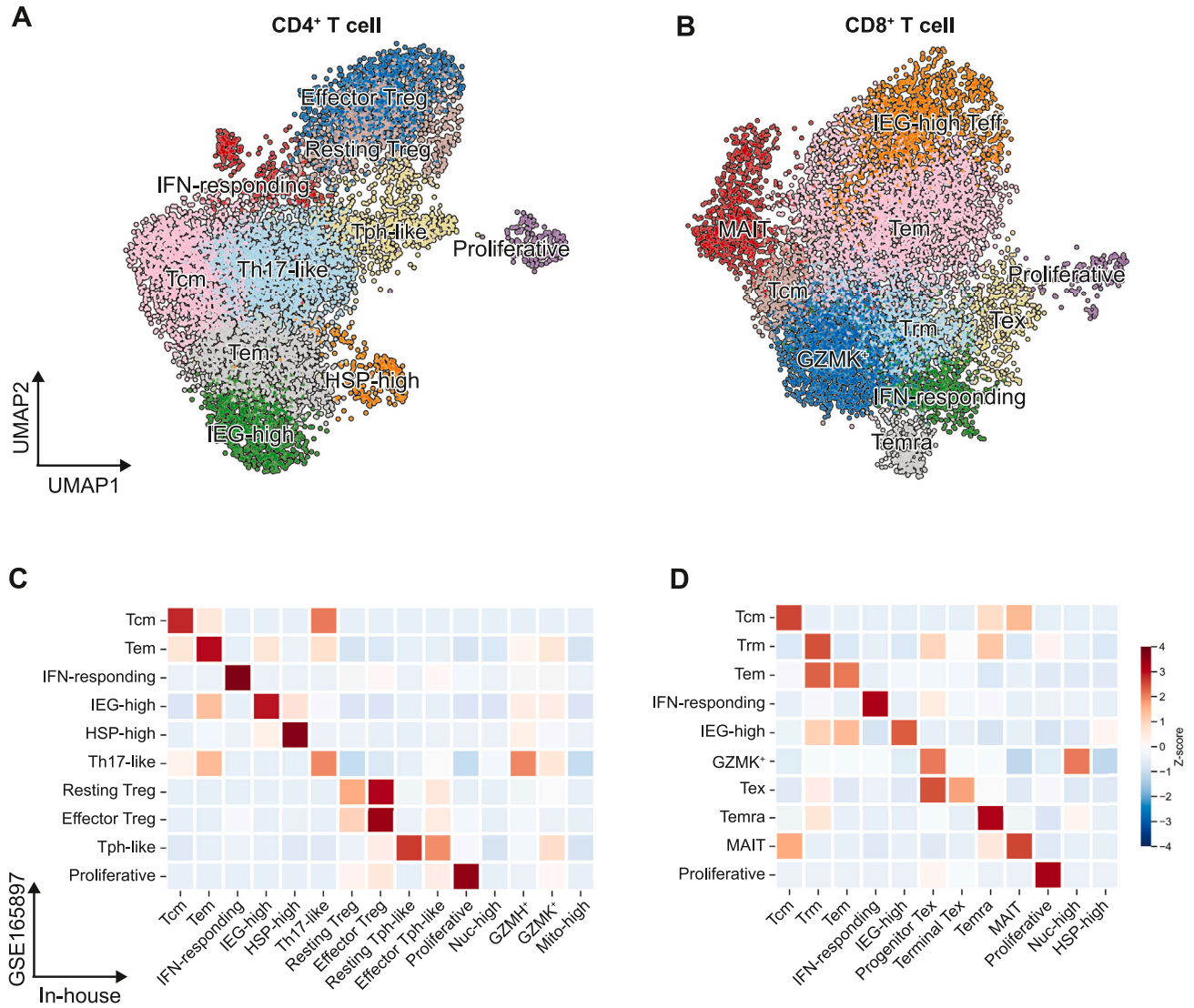
Figure S4. T cell-focused annotation of an independent scRNA-seq dataset, related to Figure 2

(A and B) UMAP embeddings of CD4^{+} (A) and CD8^{+} (B) T cells extracted from a public dataset (GSE165897) colored by T cell state.

(C and D) Overlap of cell state-specific marker genes between GSE165897 and the in-house dataset for CD4^{+} (C) and CD8^{+} (D) T cell states, measured by Jaccard index.
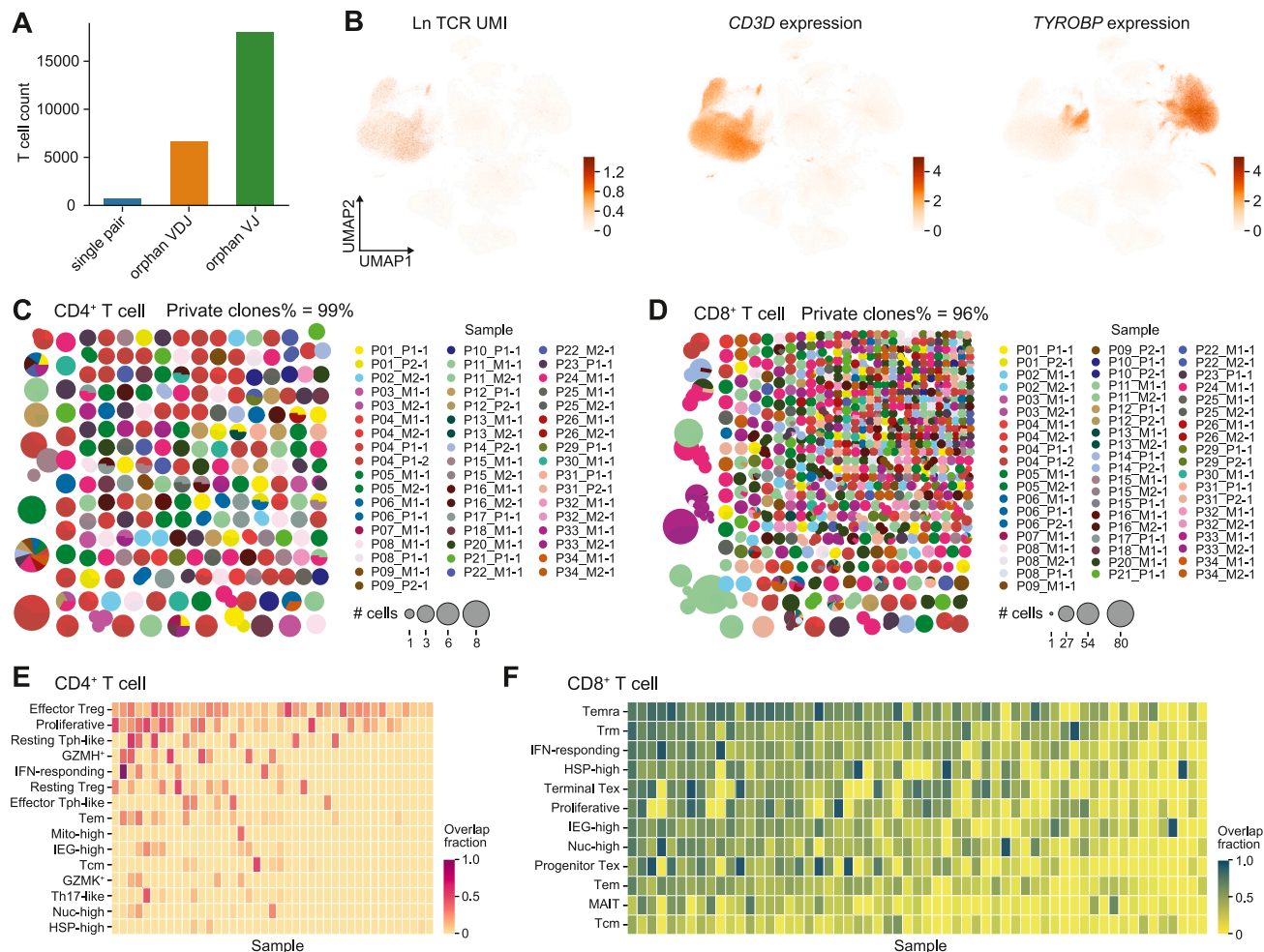
**Figure S5. Quality control of TCR clonotypes inferred from scRNA-seq data, related to Figure 3**

(A) Number of TCR clonotypes with a full pair of α- and β-chains, only a β-chain, or only an α-chain.

(B) UMAP embeddings of all cells overlaid with color grades in log-transformed TCR UMI count (left), *CD3D* expression level (middle), and *TYROBP* expression level (right).

(C and D) Sample composition of each CD4^{+} (C) or CD8^{+} (D) TCR clonotype. The circle size denotes the number of cells within each clone.

(E and F) Fraction of expanded clones in each CD4^{+} (E) or CD8^{+} (F) T cell state across samples.

See also Table S6.
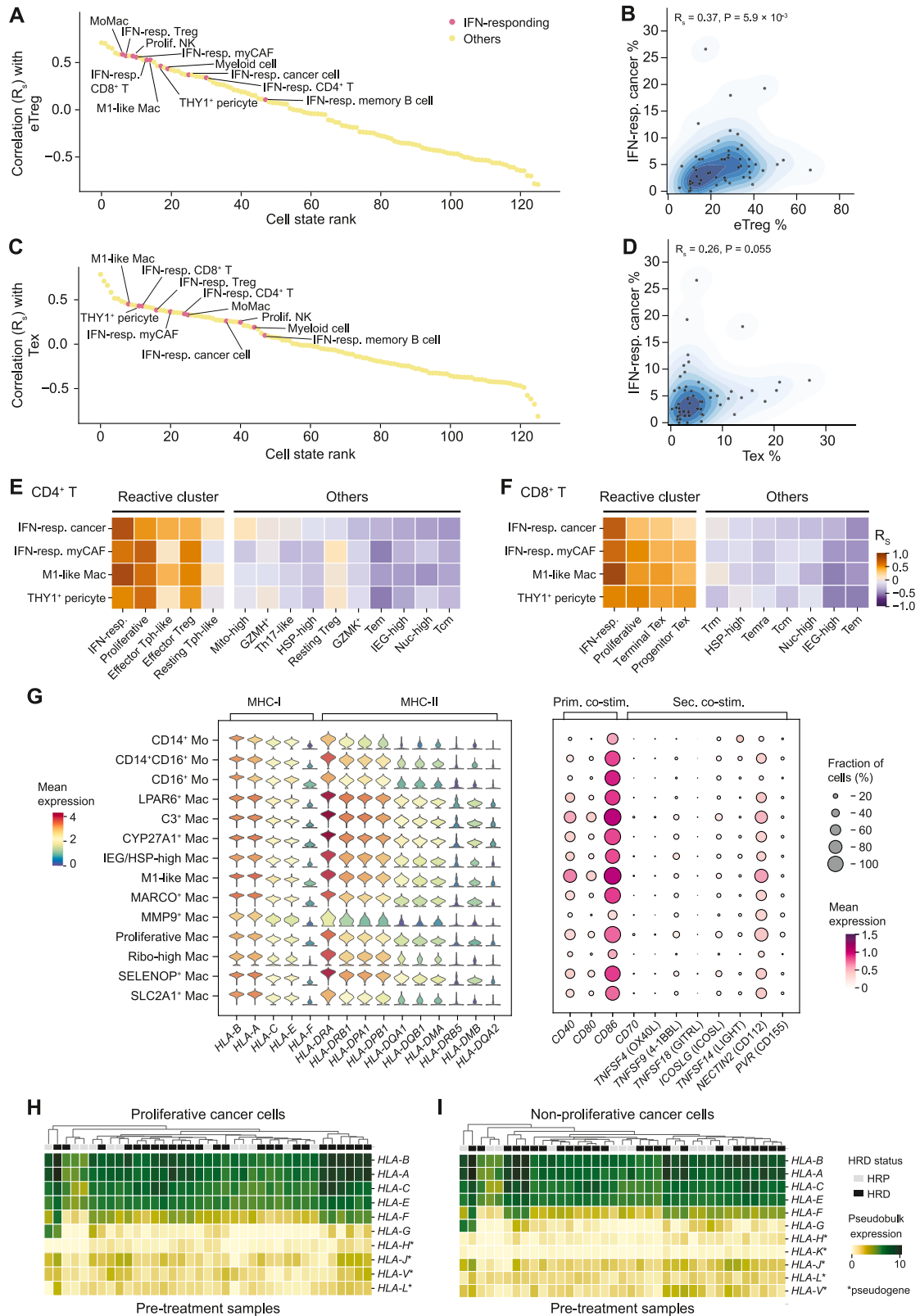
Figure S6. IFN-responding cancer cells contribute to Treg induction through MHC class II, related to Figure 6

(A) Ranking of cell types and cell states by abundance correlation with eTregs (out of all CD4$^+$ T cells) across all samples.

(B) Abundance correlation between IFN-responding cancer cells (out of all cancer cells) and eTregs (out of all CD4$^+$ T cells). R_s, Spearman rank correlation coefficient.

(C and D) Same as (A) and (B) but for Texs out of all CD8$^+$ T cells. R_s, Spearman rank correlation coefficient.

(E) Abundance correlation between top IFN-responding cell states and CD4$^+$ T cell states (each out of all CD4$^+$ T cells). R_s, Spearman rank correlation coefficient.

(F) Same as (E) but for CD8$^+$ T cells.

(G) Average expression levels of MHC class I and MHC class II genes (left) or of primary and secondary co-stimulatory T cell ligand genes (right) across MoMac cell states. The circle size denotes the proportion of cells within a cell state where a gene expression is non-zero. Labels in parentheses are common protein names.

(H) Pseudobulk (sample-average) expression levels of MHC class I genes in proliferative (left) and non-proliferative cancer cells (right). Heatmaps on the top show the HRD status of each pre-treatment sample.
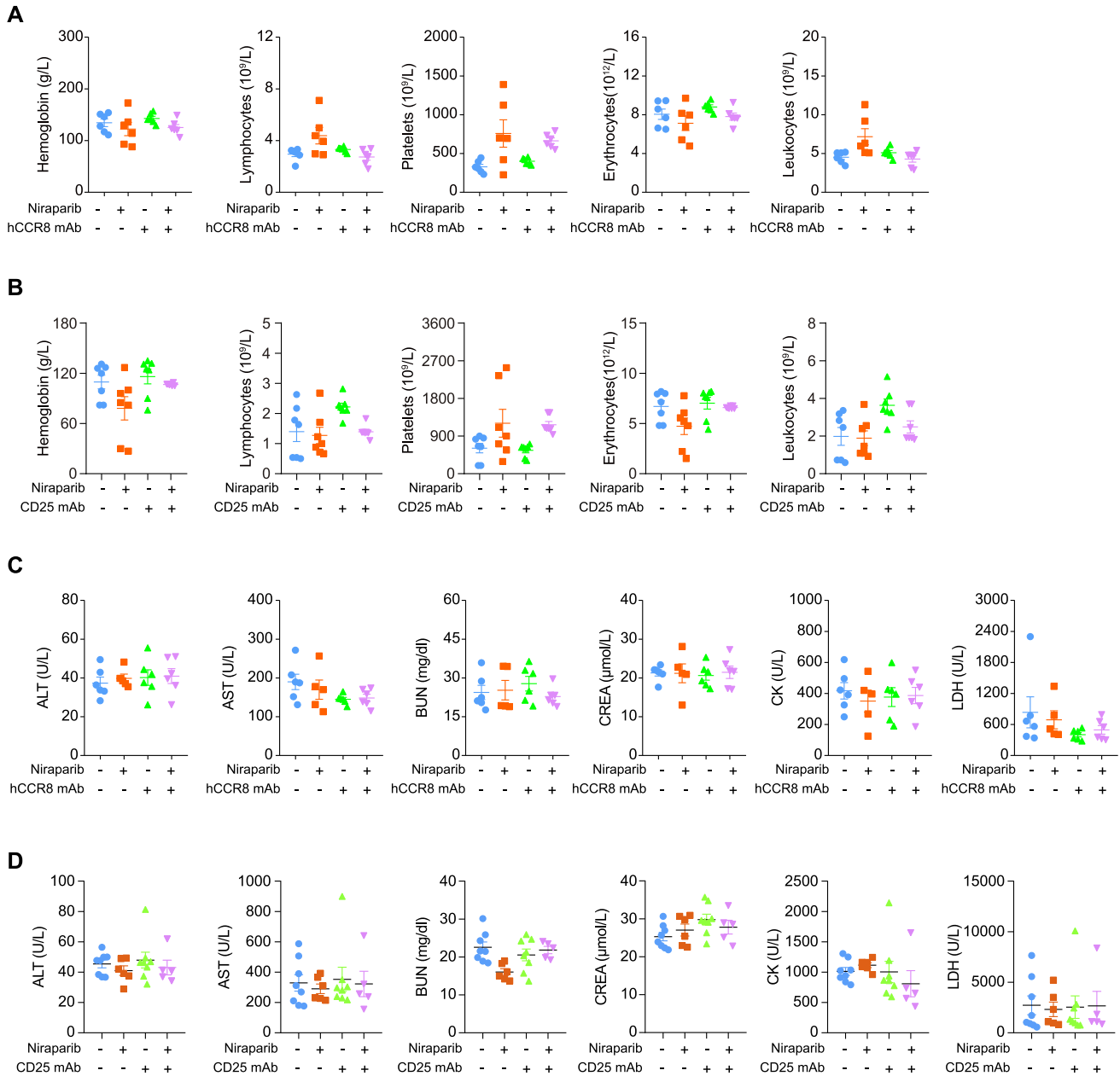
Figure S7. Niraparib combined with CCR8 mAb or CD25 mAb caused no serious side effects in mice, related to Figure 7

(A) Difference in level of hemoglobin, lymphocytes, platelets, erythrocytes, and leukocytes in the blood of h*CCR8* mice treated with control, niraparib, CCR8 mAb, or their combination.

(B) Same as (A) but for WT mice treated with control, niraparib, CD25 mAb, or their combination.

(C) Difference in level of ALT, AST, BUN, CREA, CK, and LDH in the serum of h*CCR8* mice treated with control, niraparib, CCR8 mAb, or their combination.

(D) Same as (C) but for WT mice treated with control, niraparib, CD25 mAb, or their combination.

ALT, alanine aminotransferase; AST, aspartate aminotransferase; BUN, blood urea nitrogen; CREA, creatinine; CK, creatine kinase; LDH, lactate dehydrogenase.